Electrochemical, biochemical, structural studies of cytochrome P450 monooxygenases involved in metabolism of vitamin D

by

Steve Y. Rhieu

Sc.B., Bioengineering, The University of California at Berkeley, USA, 2004

Thesis

Submitted in partial fulfillment of the requirements for
the Degree of Doctor of Philosophy
awarded jointly by the School of Engineering and the Division of Biology and Medicine at Brown University

May 2011

This dissertation by Steve Y. Rhieu is accepted in its present form
by the Biomedical Engineering Graduate Program, a joint program of the School of Engineering and the Division of Biology and Medicine as satisfying the dissertation requirement for the degree of Doctor of Philosophy

Date ....
G. Tayhas R. Palmore, Director

Recommended to the Graduate Council

Date ....
Domenico Pacifici, Reader

Date ....
Alexander Brodsky, Reader

Date ....
G. Satyanarayana Reddy, Reader

Date ....
John C. MacDonald, External Reader

Approved by the Graduate Council

Date ....
Peter M. Weber
Dean of the Graduate School

Acknowledgments

I owe my deepest gratitude to those of who helped me finish my graduate study in meaningful ways. First, Dr. Andrew J. Annalora, who contributed most of molecular docking analysis in Chapters 4 and 5, has given me opportunity to deepen my knowledge in cytochrome P450 enzymes involved in vitamin D metabolism. I owe a debt of gratitude to Prof. Toshiyuki Sakaki, for his generous provision of plasmid that encodes mouse CYP27B1 used in Chapters 2 and 3. I would also like to thank Prof. Paul Vouros and Ms. Rose M. Gathungu for their help on GC/MS analysis in Chapter 4 and 5. In addition, I wish to thank Drs. Milan R. Uskoković, Tai C. Chen, Antonio Mouriño, JoEllen Welsh, and Inge Schuster for their invaluable help. Credit is also due to Prof. Domenico Pacifici, Prof. Alexander Brodsky, Prof. G. Satyanarayana Reddy, and Prof. John C. MacDonald who served on my thesis committee.

I personally would like to express my sincere gratitude to Prof. G. Satyanarayana Reddy, who introduced me to the field of vitamin D metabolism. Also deserving of my thanks are all the group members of the Palmore group – Sung-Yeol Kim, Kwang-Min Kim, Vince Siu, Sujat Sen, and Daniel Ludwig. Most importantly, I am heartily thankful to my advisor, Prof. G. Tayhas R. Palmore, whose unflagging support and guidance enabled me to complete my thesis work. Her constructive criticism and depth of knowledge in my research always inspired me to think like a scientist.

I gratefully acknowledge financial support from NASA, ECS, and NSF, through a Rhode Island Space Grant Fellowship, a F.M. Becket Summer Research Fellowship, and a GK-12 Teaching Fellowship, respectively.

As always, I would like to thank my parents and parents-in-law for their steadfast love and care. Last, of course, my cordial gratitude goes to you, Hana. Thank you for always being there for me. I am sincerely grateful for the memories we have shared and those we have yet to create.

Preface

This thesis describes research on the investigation of two essential cytochrome P450 monooxygenases, namely CYP27B1 and CYP24A1, involved in activation and inactivation of vitamin D hormone, respectively. In Chapter 1, an overview of cytochrome P450 enzymes and vitamin D is provided to help readers understand the subsequent discussion of experimental work reported in this thesis. In Chapters 2 and 3, the electrochemical and biochemical properties of mouse CYP27B1 are examined in an attempt to develop a platform that provides a preview to vitamin D biosensing. The biochemical and structural properties of rat CYP24A1 are studied in Chapters 4 and 5, providing detailed information on the metabolism of several vitamin D analogs and a natural metabolite of vitamin D hormone, respectively.

Contents

List of Tables

List of Figures

Chapter 1

Cytochrome P450 Monooxygenase and Vitamin D: An Overview

1.1 Cytochrome P450 enzymes

1.1.1 Background

In 1955, Mason and Hayashi independently provided evidence for the existence of enzymes being able to catalyze the transfer of oxygen into substrates [1, 2]. Three years later Garfinkel and Klingenberg detected a carbon monoxide (CO) binding pigment in liver microsomes of pigs and rats, respectively [3, 4]. When pigment samples are reduced with dithionite and treated with CO, an intense absorption band arises at 450 nm [3, 4]. This pigment was ultimately proven to be a heme-containing enzyme by Omura and Sato, who designated it cytochrome P450 (CYP) [5, 6]. The regio- and stereo-specific reactions catalyzed by CYPs under physiological conditions include the hydroxylation of hydrocarbons (Fig. 1.1), alkene epoxidation, heteroatom

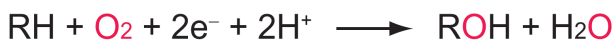

Figure 1.1: Hydroxylation reaction catalyzed by cytochrome P450 monooxygenases involves the activation of molecular oxygen, leading to the insertion of a single atom of oxygen into an organic substrate with concomitant reduction of the other atom to water.

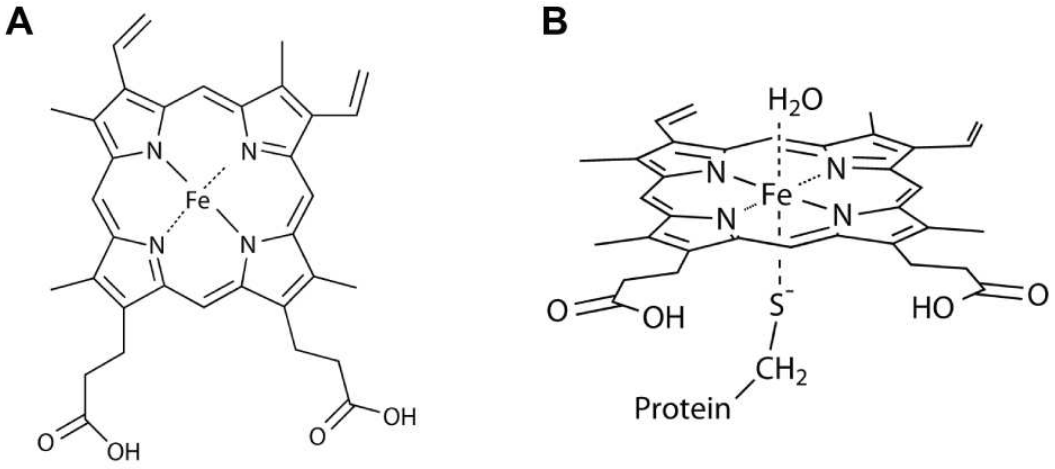

Figure 1.2: The structures of prosthetic heme-*b* group (A) and hexa-coordinated ferric heme system in the protein backbone (B).

(N,S) oxidation, dealkylation, and (anaerobic) dehalogenation [7, 8, 9, 10].

Cytochrome P450 monooxygenases are heme-containing metalloenzymes [11]. Out of four heme prosthetic groups found in biological systems, heme-*b* (more commonly referred to as protoheme IX (Fig. 1.2A)) is found not only in cytochrome P450 enzymes but also in hemoglobin, myoglobin, nitrophorin, catalase, and nitric oxide synthase. The heme group is held in the protein by a proximal ligand to the iron (Fe^{III}) from a thiolate side chain of a cysteine (Fig. 1.2B) that modulates the heme electronic environment in such a way as to alter the reduction potential and therefore thermodynamically control the overall function of the protein [12]. A labile water molecule is coordinated to the heme as a distal ligand. The iron atom (Fe^{III}) at the center of the heme is also coordinated by four nitrogen atoms from a planar porphyrin ring. The propionate and vinyl side-chains influence the heme orientation via non-bonding interactions with the protein backbone.

1.1.2 Cytochrome P450 nomenclature

The heme component retains a similar topology through the superfamily although sequence identity can be lower than 30%. This variation in identity is used to divide the superfamily (described as CYP) into families (> 40% sequence homology) and then into subfamilies (> 55% sequence homology) [13]. The nomenclature introduced

by Nebert *et al.* designates all gene members of the P450 superfamily with a CYP prefix, followed by a numeral for the family, a letter for the subfamily, and a numeral for the individual gene [14].

1.1.3 Cytochrome P450 classification

Monooxygenation reactions (Fig. 1.1) catalyzed by cytochrome P450 require an external source of two electrons that are transferred from NAD(P)H to the heme iron of the enzyme through the combined action of its redox cofactors. Since variations in the nature of the redox cofactors exist across the superfamily, further classification is necessary (Fig. 1.3). Most bacterial and mitochondrial CYPs (Class I) are three component systems, comprising a CYP, a ferredoxin (i.e., an iron-sulfur protein), and a NAD(P)H-dependent FAD-containing ferredoxin reductase. The microsomal CYPs (Class II) are two component systems, comprising a NADPH-dependent diflavin reductase (FAD and FMN) and a CYP, which are both membrane bounded. Class III CYPs (e.g., CYP102 from *Bacillus megaterium*) contain the same redox cofactors as the Class II CYPs but are soluble and fused into one continuous polypeptide.

1.1.4 Catalytic cycle of cytochrome P450

The mechanism by which cytochrome P450 enzymes are able to activate dioxygen to carry out the monooxygenation reaction (Fig. 1.1) has long been investigated, but many details have not yet been established. Structurally and biochemically, the best characterized P450 is CYP101 (or CYPcam from *Pseudomonas putida*) [16, 17, 18], which catalyzes the regio- and stereo-specific hydroxylation of camphor to 5-*exo*-hydroxy-camphor according to the mechanism [8, 19, 20] shown in Fig. 1.4.

As shown in Fig. 1.4, the steps of the catalytic cycle are as follows: (**1**) substrate (RH) binds to the enzyme in its resting state where the iron is in the ferric (Fe^{III}) state. Binding of the substrate results in the displacement of the sixth ligand (i.e., a labile water molecule) and conversion of the spin state of the ferric iron from low ($S = 1/2$) to high ($S = 5/2$). The change in spin-state gives rise to an

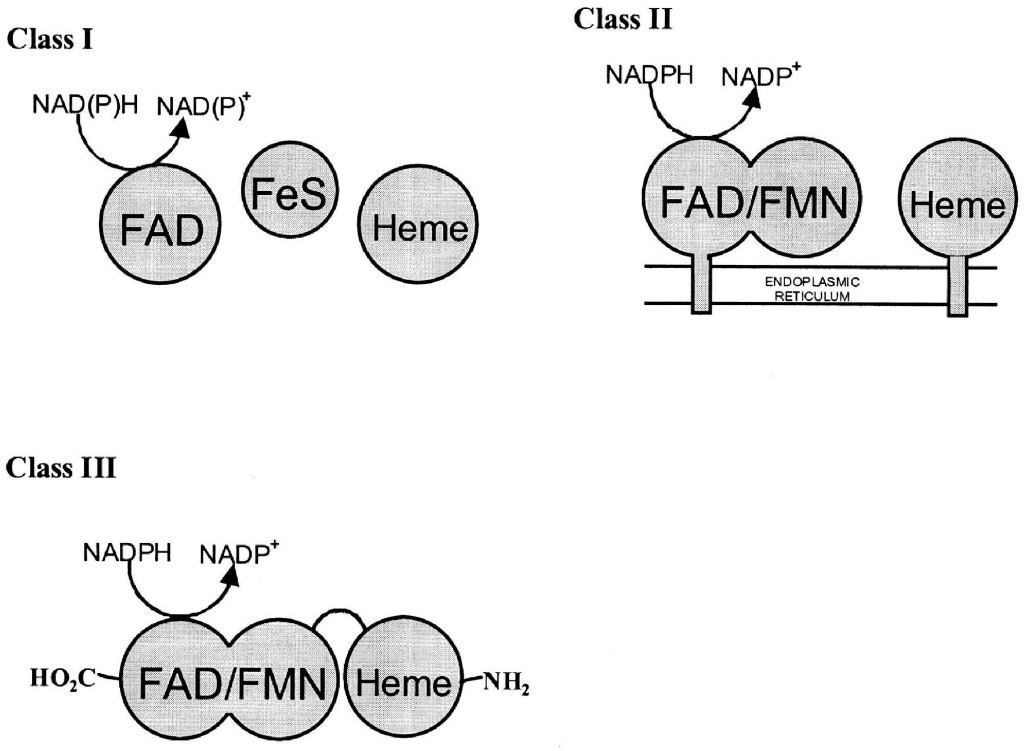

Figure 1.3: Cytochrome P450 classification (Adapted and modified from Ref. [15]).

increase in the redox potential ($E^{\circ\prime}$) of the enzyme heme (–330 to –173 mV vs. NHE [21, 22]), thereby making electron transfer from the redox partner of CYP101 (i.e., putidaredoxin, $E^{\circ\prime} = –196$ mV [23]) to the enzyme thermodynamically favorable; (**2**) putidaredoxin reduces the heme iron to the ferrous (Fe^{II}) state; (**3**) molecular oxygen binds to the iron atom; (**3a**) CO addition yields the ferrous–CO inhibitor adduct with its characteristic absorbance peak near 450 nm; (**4**) a second electron is delivered yielding a highly unstable intermediate (i.e., a ferric peroxide adduct), which (**5**) can be protonated to give a hydroperoxide complex; (**6**) a second protonation of that same oxygen then leads to heterolytic O–O bond cleavage releasing water and generating the proposed oxo-ferryl ($O{=}Fe^{IV}$) porphyrin radical intermediate (sometimes represented as $(FeO)^{3+}$), which is equivalent to the high-valent iron-oxo intermediate of peroxidase enzymes called compound I; (**7**) the remaining oxygen bound to the iron acts on the substrate with the formal insertion of the oxygen into a carbon-hydrogen bond, forming an alcohol; (**8**) product release regenerates the resting state of the enzyme.

The electron equivalents that are not utilized to oxidize substrate (i.e., electron leakage from NAD(P)H to O_2), however, can be liberated from intermediate steps of the catalytic cycle of cytochrome P450 in the form of superoxide anion (route **A**), hydrogen peroxide (route **B**), or water (route **C**) [24, 25, 26] as illustrated in Fig. 1.4.

1.1.5 Biological significance of cytochrome P450

There is broad interest in the CYPs because of the significance of these enzymes in a wide variety of disciplines, ranging from inorganic chemistry to medical genetics. Two major views on the function of CYPs have long been considered: (i) the enzymes have critical and specific roles in metabolism of endogeneous chemicals and (ii) the enzymes play a major role in detoxifying a large spectrum of foreign substances including drugs and other xenobiotics, in a relatively non-selective manner [27]. Owing to the numerous new drugs and pollutants each year that CYPs encounter, the lack of complete selectivity of some CYPs and the number of the individual forms are thus advantages. However, in some cases the oxidation of these chemicals can generate

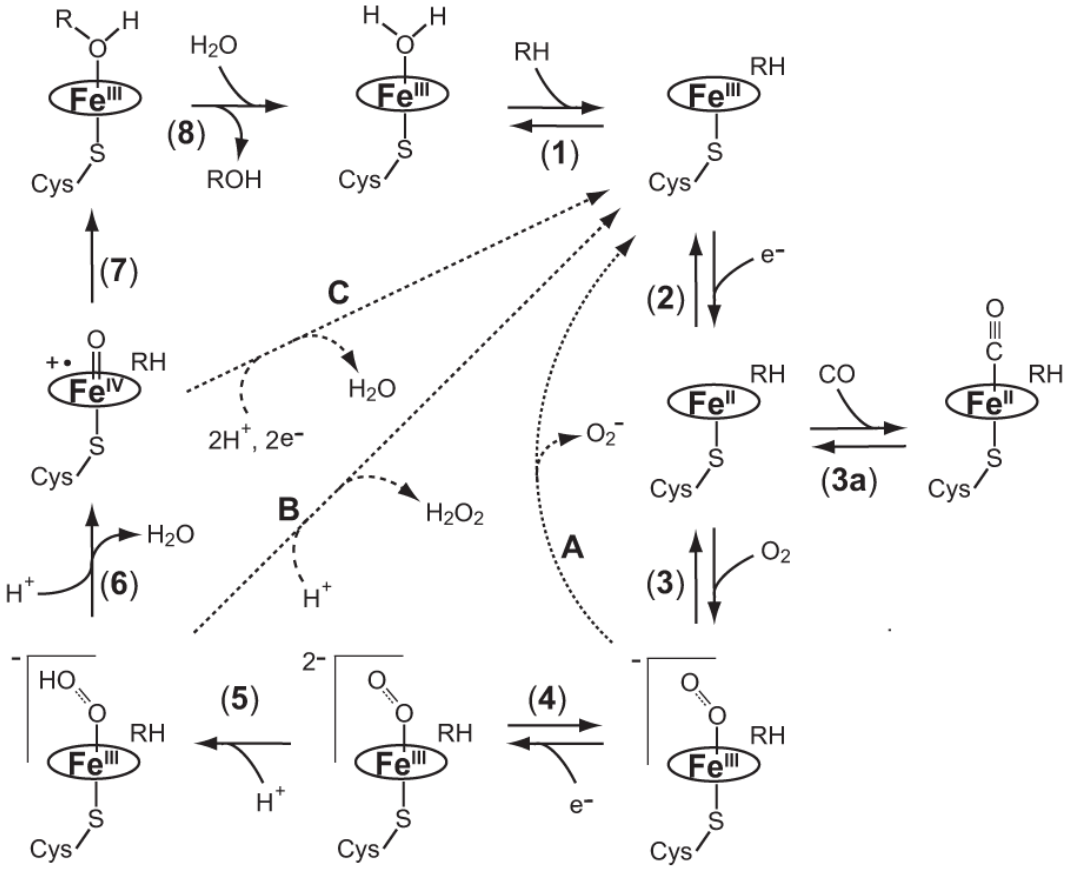

Figure 1.4: Catalytic cycle of cytochrome P450 (Adapted and modified from Ref. [19]).

dangerous electrophiles that are detrimental to the host cells and may cause cancer [28].

CYPs have been characterized in bacteria, fungi, corals, insects, fish, and avians showing that CYPs are nearly ubiquitous and have a crucial biological importance in all organisms [29, 30, 31, 32]. In plants, CYPs are involved in the biosynthesis of natural products such as amino acid derivatives, fatty acids, flavinoids, and terpenoids [29]. In mammals, many CYPs play a critical role in the synthesis of various steroids. For example, the lack of functional CYP21A2, an enzyme catalyzing 21-hydroxylation of progesterone and pregnenolone, results in a serious congenital disease [33]. More importantly, CYPs are also known to play an essential role in vitamin D metabolism [34]. The information on CYPs that are involved in biosynthesis of vitamin D hormone and its inactivation will follow in Section 1.2.

1.2 Cytochrome P450 and vitamin D

1.2.1 Background

In 1920, Aldolf Windaus and his colleagues isolated a substance from plant sterols that, following irradiation with ultraviolet light, was active in healing rickets a disorder characterized by a defect in mineralization of the skeleton [35]. The substance was termed vitamin D, which now collectively refers to two different secosteroids (Fig. 1.5), namely cholecalciferol (vitamin D_3) and ergocalciferol (vitamin D_2). Vitamin D_3 is derived from 7-dehydrocholesterol in the skin upon exposure to UVB-light (Fig. 1.6) while vitamin D_2 is derived from ergosterol that is restricted to yeast or fungi [36, 37]. It was also discovered in the 1920s and 1930s that an *endogenous factor* played an unequivocal role in calcium homeostasis by increasing the intestinal absorption of calcium needed for bone mineralization [38]. The chemical structure of this endogenous factor was later identified to be the hormonally active form of vitamin D, 1α,25-dihydroxyvitamin D_3 (1α,25$(OH)_2D_3$) [39, 40, 41], which plays a central role in calcium and phosphorous metabolism. 1α,25$(OH)_2D_3$ regulates the expression

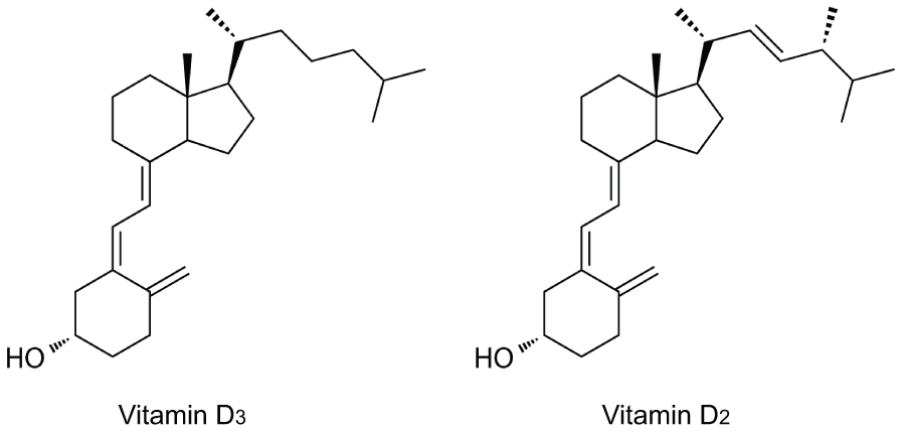

Figure 1.5: Structures of vitamin D_3 and vitamin D_2.

of a wide variety of genes through its binding to the vitamin D receptor (VDR) [42]. Ligand-bound VDR requires the retinoid-X receptor as a partner for binding to vitamin D-response elements found predominantly in the promoter of target genes. Through a complex set of co-activators, transacetylase systems are activated to loosen chromatin, resulting in an increased transcription rate of target genes [43, 44].

1.2.2 CYPs involved in the first activation step of vitamin D

As mentioned earlier, the photoconversion of 7-dehydrocholesterol in the epidermis to vitamin D_3 is the main source of vitamin D in human. Vitamin D_3 is then transported to the liver, where it undergoes its first hydroxylation to produce 25-hydroxyvitamin D_3 ($25(OH)D_3$), the major circulating form of vitamin D_3 (Fig. 1.6). At physiological concentrations, $25(OH)D_3$ is thought to lack intrinsic biological activity, but, rather, is the precursor of the active hormone, $1\alpha,25(OH)_2D_3$.

At present, four distinct human CYPs, namely the mitochondrial CYP27A1 [45] and the microsomal CYP2R1 [46], CYP2J2 [47], and CYP3A4 [48] were identified as enzymes that are capable of catalyzing hydroxylation of vitamin D_3 at C25. Of these CYPs, CYP2R1 showed the highest affinity and specificity for vitamin D_3 [46]. The crystal structure of human CYP2R1 complexed with vitamin D_3 [49] revealed an extended binding site lined with mostly hydrophobic groups in which the site of C25-hydroxylation of vitamin D_3 is placed 6.5 Å apart from the heme iron (Fig. 1.7).

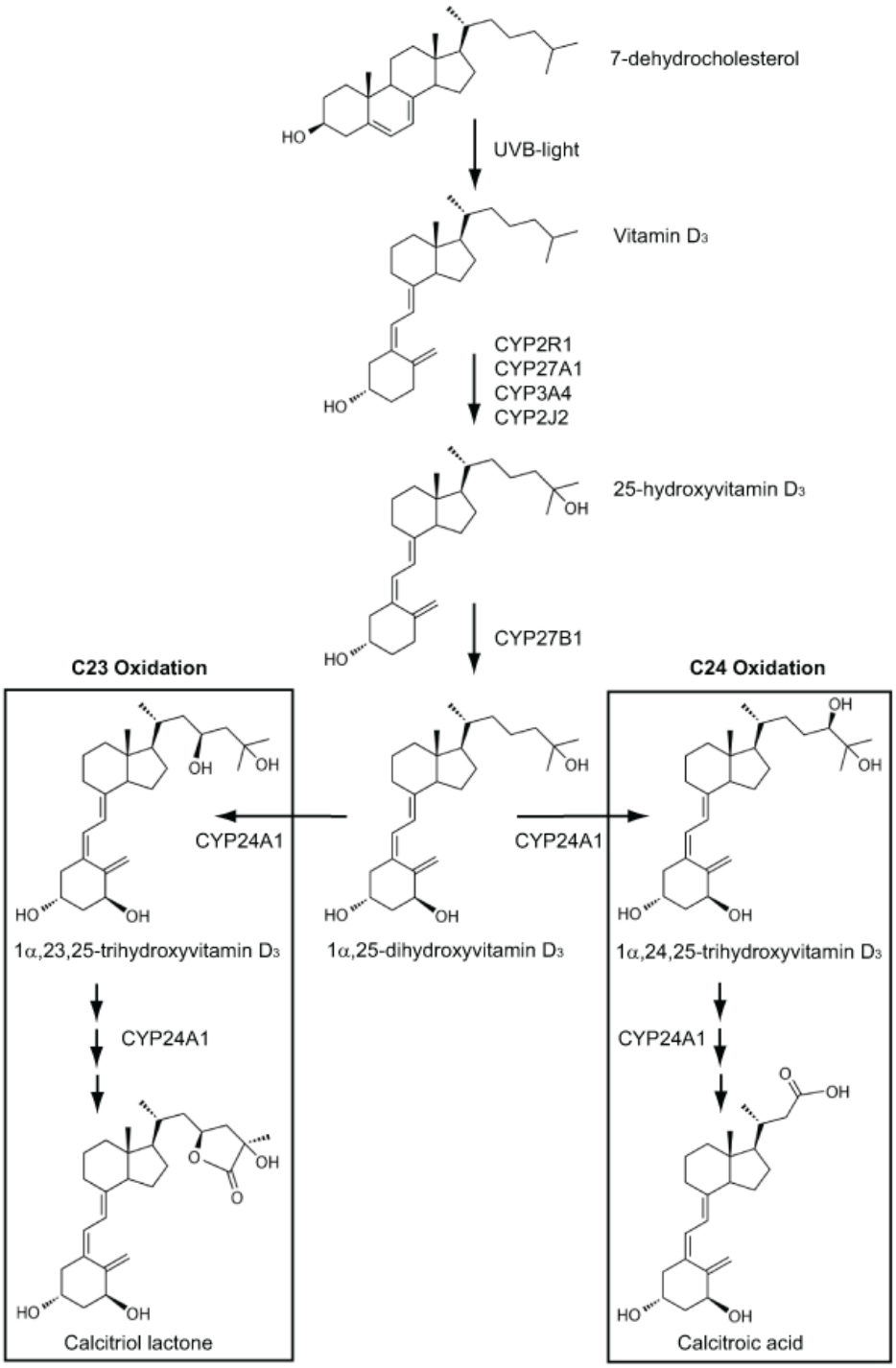

Figure 1.6: Activation and inactivation of vitamin D hormone catalyzed by cytochrome P450s.

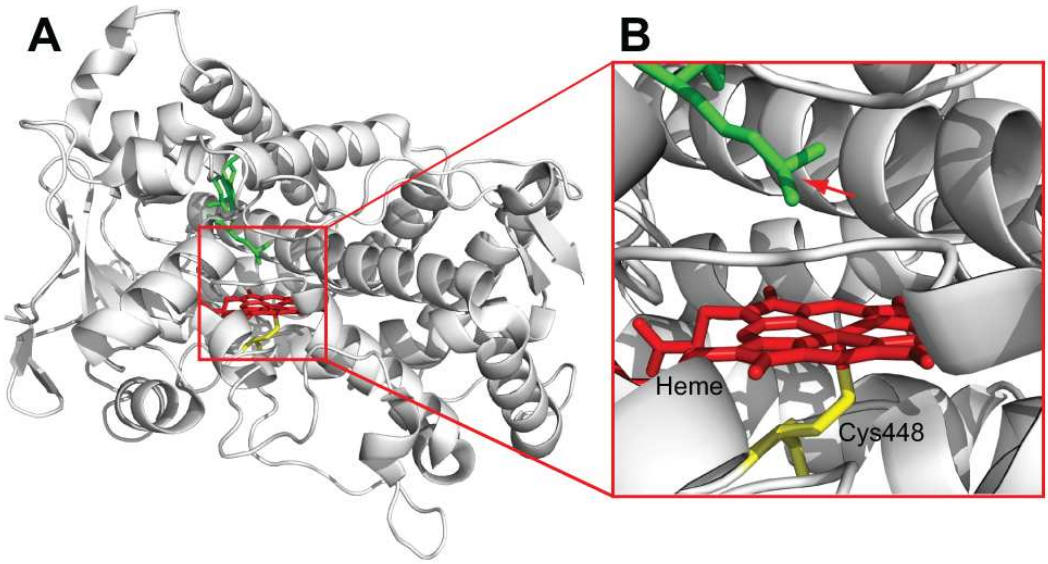

Figure 1.7: (A) Structure of CYP2R1 complexed with vitamin D_3 (PDB ID: 3C6G). (B) Closed-up view of the region of the active site of CYP2R1. An arrow in red indicates the site of the C25-hydroxylation of vitamin D_3 catalyzed by CYP2R1. Heme is in red; vitamin D_3 in green; cysteine residue 448 as a proximal heme ligand in yellow.

It was also found that a genetic defect of *CYP2R1* causes a hereditary form of rickets [50, 51].

1.2.3 CYP27B1 involved in the second activation step of vitamin D

The hormonally active form of vitamin D, 1α,$25(OH)_2D_3$, is formed predominantly in the proximal convoluted tubule cells of the kidney [52]. The enzyme responsible for the production of 1α,$25(OH)_2D_3$ is CYP27B1, which is a mitochondrial CYP (Class I) that selectively catalyzes the 1α-hydroxylation reaction of $25(OH)D_3$ into 1α,$25(OH)_2D_3$ [53]. This reaction proceeds by electron transfer from NADPH to the heme site of CYP27B1 and it involves the aid of redox cofactors such as a FAD-containing NADPH-adrenodoxin reductase and an iron-sulfur protein known as adrenodoxin [54]. The expression of *CYP27B1* is tightly regulated by parathyroid hormone (PTH) and 1α,$25(OH)_2D_3$. In response to low serum calcium, the parathy-

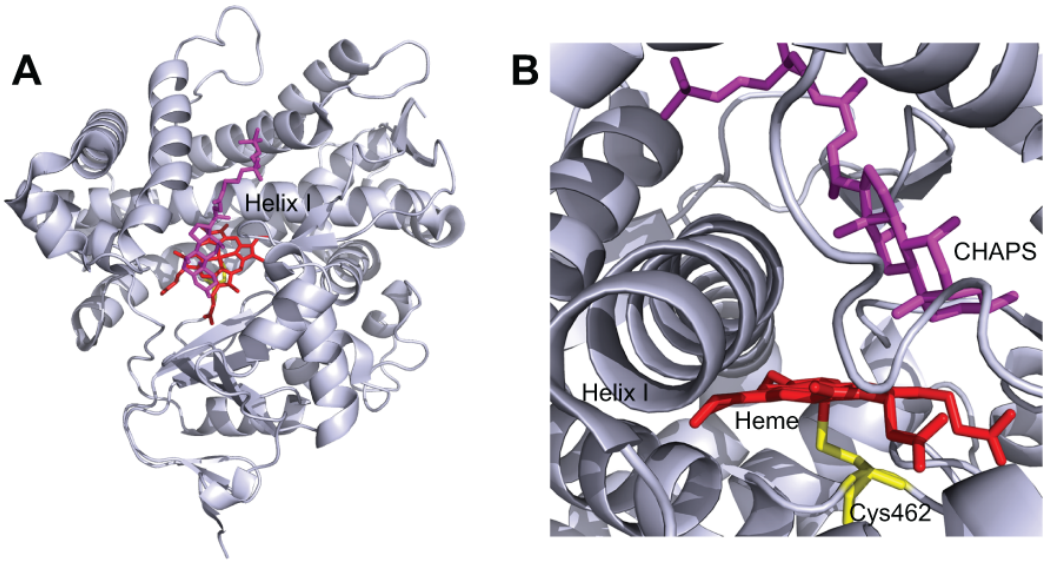

Figure 1.8: (A) Structure of substrate–free open form of rat CYP24A1 (PDB ID: 3K9V). (B) Closed-up view of the region of the active site of CYP24A1. CHAPS, a zwitterionic detergent used to purify the enzyme, binds tightly to the active site. The role of the kinked helix I with respect to substrate recognition of CYP24A1 will be discussed in Chapter 4. Heme, CHAPS, and cysteine residue 462 are depicted in red, purple, and yellow, respectively.

roid gland secretes PTH, which stimulates the transcription of *CYP27B1*, resulting in an increase in the production of 1α,25(OH)$_2$D$_3$. In turn, 1α,25(OH)$_2$D$_3$ directly stimulates intestinal calcium absorption and corrects the initial response of low serum calcium. Besides its natural substrate 25(OH)D$_3$ (K_m = 0.38 μM [19]), CYP27B1 shows high specificity toward some 25-hydroxylated vitamin D$_3$ metabolites such as 24,25-dihydroxyvitamin D$_3$ and 24-oxo-25-hydroxyvitamin D$_3$, but no specificity toward vitamin D$_3$ [55]. This finding suggests that the 25-hydroxyl group of vitamin D$_3$ is essential for CYP27B1 to proceed with 1α-hydroxylation. At present, structural details on substrate recognition of CYP27B1 are still preliminary and the crystal structure of CYP27B1 has not yet been solved.

1.2.4 CYP24A1 involved in inactivation of the hormonally active form of vitamin D

As stated in Section 1.2.1, 1α,25$(OH)_2D_3$ induces a wide range of genes through binding to VDR [42]. Of great importance physiologically is that 1α,25$(OH)_2D_3$ specifically induces expression of a gene, which encodes the mitochondrial CYP24A1 [43]. CYP24A1, located in the inner mitochondrial membrane, is responsible for the inactivation of 1α,25$(OH)_2D_3$ (also 25$(OH)D_3$ as a minor substrate) and therefore serves as an important mechanism for controlling the tissue levels of 1α,25$(OH)_2D_3$ [56]. This important physiological role of CYP24A1 is evident from studies [57, 58] in which *CYP24A1*-knockout mice showed 50% lethality before adulthood, and suffered from hypercalcemia and intramembraneous ossification of bone due to a highly retarded clearance of 1α,25$(OH)_2D_3$ in target tissues. As *CYP24A1* is the most responsive vitamin D target gene, its expression is widely used as the most sensitive indicator of the vitamin D hormonal function. Furthermore, *CYP24A1* is often considered as an oncogene, the expression of which is highly elevated in a wide range of malignancies (e.g., colorectal cancer [59]) due to gene amplification.

Rat CYP24A1 is the first mitochondrial CYP ever crystallized [60]) and it shows an open cleft leading from the distal surface to the heme group in the active site (Fig. 1.8). The structural features of CYP24A1 in its substrate binding cavities are similar to that of CYP3A4, concerning the widening of the cavity close to the catalytic heme center, thereby exposing a larger portion of the heme surface [44]. Inactivation of 1α,25$(OH)_2D_3$ catalyzed by CYP24A1 proceeds through three different oxidation pathways, namely C23, C24, and C26 oxidation pathways (Fig. 1.9), which involve sequential modification of the side-chain of 1α,25$(OH)_2D_3$. *In vitro* studies with recombinant CYP24A1 from rat and human confirmed that all the intermediary metabolites shown in Fig. 1.9 are produced solely by CYP24A1 [56, 61]. In addition, there is a species-based difference in CYP24A1-dependent inactivation of 1α,25$(OH)_2D_3$. Both rat and mouse CYP24A1 show preference toward C24 oxidation pathway over C23 oxidation pathway, resulting in the production of calcitroic acid

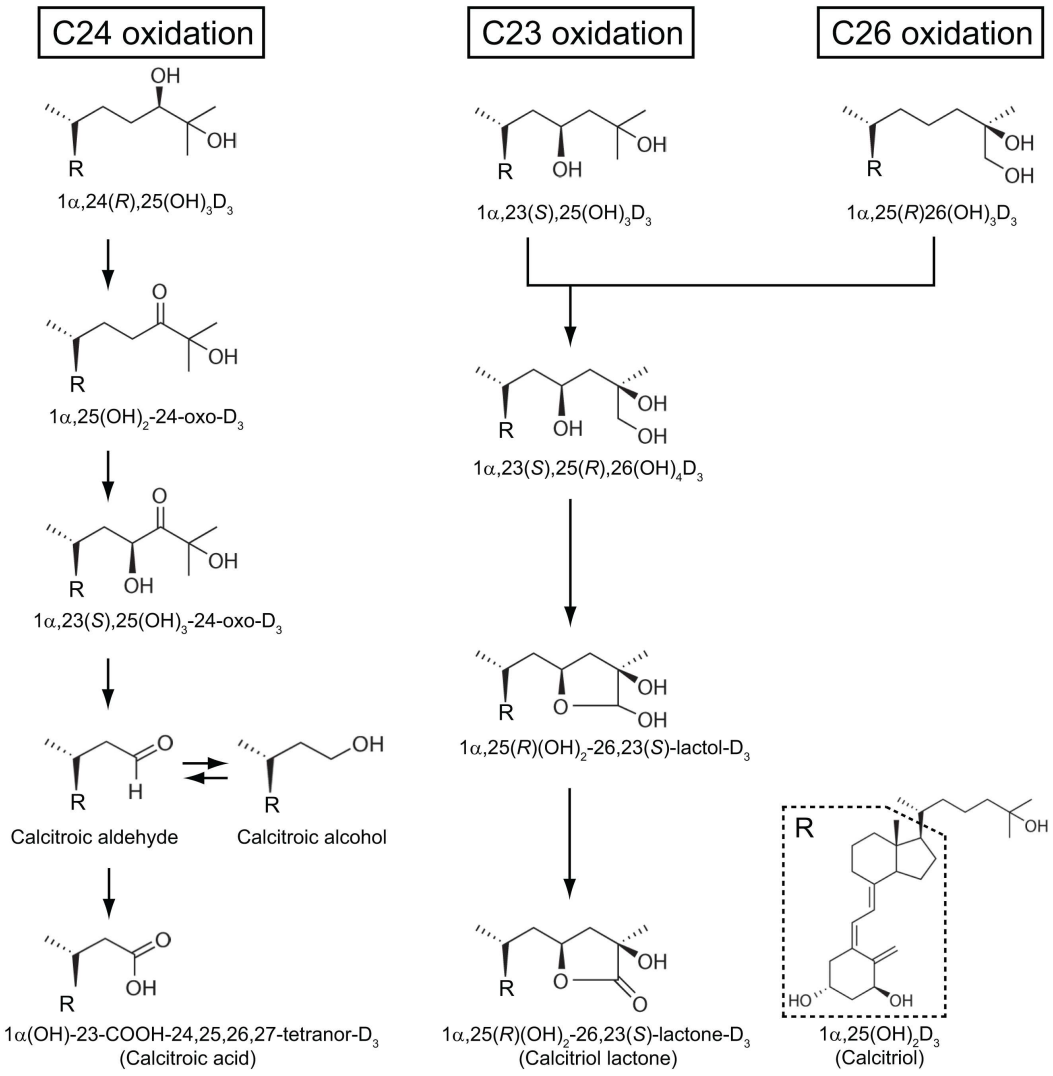

Figure 1.9: CYP24A1-mediated metabolism of $1\alpha,25(OH)_2D_3$ via C24, C23, or C26 oxidation pathways.

as the end product [62, 63, 64]. On the contrary, 1α,25$(OH)_2D_3$ is metabolized by human CYP24A1 through both C23 and C24 oxidation pathways, resulting in two different end products, calcitroic acid and calcitriol lactone [65, 66].

1.3 Thesis overview

As previously described, CYP enzymes have an important physiological role in activating unfunctionalized carbon atoms regio- and stereo-specificially, as well as in their potential to catalyze challenging oxidations for chemical synthesis. Exploiting this catalytic activity of CYPs *in vitro* may help yield future clinical benefits in regards to drug screenings as well as the development of biocatalysts or biosensors. In support of such an effort, the studies in this thesis used CYP27B1 and CYP24A1 for vitamin D biosensing applications and vitamin D drug metabolism, respectively.

Chapters 2 and 3 focus mainly on characterizing the electrochemical and biochemical properties of CYP27B1, which can be used as a sensing element that recognizes the analyte of interest (i.e., 25$(OH)D_3$, a major circulating form of vitamin D) and transduces the signal (i.e., electrocatalytic current based on the turnover rate of CYP27B1). In Chapter 2, the electrochemical properties of mouse CYP27B1 were examined using cyclic voltammetry. The use of surfactant films to immobilize CYP27B1 on carbon electrodes demonstrates direct electrochemical communication between the electrode and the enzyme. However, lack of electrocatalytic substrate hydroxylation by immbolized CYP27B1 was observed. Following the results in Chapter 2, Chapter 3 demonstrates the analysis of biochemical and spectroscopic measurements on CYP27B1 in surfactant films. The data indicate that the surfactant used in Chapter 2 to immobilize CYP27B1 on electrodes is capable of inducing a P420 isomer, an inactive form of CYP. These results provide insight into the parameters (e.g., immobilization conditions) that control the structure and redox properties of CYP27B1 and contribute to the understanding of the apparently anomalous behavior of CYPs in bioelectronic devices.

Aside from its central role in calcium homeostasis, 1α,25$(OH)_2D_3$ also displays

non-calcemic actions such as anti-proliferative and pro-apoptotic activities against certain types of cancer cells. However, the clinical use of $1\alpha,25(OH)_2D_3$ as an anti-cancer drug is limited by its side effect of hypercalcemia. As a result, numerous less calcemic synthetic analogs of $1\alpha,25(OH)_2D_3$ have been synthesized. In part, the strategy behind the synthesis of one group of vitamin D analogs was to block their inactivation by CYP24A1 so that their biological activities can be prolonged. In Chapter 4, the metabolism of two such analogs, namely 1α,25-dihydroxy-16-ene-23-yne-vitamin D_3 and 1α,25-dihydroxy-16-ene-23-yne-26,27-dimethyl-vitamin D_3, was examined using rat CYP24A1 in a reconstituted system. To gain a better insight into the structural determinants of substrate recognition, as a means to understand the metabolic profiles of the selected analogs, a molecular docking analysis was examined using the crystal structure of rat CYP24A1.

The metabolism study of less calcemic synthetic analogs using CYP24A1 in Chapter 4 is extended to 1α,25-dihydroxy-3-epi-vitamin D_3 ($1\alpha,25(OH)_2$-3-epi-D_3), a less calcemic natural metabolite of $1\alpha,25(OH)_2D_3$ in Chapter 5. The data provided for the first time definitive evidence that $1\alpha,25(OH)_2$-3-epi-D_3 when compared to $1\alpha,25(OH)_2D_3$ exhibits higher metabolic stability. Finally, the findings from Chapters 4 and 5 should enable one to design rationally efficacious vitamin D drugs through the improved understanding of structure-function relationships between CYP24A1 and various synthetic analogs and natural metabolites of $1\alpha,25(OH)_2D_3$

Chapter 2

Direct Electrochemistry of Mouse Cytochrome P450 27B1 in Surfactant Films

2.1 Introduction

Recent research on the electrochemistry of cytochrome P450s (CYPs) has focused on elucidating their electron transport pathways and their development for use in biosensors and bioreactors [67, 68, 69, 70, 71, 72, 73, 74]. However, heterogeneous electron transfer is difficult to achieve in many oxidoreductases [75, 76], especially with CYPs because membrane-bound enzymes exhibit a general instability when solubilized and the heme active-site is often buried within the protein. Much effort has been made to overcome the aforementioned issues. To date, coating an electrode surface with a surfactant film has been a successful method to facilitate direct electron transfer to heme-containing proteins such as myoglobin and CYP101 [72, 77, 78]. The stereoselective hydroxylation of 25-hydroxyvitamin D_3 ($25(OH)D_3$) is catalyzed by CYP27B1. This reaction results in the formation of 1α,25-dihydroxyvitamin D_3 ($1\alpha,25(OH)_2D_3$), the biologically active form of vitamin D_3 [54, 79]. The CYP27B1-catalyzed 1α-hydroxylation reaction required the uptake of two electrons from NADPH via an

electron transport chain consisting of two proteins: a FAD-containing adrenodoxin reductase (ADR) and an iron-sulfur protein, adrenodoxin (ADX) [54]. Recently, mouse CYP27B1 has been overexpressed in *Escherichia coli*, purified, and biochemically characterized [80]. As such, the availability of recombinant CYP27B1 makes possible its electrochemical characterization. In this chapter, we report direct electrochemistry of recombinant mouse CYP27B1 immobilized on an edge-plane pyrolytic graphite (EPG) electrode coated with a thin didodecyldimethylammonium bromide (DDAB) film. The electrochemical characterization of CYP27B1 presented in this chapter represents a first step toward measuring 25(OH)D_3 electrochemically.

2.2 Methods

2.2.1 Materials

The expression plasmids for mouse CYP27B1 (pKCHis-m1α) and GroEL/ES (pGro12) were kindly provided by Dr. T. Sakaki (Toyama Prefectural University, Japan). Synthetic 25(OH)D_3 and 1α,25(OH)$_2D_3$ were generous gifts from Dr. M.R. Uskoković (Hoffmann-La-Roche, Nutley, NJ). The Amplex Red hydrogen peroxide/peroxidase assay kit was purchased from Invitrogen. Ni-NTA affinity resin was purchased from Qiagen, PD-10 columns from GE Healthcare, and centrifugal filter devices (Amicon Ultra-15 30,000 NMWL) from Millipore. DDAB was purchased from Aldrich. EPG disk electrodes were purchased from Pine Instrument Company. All solutions were prepared in water purified by a Milli-Q system providing 18.2 MΩ resistivity. All other chemicals were reagent grade and used as received.

2.2.2 Expression and Purification of CYP27B1

Mouse CYP27B1 with a C-terminal tetra-histidine tag was co-expressed with molecular chaperonins GroEL/ES in *Escherichia coli* and purified as described previously with minor modifications [80] (see Appendix A for detailed protocols). After purification, protein samples that yielded an absorbance ratio (A_{417}/A_{280}) greater than 1.0

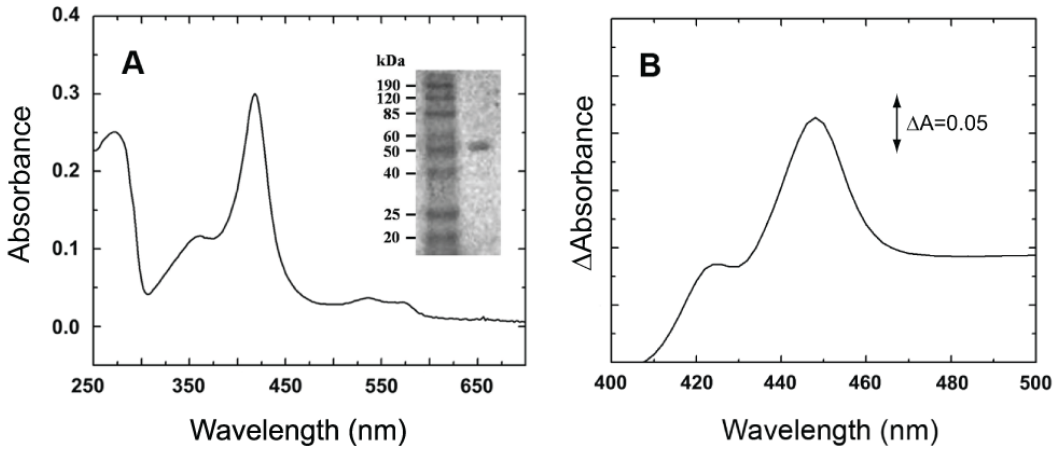

Figure 2.1: Spectral properties of the purified CYP27B1. (A) Absolute spectrum of purified CYP27B1 in 100 mM potassium phosphate, pH 7.4, 20% glycerol, 0.1% 3-[(3-Cholamidopropyl)dimethylammonio]-2-hydroxy-1-propanesulfonate, and 0.5 M NaCl was measured. (B) The concentration of purified CYP27B1 was determined from the reduced CO-difference spectrum (i.e., $Fe^{II}{\cdot}CO$ vs. Fe^{II}) using a difference extinction coefficient at 446 and 490 nm of $\epsilon_{446-490} = 91$ $mM^{-1}cm^{-1}$.

were collected and concentrated (Fig. 2.1). SDS-PAGE (inset of Fig. 2.1A) and an enzyme reconstitution assay were performed to confirm enzyme purity and activity, respectively. The enzymatic product, 1α,25$(OH)_2D_3$, was purified by HPLC (Fig. 2.2) and identified by gas chromatography-mass spectrometry (Fig. 2.3) in comparison with the corresponding synthetic standard. Aliquots of protein were flash-frozen in liquid nitrogen and stored at –80 °C until use.

2.2.3 Electrochemistry experiments

A three-neck round-bottom flask was utilized as the electrochemical cell containing an EPG disk (working, geometric area, A = 0.126 cm^2), a platinum gauze (counter), and a Ag/AgCl (reference, 0.197 V vs. NHE). All potentials in this study were reported with reference to Ag/AgCl. An EG&G Potentiostat/Galvanostat, model 263A, was used for cyclic voltammetry (CV) experiments. All CV experiments were performed at room temperature (22 ± 1 °C) with 4 mL of 50 mM potassium phosphate buffer (pH 7.4) containing 50 mM NaBr. Prior to performing CV, the working solution was fully deoxygenated (< 1.5 ppm) by purging with argon for at least 30 min. An argon

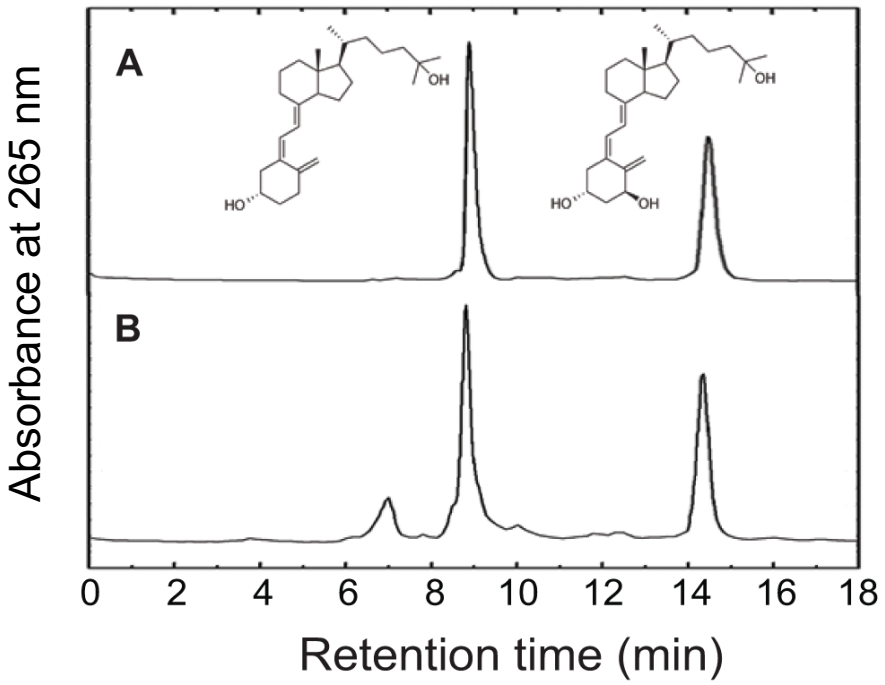

Figure 2.2: The CYP27B1 monooxygenase acitivity was measured in a reconstituted system consisting of the purified CYP27B1, ADR, ADX, and 25(OH)D_3 in a final volume of 1 mL of working buffer. After incubation at 37 °C for 5 min, the reaction was initiated by adding NADPH at a final concentration of 1 mM. The reaction was terminated by adding 6 mL of methanol/dichloromethane (1:2, v/v). After extraction, the organic phase was recovered and subjected to the HPLC analysis. HPLC profile of synthetic standards of 25(OH)D_3 and 1α,25$(OH)_2D_3$, eluted at $\sim$8.5 min and $\sim$14.3 min, respectively (panel A). HPLC profile of the lipid extract from a CYP27B1 reconstituted assay incubated with 25(OH)D_3 (panel B).

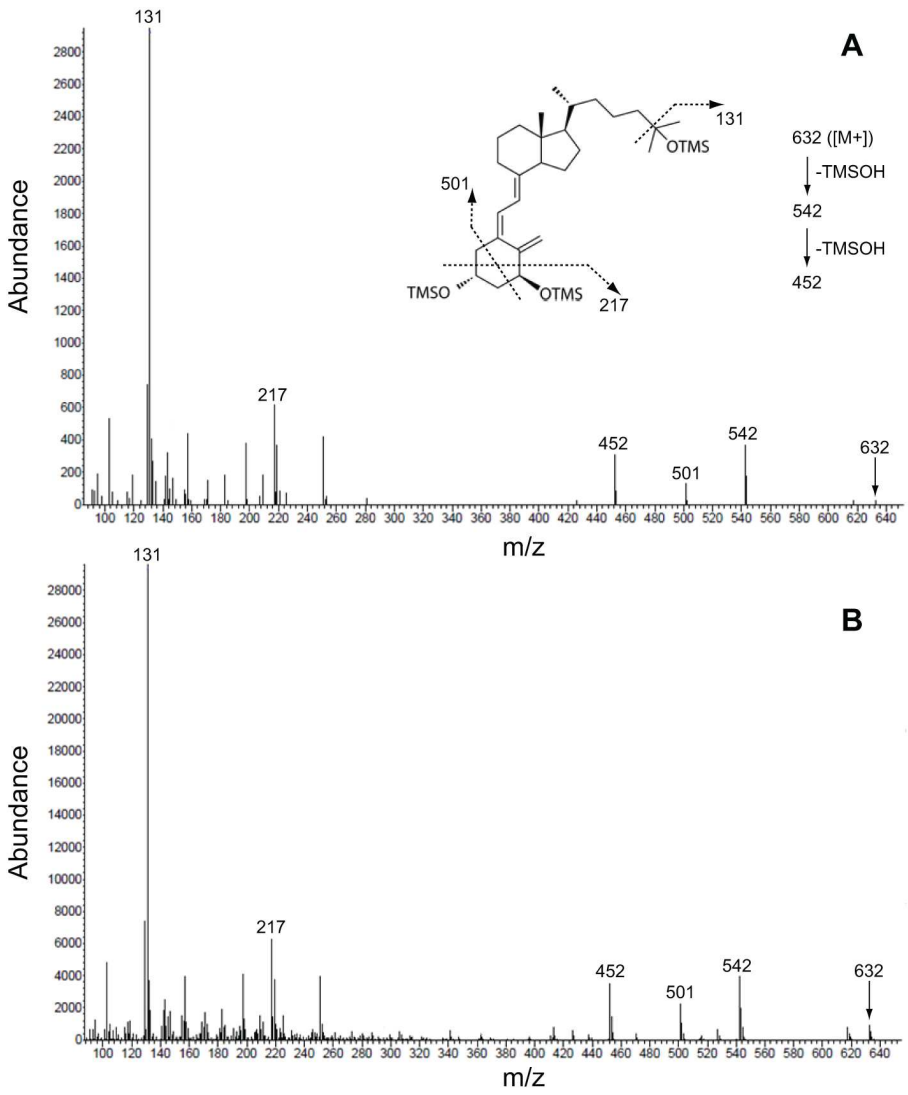

Figure 2.3: Mass spectra of enzymatic product (panel A) and synthetic standard 1α,25$(OH)_2D_3$ (panel B). Both enzymatic product and synthetic standard 1α,-25$(OH)_2D_3$ were subjected to trimethylsily (TMS) derivatization prior to analysis. The TMS derivative of enzymatic product exhibited a molecular ion ($[M^+]$) at m/z 632 followed by the sequential losses of TMSOH moieties (90 Da) to produce the fragments at m/z 542 and m/z 452. The ion fragment at m/z 131 accounts for the side-chain cleavage across C24-C25 while the fragments at m/z 501 ($[M–131]^+$) and m/z were formed upon cleavage across the A–ring. The fragmentation patterns of TMS-derivatized synthetic 1α,25$(OH)_2D_3$ were virtually identical to that of TMS-derivatized enzymatic product.

atmosphere also was maintained over the solution throughout the experiments.

2.2.4 Film preparation

DDAB films were fabricated as described previously for CYP101 with minor modifications [72, 81]. A freshly polished EPG disk electrode was coated with 15 μL of 10 mM DDAB in chloroform, which was evaporated at room temperature for 1 h. The DDAB-modified EPG electrodes were placed into 5 μL of 40 μM purified CYP27B1 for 1 h at 4 °C. The resulting CYP27B1/DDAB/EPG electrodes were dried under a stream of nitrogen prior to the experiments.

2.3 Results and Discussion

2.3.1 Direct electrochemistry of the CYP27B1/DDAB/EPG electrode

The cyclic voltammogram shown in Fig. 2.4A demonstrates the electrochemical reversibility of CYP27B1 immobilized on the DDAB/EPG electrode. No voltammetric peaks were observed in the absence of enzyme. CYP27B1 showed an average midpoint potential of –180 mV with a standard deviation of ± 5 mV across three different electrodes. The voltammetric peaks grew over the course of an hour (Fig. 2.4B), suggesting reorganization of the enzyme within the film and/or changes in the degree of hydration of the film [82]. The relationship between peak current and scan rate was linear up to 1 Vs^{-1} (Fig. 2.4D). This property is indicative of a thin film of electroactive species that is not under diffusion control as stated in Laviron theory. By integrating the oxidative and reductive peaks in the CV and applying Faradays law, the apparent surface coverage of electroactive CYP27B1 was calculated to be $(7.0 \pm 2.5) \times 10^{13}$ molecules per cm^2, suggesting multiple layers of CYP27B1 were electroactive. This amount of enzyme corresponds to ∼7% of the deposited enzyme. The oxidative and reductive peaks had approximately equal areas indicating only a single electron was transferred reversibly to the heme center and no oxygen reduction

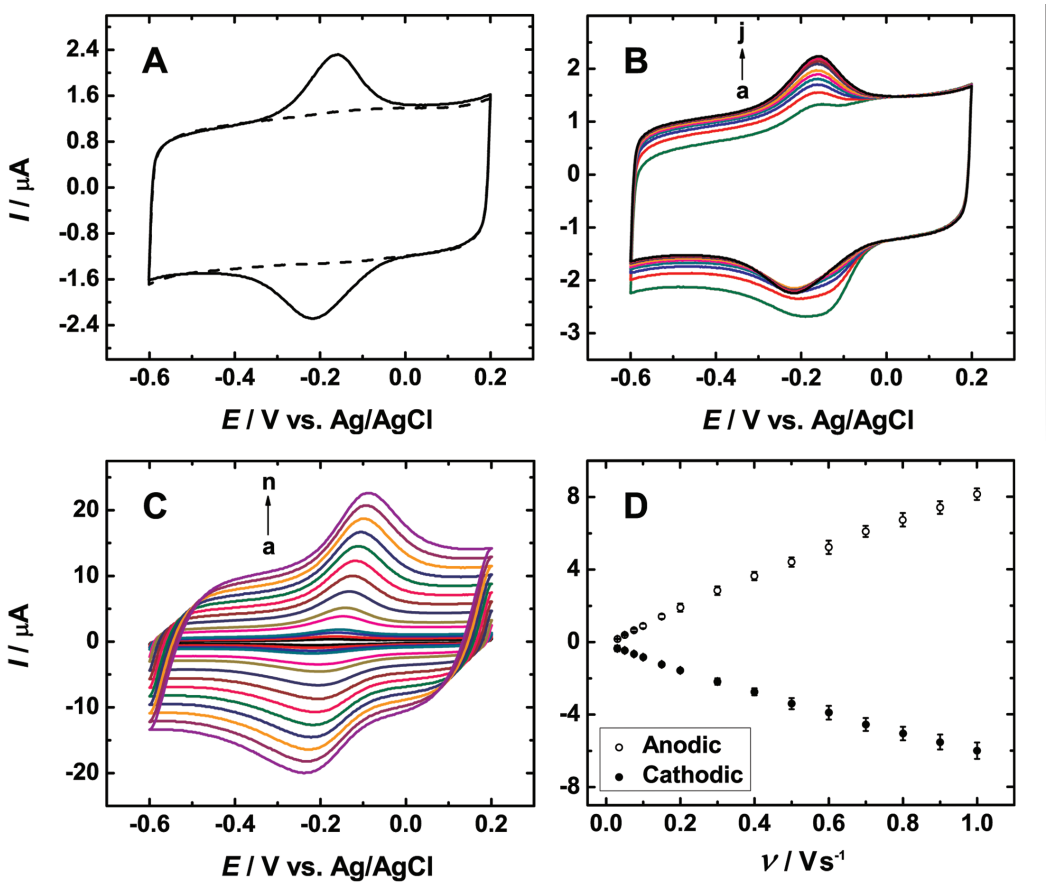

Figure 2.4: Cyclic voltammetry of CYP27B1 immobilized on a DDAB-modified EPG electrode. (A) The cyclic voltammogram was recorded in deoxygenated 50 mM potassium phosphate buffer including 50 mM NaBr, pH 7.4, at a scan rate of 0.1 Vs^{-1} for the CYP27B1/DDAB/EPG (solid) and DDAB/EPG (dashed) electrodes. (B) The voltammetric peaks grow over the course of an hour (a-j: scanned every 5 min over a period of an hour). (C) Cyclic voltammograms of CYP27B1/DDAB/EPG electrodes at different scan rates (a-n: 0.03, 0.05, 0.075, 0.1, 0.15, 0.2, 0.3, 0.4, 0.5, 0.6, 0.7, 0.8, 0.9, 1 Vs^{-1}). (D) The peak currents increased linearly as a function of scan rate up to 1 Vs^{-1}, indicating that CYP27B1 is confined to the surface of the electrode. Data points represent the mean of triplicate determinations ± S.D.

took place. The small standard deviation in the midpoint potential, apparent surface coverage of electroactive species, and the peak current demonstrate that electrode preparation was highly reproducible.

2.3.2 Determination of α and k_s

The electron-transfer coefficient (α) and the rate constant (k_s) were obtained from empirically fitted Laviron equations [83]. Irreversible electrochemistry (i.e., peak separation >200/n mV, taking n = 1) occurred when the scan rate exceeded 1.5 Vs^{-1} (Fig. 2.5A). Using Lavirons approach for diffusionless thin-layer voltammetry, the cathodic (E_{pc}) and anodic (E_{pa}) peak positions at various scan rates (υ) are expressed as Eq. (2.1) and (2.2):

$$E_{pc} = E^{\circ\prime} - \frac{RT}{\alpha nF}\ln\left(\frac{\alpha nF}{RTk_s}\right) - \frac{RT}{\alpha nF}\ln\upsilon \tag{2.1}$$

$$E_{pa} = E^{\circ\prime} + \frac{RT}{(1-\alpha)nF}\ln\left(\frac{(1-\alpha)nF}{RTk_s}\right) - \frac{RT}{(1-\alpha)nF}\ln\upsilon \tag{2.2}$$

where $E^{\circ\prime}$ is the formal potential, and R, T, F, and n are the universal gas constant, absolute temperature, Faraday's constant, number of moles of electrons transferred, respectively. The value of α can be determined from Eq. (2.3) by using the slopes from the linear plots of E_{pa} and E_{pc} vs. $\ln\upsilon$

$$\alpha = \frac{\dfrac{RT}{(1-\alpha)nF}}{\dfrac{RT}{(1-\alpha)nF} + \dfrac{RT}{\alpha nF}} = \frac{\delta_{pa}}{\delta_{pa} - \delta_{pc}} \tag{2.3}$$

where δ_{pa} and δ_{pc} are the slopes of linear region of the plot (Fig. 2.5B) when the difference of E_{pa} and E_{pc} (ΔE_p) is greater than 200 mV. The value of k_s can be determined by using Eq. (2.4):

$$\log(k_s) = \alpha\log(1-\alpha) + (1-\alpha)\log\alpha - log\left(\frac{RT}{nF\upsilon}\right) - \alpha(1-\alpha)\frac{nF\Delta E_p}{2.3RT} \tag{2.4}$$

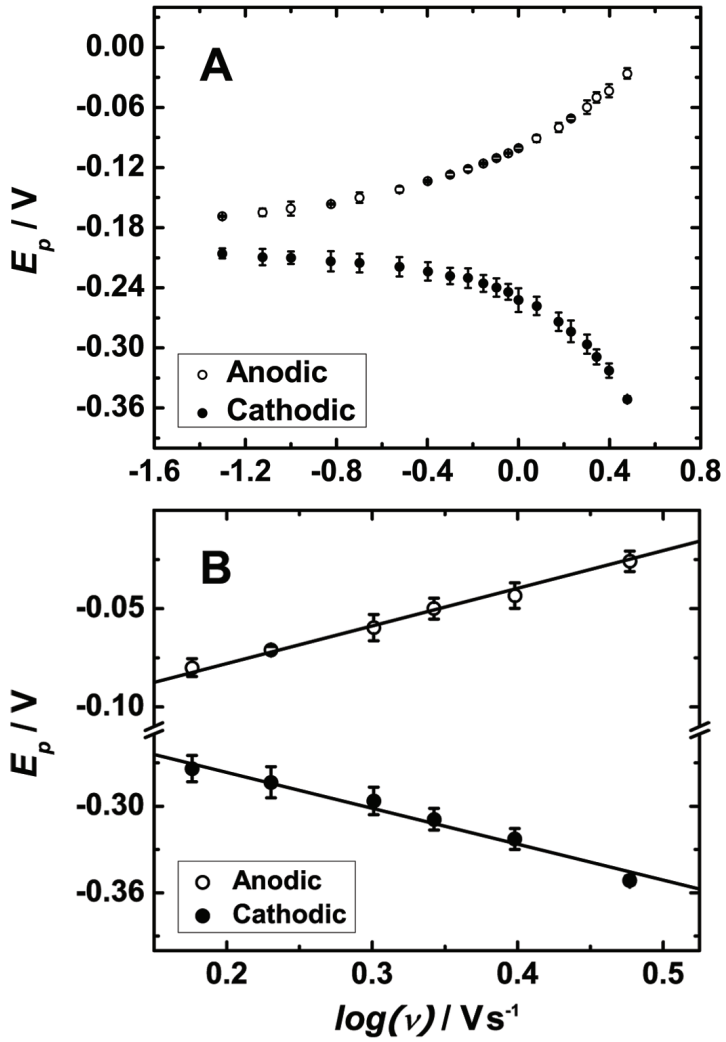

Figure 2.5: (A) Laviron plot: dependence of the anodic and cathodic peak potentials of a CYP27B1/DDAB/EPG electrode on the logarithm of the scan rates. (B) Linear segments of the Laviron plot showing the dependence of the peak potential (E_p) on the logarithm of scan rates. Data points represent the mean of triplicate determinations ± S.D.

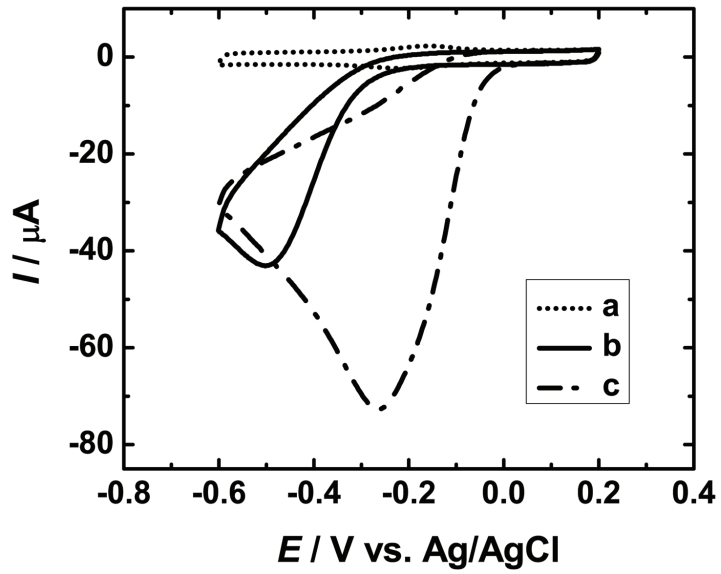

Figure 2.6: Cyclic voltammetric responses of CYP27B1/DDAB/EPG electrodes in buffer saturated with argon (a) or dioxygen (c). Negative control (DDAB/EPG electrodes) revealed dioxygen reduction at more negative potentials (b).

The resulting electron transfer coefficient and rate constant for heterogeneous electron transfer were determined to be 0.4 and 3.5 $\pm$ 0.6 s^{-1}, respectively.

2.3.3 Catalytic activity of immobilized CYP27B1

When the solution was saturated with dioxygen, a large increase in cathodic current was observed along with a disappearance of the anodic peak (Fig. 2.6). One source of this cathodic current reflects the enzymatic reduction of dioxygen to hydrogen peroxide (i.e., the formation of an $Fe^{II} - O_2$ complex followed by a second one-electron reduction to yield an iron-peroxo species [7]). The formation of hydrogen peroxide was confirmed by using the Amplex Red hydrogen peroxide/peroxidase assay kit. The reduction of dioxygen by DDAB/EPG electrodes occurred at more negative potentials, indicating that CYP27B1 significantly lowered the overpotential required for dioxygen reduction. The electrocatalytic reduction of the generated peroxide to water also may contribute to the observed catalytic current (i.e., the formation of an $O{=}Fe^{IV}$ complex followed by two electron reduction with diprotonation to yield water [73]).

After addition of catalase to the solution, a noticeable increase in cathodic current was observed, suggesting that the reduction of generated peroxide by CYP27B1 to water is slower than that of dioxygen to peroxide. Electrolysis reactions were performed at –0.6 V in oxygenated solutions in the presence of $25(OH)D_3$, however, no product formation was observed. It is possible that the active site of CYP27B1 is blocked by DDAB, a phenomenon that has been observed for other CYPs in surfactant films [70, 84].

2.3.4 The potential of the heme Fe^{III}/Fe^{II} redox couple of CYP27B1 in DDAB/EPG films

The measured midpoint potential of CYP27B1 in this study is considerably more positive to the redox potentials of CYPs reported previously [69, 85]. This shift in potential may be a consequence of the DDAB film. For example, it has been observed that the measured redox potential of the heme group shifts to more positive values (100∼300 mV) when CYP101 is embedded within DDAB films [68, 72] compared to values obtained in solution [67, 86]. One possible explanation for the observed shift in redox potential is electrostatic repulsion between ferric heme and DDAB head groups (both are cationic), which destabilizes the ferric state and shifts the equilibrium towards the ferrous state. Consequently, the potential of the ferric/ferrous redox couple shifts to a more positive value according to the Nernst equation. Furthermore, the Born equation [87] implies that the electrostatic free energy ($\Delta G = nF\Delta E$) of the heme group changes because of local differences in the dielectric constant of the hydrophobic tails of DDAB compared to the polar environment of the bulk electrolyte. Such effects have been discussed in the literature for other heme-containing enzymes [88, 89].

2.4 Acknowledgements

I thank Dr. G.S. Reddy for his help with HPLC analysis and Prof. T. Sakaki for generous provision of plasmid pKCHis-m1α encoding mouse CYP27B1. I also acknowledge financial support from the F.M. Becket Summer Fellowship of the Electrochemical Society.

Chapter 3

Conformational Transitions of Mouse Cytochrome P450 27B1 Induced by Surfactant Films Upon Immobilization

3.1 Introduction

Cytochrome P450s (CYPs) are heme-thiolate monooxygenases that play important roles in the synthesis of endogenous compounds such as fatty acids and steroids as well as the metabolism of xenobiotics using an electron transport system dependent on NAD(P)H and other redox cofactors [7]. In recent years, CYPs in vitro have been targeted for exploitation in bioreactors and biosensors [70, 71, 73]. One common yet simple approach is the direct electrochemical reduction of CYPs, but this method is often limited by poor electronic coupling between the deeply buried heme of CYPs and the electrode. Pioneered by Rusling et al. [78], several CYPs [68, 72, 74, 84, 90, 91, 92] have been incorporated successfully into surfactant films on electrodes to facilitate electron transfer.

Table 3.1: Summary of the immobilization strategies used for CYPs where heterogeneous electron transfer rates (k_s) and product generated by electrode–driven catalysis.

CYP	Electrode/modification	k_s [s^{-1}]	Product formation	Ref.
119A2	BPG† / None	550	No	[96]
119A2	PFC/PEO	35.1	No	[97]
101	GC/MT	152	No	[93]
102A1	BPG/DDAB+PSS	30	No	[94]
102A1	BPG/SDS	10	No	[84]
2C9	EPG/DDAB	150	No	[100]
2C9	Au/MUA/OT	6-31	Yes	[101]
2C17	EPG/DDAB	164	No	[74]
2C18	EPG/DDAB	–	No	[102]
2C19	EPG/DDAB	–	No	[102]
2E1	GC/DDAB	–	Yes	[70]
2E1	GC/PDDA	2	Yes	[70]
2E1	Au/cystamine-maleimide	10	Yes	[70]
2E1	Au/DTME	–	Yes	[103]
3A4	Au/MPA/PDDA	–	Yes	[82]
2B4	GC/clay/Tween20	–	Yes	[73]
2B6	GC/Au-NP/chitosan	0.5-16.4	Yes	[104]
2B6	GC/ZD/Pt colloidal/PLL	0.16-15.49	No	[98]
27B1	EPG/DDAB	3.5	No	Chapter 1

† BPG, basal-plane pyrolytic graphite; PFC, perfluorocarbon; PEO, poly(ethylene oxide); GC, glassy carbon; MT, montmorillonite; DDAB, didodecyldimethylammonium bromide; PSS, poly(styrenesulfonate); SDS, sodium dodecyl sulfate; EPG, edge-plane pyrolytic graphite; MUA, 11-mercaptoundecanoic acid; OT, octanethiol; PDDA, poly(diallyldimethylammonium chloride); DTME, dithio-bismaleimidoethane; MPA, 3-mercapto-1-propene sulfonic acid; Au-NP, gold nanoparticle; ZD, zirconium dioxide; PLL, poly-L-lysine

However, lack of electrode-driven CYP biocatalysis when using synthetic surfactant (e.g., didodecyldimethylammonium bromide (DDAB)) films has been frequently reported [68, 69, 74, 84, 92, 93, 94, 95, 96, 97, 98, 99]. Moreover, demonstration of successful catalytic activity of immobilized CYPs has been difficult to achieve despite various strategies used for immobilization have been utilized (see Table 3.1).

In this chapter, the effect of DDAB on the structure of mouse CYP27B1 was investigated with respect to its inability to produce enzymatic product via electrode–driven catalysis, which was observed in our previous study [92]. The spectroscopic data for CYP27B1 in DDAB dispersions suggest that the structural integrity of CYP27B1-bound heme is perturbed by the surfactant leading to the formation of a P420 isomer. However, despite the formation of the P420 isomer reduction of dioxygen on CYP27B1/DDAB/EPG electrodes was observed. One prominent cathodic peak appeared at low concentration of dioxygen whereas another cathodic peak emerged at more negative potential when the concentration of dioxygen is gradually increased. This work provides an unequivocal explanation for a long-standing problem in the field of electrode–driven biocatalysis where the catalytic activity of CYPs is annihilated due to the formation of P420 isomer which is induced by the surfactant environment.

3.2 Materials and Methods

3.2.1 Chemicals and solutions

DDAB and Hemin were purchased from Sigma-Aldrich. EPG disk electrodes were purchased from Pine Instrument Company. The Amplex Red hydrogen peroxide/peroxidase assay kit was purchased from Invitrogen. 25-hydroxyvitamin D_3 ($25(OH)D_3$) and 1α,25-dihydroxyvitamin D_3 ($1\alpha,25(OH)_2D_3$) were purchased from Biomol. The working solution for all experiments consisted of 50 mM potassium phosphate (KPi) buffer (pH 7.4) containing 50 mM NaBr. All other chemicals were reagent grade and used as received.

3.2.2 Enzyme preparation

Mouse CYP27B1 was co-expressed with molecular chaperonins GroEL/ES in Escherichia coli and purified as described [92]. Adrenodoxin reductase (ADR) and adrenodoxin (ADX) were provided by Dr. A.J. Annalora (The Scripps Research Institute, La Jolla, CA). To ensure the monooxygenase activity of purified CYP27B1, the reconstituted CYP27B1 assay was performed in a buffer containing 100 mM KPi (pH 7.4), 0.1% CHAPS, 2 μM ADX, 0.5 μM ADR, 0.5 μM CYP27B1, 1 μM 25(OH)D_3, and 1 mM NADPH. Aliquots of protein were flash-frozen in liquid nitrogen and stored at –80 °C until use.

3.2.3 Film preparation

DDAB films were fabricated as described with minor modifications [72]. A freshly polished EPG disk electrode was coated with 15 μL of 10 mM DDAB in chloroform, which was evaporated at room temperature for 30 min. The DDAB-modified EPG electrodes were placed into 10 μL of 20 μM purified CYP27B1 for 1 h at 4 °C. The resulting electrodes were dried under a stream of nitrogen prior to the experiments. Analogous films with Hemin were prepared under the same conditions as above, except that 30 μL of 2.5 mM Hemin in chloroform were used in place of CYP27B1.

3.2.4 Electrochemical apparatus

A three-neck round-bottom flask was utilized as the electrochemical cell containing an EPG disk (geometric area, A = 0.126 cm^2) working electrode, a platinum gauze counter electrode, and a Ag/AgCl (0.197 V vs. NHE) reference electrode. An EG&G Potentiostat/Galvanostat (model 263A) was used for cyclic voltammetry (CV) experiments at room temperature. Prior to performing CV experiments, the working solution was deaerated by purging with argon (Ar) for 30 min. An Ar atmosphere also was maintained over the solution throughout the experiments. High-purity dioxygen (O_2) or carbon monoxide (CO) was purged through the solution when necessary.

3.2.5 Measurement of CO difference spectra of reduced CYP27B1 in the presence of DDAB

The CO difference spectra of reduced CYP27B1 were measured with a UV-Vis spectrophotometer (Cary 500) at ambient temperature. Prior to measurement, the solution of CYP27B1 (5.5 μM) was mixed with DDAB (100 μM) for 10 min. Sodium dithionite was added to the reaction solution followed by a 1 min purge with CO.

3.3 Results and Discussion

3.3.1 Effects of DDAB on the structural integrity of CYP27B1

Electrocatalytic conversion of 25(OH)D_3 into 1α,25$(OH)_2D_3$ was examined using CYP27B1/DDAB/EPG electrodes as described [12]. As seen in other electrode–driven systems involving CYPs [68, 70, 74, 84, 92, 93, 94, 95, 96, 97, 98], CYP27B1 immobilized to the surface of an electrode was unable to catalyze the hydroxylation of 25(OH)D_3. To determine if the surfactant itself perturbs the enzymatic activity of CYP27B1, CO difference spectra of reduced CYP27B1 were measured in the presence of DDAB. As shown in Fig. 3.1A, the absorption maximum of CYP27B1 shifts from 450 nm to 422 nm, indicating that DDAB induces the formation of the P420 isomer, a biologically inactive form of the enzyme. Inactivation of CYP27B1 by DDAB was confirmed when an *in vitro* reconstituted assay did not produce 1α,25$(OH)_2D_3$ in the presence of DDAB (Fig. 3.1B). Our results are consistent with previous studies [105, 106] that showed the structural integrity of CYP102A1 was perturbed when the protein was immobilized on surfaces modified with a surfactant or charged polymers. Immobilization of CYP102A1 on theses surfaces produced the P420 isomer, which carries an electron-deficient iron center due to weakening of the iron-thiolate interaction between the heme and the protein backbone [105]. Such an effect appears as a large positive shift in the potential of the heme in the CVs of immobilized CYPs [68, 70, 74, 84, 92].

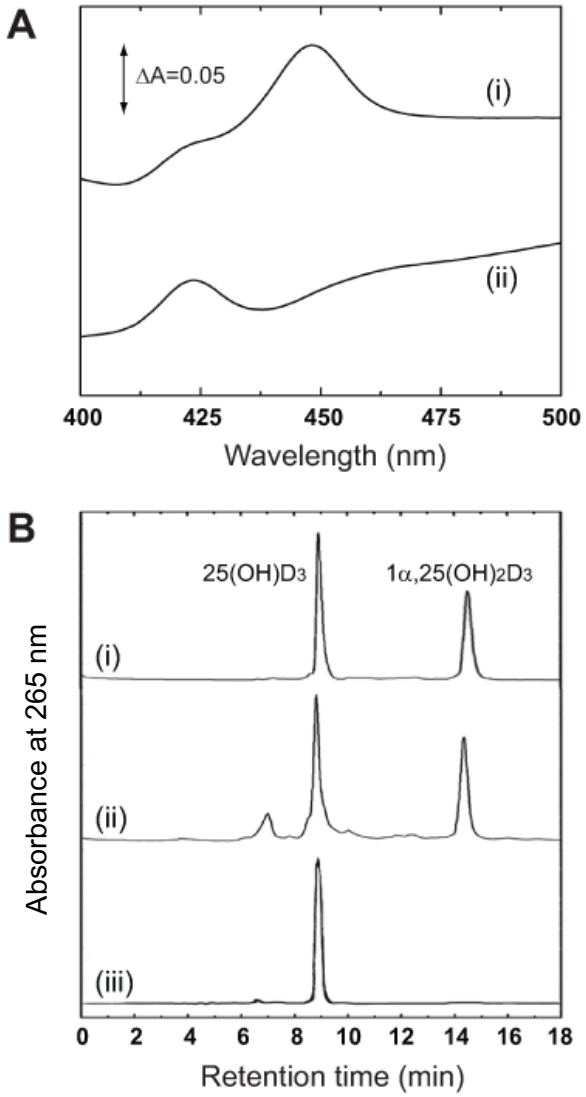

Figure 3.1: (A) CO difference spectra of reduced CYP27B1 (5.5 μM) in the absence (i) and presence of DDAB (100 μM) (ii) at ambient temperature. (B) Straight-phase HPLC profiles of synthetic standards of 25(OH)D_3 and 1α,25$(OH)_2D_3$ (i); and of extracts taken from an in vitro reconstituted assay in the absence (ii) or presence of DDAB (iii). Lipids were extracted from the enzyme reaction mixture and subjected to HPLC analysis using a Waters System Controller (Millennium 3.2). Resolution of vitamin D metabolites was achieved using a Zorbax-SIL column (250 mm 4.6 mm) (Dupont, Wilmington, DE) eluted with 20% isopropanol in hexane at a flow rate of 2 mL/min. A model 996 photodiode array detector (Waters, Milford, MA) was used to monitor lipids with the typical vitamin D chromophore (λ_{max} at 265 nm; λ_{min} at 228 nm).

3.3.2 Cyclic voltammetry in the absence of dioxygen

In deoxygenated conditions, cyclic voltammograms of CYP27B1/DDAB/EPG electrodes revealed a midpoint potential (E_{m}) centered at –190 ± 2 mV, which corresponds to the $Fe^{III/II}$ redox couple of the heme (Eq. 3.1) of CYP27B1 (inset to Fig. 3.2A). Typical for diffusionless thin-film voltammetry, the peak current increased linearly as a function of scan rate up to 1 Vs^{-1} [83]. Control experiments consisting of DDAB/EPG or EPG electrodes did not exhibit voltammetric peaks within the same potential window.

In the presence of CO, the value of E_{m} shifts positive by 35 mV (Fig. 3.2B), corresponding to the formation of a ferrous−CO adduct [107]. This adduct has been observed by others [68, 72, 108] and confirms that initial electron transfer occurs between the electrode and Fe^{III} of CYP27B1.

$$Fe^{III} + e^- \rightleftarrows Fe^{II} \tag{3.1}$$

$$Fe^{II} + O_2 \rightarrow Fe^{II} \cdots O_2 \tag{3.2}$$

$$[Fe^{II} \cdots O_2 \rightleftarrows Fe^{III} \cdots O_2^{\cdot -}] \overset{e^-}{\rightarrow} Fe^{III} \cdots O_2^{2-} \tag{3.3}$$

$$Fe^{III} \cdots O_2^{2-} \overset{H^+}{\rightarrow} Fe^{III} \cdots OOH \tag{3.4}$$

$$Fe^{III} \cdots OOH \overset{H^+}{\rightarrow} Fe^{III} + H_2O_2 \tag{3.5}$$

3.3.3 Electrocatalytic reduction of dioxygen

Addition of dioxygen to the electrolyte resulted in a significant increase in cathodic current (from ∼5 μA to ∼65 μA shown in Fig 3.2A), indicating the formation of Fe^{II} of CYP27B1, followed by fast dioxygen binding (Eq. 3.2). The cathodic current at –190 mV increased with each subsequent increase in the concentration of dioxygen until reaching a plateau current of –110 μA. After this point, any additional increase in the concentration of dioxygen resulted in the appearance of a second cathodic peak at –380 mV (initially appearing as a shoulder to the first cathodic peak). This second, more negative peak corresponds to the reduction of the ferric-superoxide complex $[Fe^{III} - O_2^{\cdot -}]$, resulting in the formation of ferric-peroxide complex $[Fe^{III} - O_2^{2-}]$ (Eq.

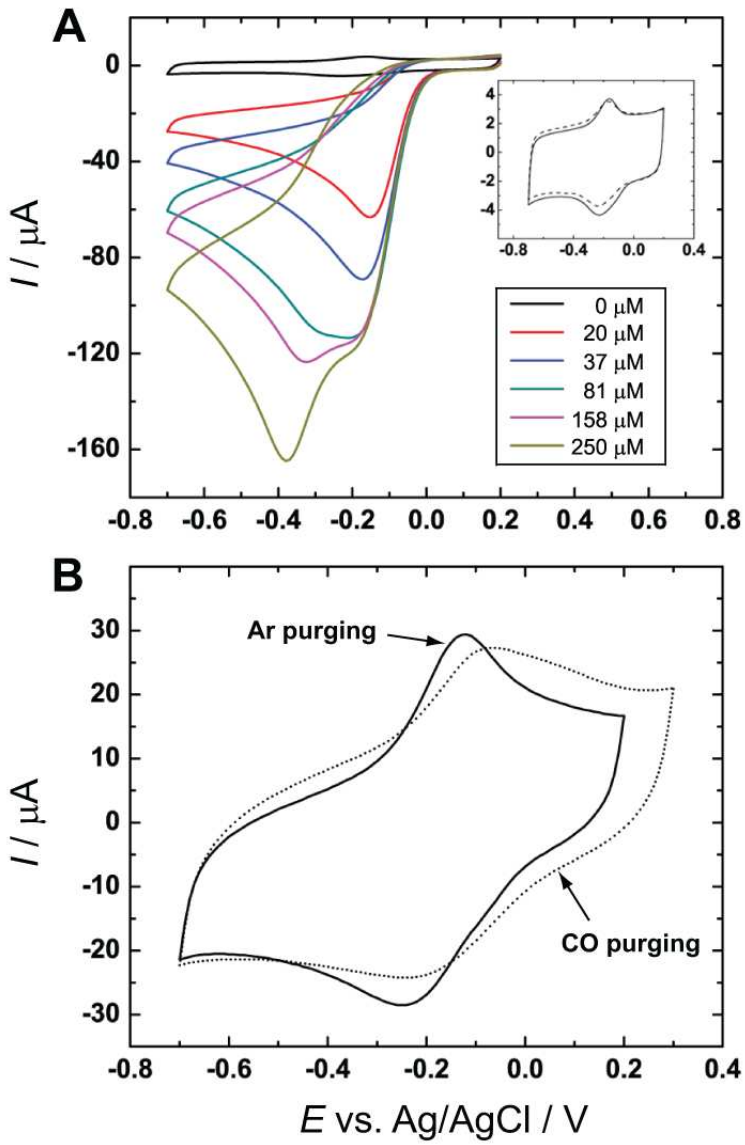

Figure 3.2: (A) Cyclic voltammograms of the CYP27B1/DDAB/EPG electrode at 0.2 Vs^{-1} in 50 mM KPi buffer including 50 mM NaBr, pH 7.4 with increasing amounts of pure dioxygen (0 to 250 μM) bubbled through the solution. The inset shows the initial cyclic voltammogram of CYP27B1/DDAB/EPG in a solution purged with Ar (solid) and subsequent to experiments with different amount of dioxygen, purged with Ar for 30 min (dashed). (B) Cyclic voltammograms of the same electrode after the solution was purged with CO for 5 min (dotted).

3.3), based on the following rationale. In the presence of dioxygen, reduction of Fe^{III} to Fe^{II} in the heme of CYP27B1 results in the formation of a ferrous-oxy complex [$Fe^{II} - O_2$]. Thus, increasing the amount of dioxygen results in an increase in the amount of $Fe^{II} - O_2$ formed at –190 mV. Once formed, $Fe^{II} - O_2$ complex is capable of undergoing an internal electron transfer to yield a $Fe^{III} - O_2^{\cdot -}$. Reduction of $Fe^{III} - O_2^{\cdot -}$ complex yields a ferric peroxide adduct $Fe^{III} - O_2^{2-}$, which can be protonated to give a ferric-hydroperoxide complex [$Fe^{III} - OOH$] (Eq. 3.4) [8]. Our data indicate that the reduction of $Fe^{III} - O_2^{\cdot -}$ depends on the concentration of dioxygen. Subsequent to the reaction shown in Eq. 3.4, a second protonation of $Fe^{III} - OOH$ on the unprotonated oxygen releases H_2O_2 via the two-electron peroxide shunt (Eq. 3.5). The formation of the H_2O_2 was confirmed with the Amplex Red hydrogen peroxide/peroxidase assay kit. Determining the number of electrons transferred to dioxygen using a rotating disk electrode and the Levich equation [109] was thwarted by the mechanical fragility of CYP27B1/DDAB films. Although the autooxidation of $Fe^{III} - O_2^{\cdot -}$ can produce superoxide, which disproportionates non-enzymatically to H_2O_2 and O_2 in aqueous media, this reaction is unlikely because the autooxidation process is slow compared to the one-electron reduction of $Fe^{III} - O_2^{\cdot -}$ shown in Eq. 3.3 [26].

Table 3.2: Midpoint potentials (E_{m}) for $Fe^{III/II}$ redox couple and cathodic peak potentials (E_{pc})† corresponding to dioxygen reduction taken from the CVs of different electrodes immersed in 50 mM KPi/50 mM NaBr (pH 7.4) and scanned at 200 mVs^{-1}.

Film	(E_{m} vs. Ag/AgCl)/mV	(E_{pc} vs. Ag/AgCl)/mV
DDAB/EPG	not present	–505 ± 1
Hemin/DDAB/EPG	–185 ± 2	–175 ± 2
CYP27B1/DDAB/EPG	–190 ± 2	–382 ± 2

† Cathodic peak potentials corresponding to the reduction of dioxygen were measured in electrolyte saturated with dioxygen (∼250 μM).

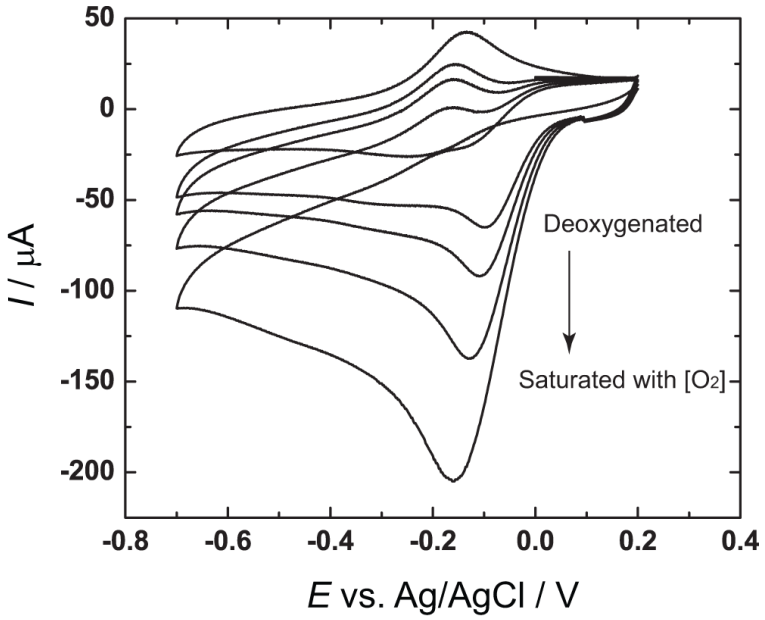

Figure 3.3: Cyclic voltammograms of the Hemin/DDAB/EPG electrode at 0.2 Vs^{-1} with increasing amounts of pure dioxygen. Experimental conditions are as described in Fig. 3.2.

3.3.4 Cyclic voltammetry with free heme in DDAB

After removal of O_2 by purging the solution with Ar for 30 min, the voltammogram on the CYP27B1/DDAB/EPG electrode was found to be nearly identical to the original voltammogram (inset to Fig. 3.2A). It should be noted that dioxygen reduction at a DDAB/EPG electrode (i.e., negative control) occurs at more negative potentials (Table 3.2). For comparison, a Hemin/DDAB/EPG electrode was examined under identical experimental conditions. The value for E_m of the $Fe^{III/II}$ redox couple in Hemin was similar to that of CYP27B1 (Table 3.2), however, only one cathodic peak potential (E_{pc}) was observed regardless of the amount of dioxygen present in the electrolyte (Fig. 3.3).

3.4 Conclusion

Our spectroscopic work indicates that DDAB is capable of inducing an inactive P420 isomer of CYP27B1, thereby affecting the catalytic activity of the enzyme. This finding is fully consistent with surface-enhanced resonance Raman investigations by

Todorovic *et al.* [110], which suggest that immobilization of P450 on modified silver surfaces perturbs the heme potential by decreasing the electron donor strength of the heme axial thiolate, ultimately producing a P420 isomer. Following this result, cyclic voltammograms of CYP27B1/DDAB films on EPG electrodes show that the P420 isomer of CYP27B1 is still able to catalyze the reduction of dioxygen. In this regard, two successive reductive peaks were observed − one prominent reductive peak appeared at low concentration of dioxygen whereas another reductive peak emerged at more negative potential by gradually increasing the concentration of dioxygen, which was not observed in the case of Hemin/DDAB/EPG electrodes.

Chapter 4

A New Insight Into the Role of Rat Cytochrome P450 24A1 in Metabolism of Selective Analogs of 1α,25-dihydroxyvitamin D_3

4.1 Introduction

The active form of vitamin D_3, 1α,25-dihydroxyvitamin D_3 (**1**), is a secosteroid hormone. Aside from its central role in regulating calcium homeostasis, **1** also displays other non-calcemic actions such as antiproliferative and proapoptotic activities against certain types of cancer cells. This finding led to the use of **1** as a possible drug in treatment of renal osteodystrophy, various cancers, and other proliferative disorders such as psoriasis [111, 112, 113]. However, the clinical use of **1** is limited mainly because of its side effect of hypercalcemia. To minimize the calcemic effect, numerous vitamin D analogs have been synthesized by adding structural modifications to one or more geographic regions of **1** including the A−ring, seco−B−ring, CD−ring, and/or the side chain as shown in Fig. 4.1. The reader is directed to reviews [42, 114, 115] for further details on vitamin D analogs.

Some of the structural modifications that are added to **1** are aimed to block metabolic inactivation of **1** so that the therapeutic effects of **1** within target cells can be prolonged. Metabolic inactivation of **1** is catalyzed by mitochondrial cytochrome P450 24A1 (CYP24A1), which is responsible for all the natural metabolites produced through C24, C23, and C26 oxidation pathways [61, 65, 116, 117] (see Fig. 1.9). Of these metabolic pathways, **1** mainly proceeds through C24 oxidation pathway which is initiated by C24 hydroxylation, followed by a series of side chain oxidations leading to the formation of the final metabolite, calcitroic acid [62, 118, 119]. The remaining two pathways initiated by C23 and C26 hydroxylations are minor metabolic pathways responsible for conversion of **1** to the final metabolite, calcitriol lactone [120]. For a comprehensive overview on vitamin D metabolism and the enzymes involved, the reader is referred to a recent review [44].

One group of analogs was synthesized with the aim to block metabolic inactivation of **1** through C23 and C24 oxidation pathways by adding 16-ene and 23-yne modifications to **1**. 1α,25-dihydroxy-16-ene-23-yne-vitamin D_3 (**2**), the archetype of these analogs, was found to have 4− to 12−fold higher potency than **1** in inducing differentiation and inhibiting proliferation of human myeloid leukemic cells without causing hypercalcemia [121, 122]. In a preliminary study, we investigated the metabolism of **2** in an isolated perfused rat kidney (IPK) and noted that **2** is slowly metabolized through only the C26 oxidation pathway resulting in the formation of a minor metabolite which was putatively identified as C26-hydroxy-**2** [123]. Preliminary results also indicated that **3** remained unmetabolized [124] while **4** was rapidly metabolized into two polar metabolites in the IPK (G.S. Reddy, unpublished data). Furthermore, we noted that **2** and **4** were metabolized only in the kidneys isolated from rats that were pretreated with **1**. Since the upregulation of *CYP24A1* gene expression and activity by **1** in an IPK is well established [125, 126], we speculated that CYP24A1 is the enzyme responsible for the metabolism of **2** and **4**. To prove this hypothesis, we examined the comprehensive metabolism of **2** and **4** using purified rat CYP24A1 in a reconstituted system. We did not include **3** in this study as it remained unmetabolized in an IPK despite highly upregulated CYP24A1. We noted that **2** is metabolized

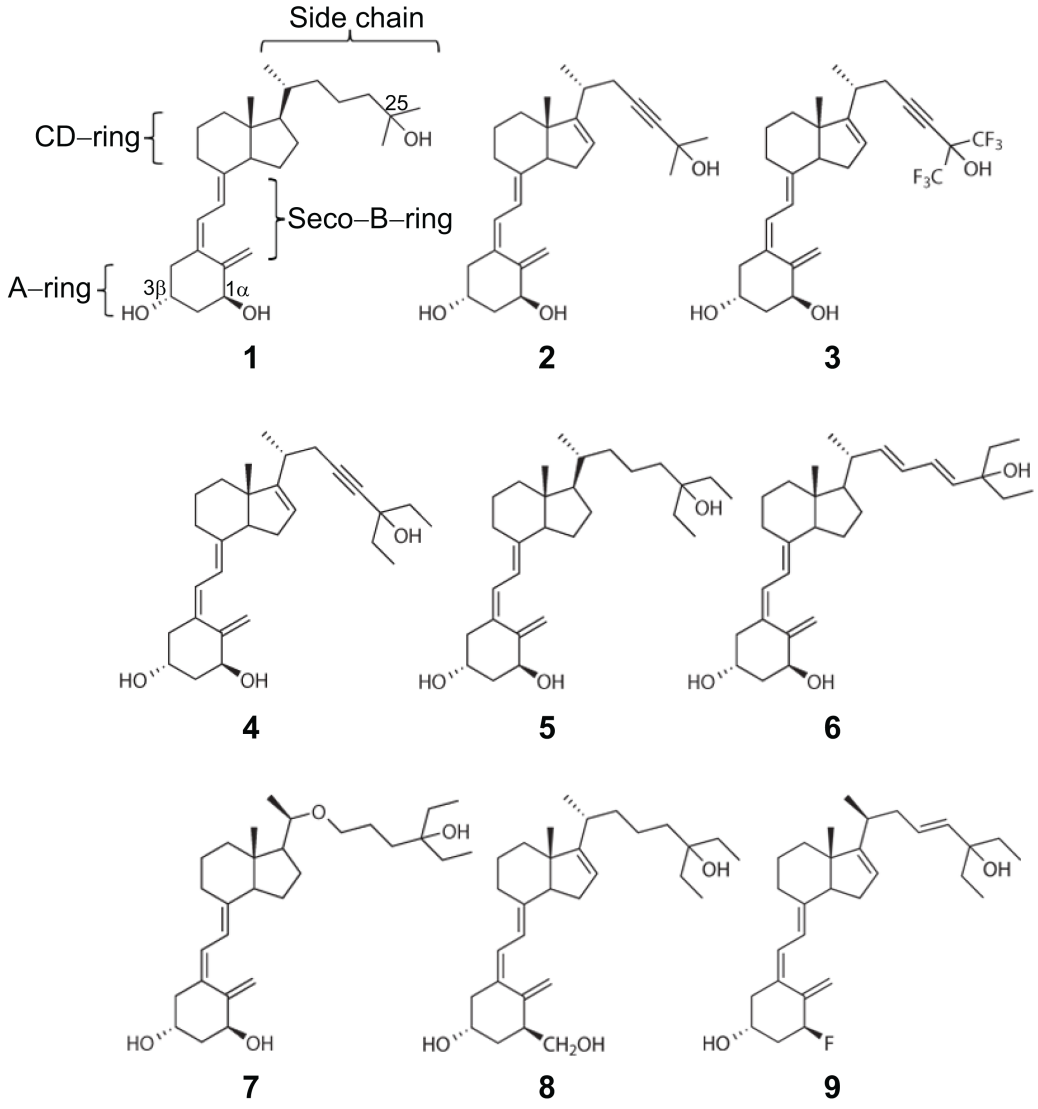

Figure 4.1: Chemical structures of 1α,25-dihydroxyvitamin D_3 (**1**) and its analogs: 1α, 25 -dihydroxy - 16 -ene-23-yne-vitamin D_3 (**2**), 1α,25-dihydroxy-16-ene-23-yne-hexafluoro-vitamin D_3 (**3**), 1α,25-dihydroxy-16-ene-23-yne-26,27-dimethyl-vitmain D_3 (**4**), 1α, 25-dihydroxy-26, 27-dimethylvitamin D_3 (**5**), 1α,25-dihydroxy-22,24-diene-24,26,27-trihomo-vitamin D_3 or EB1089 (**6**), 1α, 25-dihydroxy -20 - epi -22 - oxo -24a-homo-26, 27-dimethyl-vitamin D_3 or KH1060 (**7**), 1α -hydroxymethyl - 3β ,25-dihydroxy-16-ene-26,27-bishomo-vitamin D_3 (**8**), and 1α-fluoro-25-hydroxy-16,23E-diene-26,27-bishomo-20-epi-vitamin D_3 (**9**).

into a single metabolite identified as C26-hydroxy-**2** while **4** is metabolized into two metabolites identified as C26-hydroxy-**4** and C26a-hydroxy-**4**.

The structural modification of extending the distal carbons of the sterol side chain with methyl groups seen in **4** has been incorporated into the synthesis of many other analogs (examples shown in Fig. 4.1). All these analogs were found to have remarkable biological properties when compared to **1**, for some of them sufficiently promising to enter clinical drug development [127, 128, 129, 130]. In particular, analog **6** (EB1089) has been extensively studied including its metabolism [131, 132, 133, 134, 135]. It was shown that **6** was metabolized into two metabolites identified as C26-hydroxy-**6** and C26a-hydroxy-**6** and the enzyme responsible for its metabolism was not CYP24A1 [132]. To this end, even though the metabolic fate of **4** and **6** are indistinguishable, it is interesting to note that out of the two analogs, only **4** is metabolized by CYP24A1. Recently, the crystal structure of rat CYP24A1 has been published [60]. We took this as an opportunity to gain an insight into the structural determinants of substrate recognition, as a means to understand the metabolic profiles of the analogs **2**, **4**, and **6** by performing a molecular docking analysis.

4.2 Materials and Methods

4.2.1 Vitamin D compounds and chemicals

Crystalline **1**, **2**, **4**, 25-hydroxyvitamin-D_3 (25(OH)D_3), and 1α,25,26-trihydroxy-16-ene-23-yne-vitamin D_3 (1α,25,26$(OH)_3$-16-ene-23-yne-D_3) were synthesized at Hoffmann-La-Roche (Nutley, NJ). Analog **6** was generously provided by Dr. J. Welsh (State University of New York at Albany, Rensselaer, NY). All the known natural metabolites of **1** which include 1α,24(R),25-trihydroxyvitamin D_3 (1α,24(R),25$(OH)_3D_3$), 1α,25-dihydroxy-24-oxo-vitamin D_3 (1α,25$(OH)_2$-24-oxo-D_3), 1α,23(S),25-trihydroxy-24-oxo-vitamin D_3 (1α,23(S),25$(OH)_3$-24-oxo-D_3), and 1α,23-dihydroxy-24,25,26,27-tetranorvitamin D_3 (1α,23$(OH)_2$-24,25,26,27-tetranor-D_3) were biologically synthesized using the IPK as previously described [62]. All

other chemicals were purchased from Sigma-Aldrich (St. Louis, MO) and used without further purification.

4.2.2 Preparation of enzymes

Recombinant rat CYP24A1 (WT, $\Delta 2-32$) was expressed in *E. coli* (DH5α-FIQ) and purified as described [136]. Purified CYP24A1 samples with A_{417}/A_{280} ratio exceeding 1.0 were considered pure for biochemical assay. Bovine adrenodoxin (ADX) and adrenodoxin reductase (ADR) were expressed and purified as described with minor modifications [136, 137, 138]. Spectral purity indexes of ADX (A_{414}/A_{276}) and ADR (A_{452}/A_{278}) used in the present study were 0.9 and 0.1, respectively [136, 139]. All enzymes were purified using the AKTA^{TM} FPLC system (GE Healthcare, Chalfont St. Giles, UK) and were stored at –80 °C prior to use.

4.2.3 CYP24A1 reconstitution assay

The CYP24A1 reconstitution assay consisted of a mixture of substrates (5 μM), ADX (0.5 μM), ADR (0.5 μM), and CYP24A1 (0.5 μM) in 1 mL of 50 mM potassium phosphate buffer, pH 7.4. After preincubation at 37 °C for 5 min, the reaction was initiated by adding NADPH at a final concentration of 1 mM. After incubation at 37 °C for 5 min, the reaction was terminated by adding 2 mL of methanol followed by the addition of 1 μg of 25(OH)D_3 as an internal standard. The reactants were extracted by adding 4 mL of dichloromethane and subjected to HPLC analysis. A time course study of the metabolism of **2** and **4** was performed in a similar manner as described above except that the buffer contained 0.1 μM ADX, 0.1 μM ADR, and 0.4 μM CYP24A1 over the time period 5–60 min.

4.2.4 Purification of vitamin D metabolites using High-performance liquid chromatography (HPLC)

Lipids were extracted from the enzyme reaction mixture and subjected to HPLC analysis according to a standard procedure [62] using a Waters System Controller

(Millennium 3.2). Resolution of vitamin D metabolites was achieved using a Zorbax-SIL column (250 mm × 4.6 mm) (Dupont, Wilmington, DE) eluted with two different solvent mixtures at a flow rate of 2 mL/min: (1) 20% isopropanol in hexane for initial separation (2) 10% isopropanol in hexane for enhanced resolution of the metabolites. A model 996 photodiode array detector (Waters, Milford, MA) was used to monitor lipids with the typical vitamin D chromophore (λ_{max} at 265 nm and λ_{min} at 228 nm).

4.2.5 Gas chromatography/Mass spectrometry (GC/MS)

GC/MS analysis was performed using an Agilent GC system 6890 equipped with a mass-selective detector (MSD5973). The metabolites of interest obtained from HPLC were subjected to trimethylsilyl (TMS) derivatization using Power SIL-Prep (Alltech Associates, Deerfield, IL) in anhydrous acetonitrile (50:50, v/v) at 70 °C for 15 min. The derivatized metabolites (final concentration, 10 μg/mL) were subjected to GC/MS analysis using a HP-5MS GC capillary column (30 m × 0.25 mm × 0.25 μm, 5% phenyl siloxane) with helium as a carrier gas at a flow rate of 0.8 mL/min. The oven temperature was set at 150 °C and ramped at a rate of 10 °C/min to reach the final temperature of 300 °C. Full-scan electron impact spectra across the mass range of m/z 50–700 were acquired in each run and the final spectra were obtained after background correction.

4.2.6 Periodate oxidation of vitamin D metabolites

The metabolites of **4** produced by CYP24A1 were purified as described above. Each metabolite (1 μg) in 15 μL of methanol was subjected to treatment with 15 μL of 5% (w/v) sodium periodate at 25 °C for 30 min. The products of the reaction were dried under nitrogen and subjected to HPLC analysis.

4.2.7 Substrate-induced difference spectra

Before proceeding to perform docking analysis, the substrate-induced difference spectra were measured with a Cary Model 500 double-beam spectrophotometer to ensure

the ability of **6** to bind to the active site of CYP24A1 along with **1**, **2**, and **4**. After obtaining a baseline with the purified CYP24A1 (0.5 μM) preparation in both reference and sample cuvettes, the vitamin D compounds (1 μM) were added to the sample cuvette while the equal volume of the vehicle solvent (absolute ethanol) was added to the reference cuvette. The final concentration of ethanol was less than 1% (v/v) in all cases.

4.2.8 Ligand docking simulations using AutoDock 4.2

The simulated docking of vitamin D compounds including **1**, **2**, **4**, and **6** into the open conformation of rat CYP24A1 crystal structure (PDB ID: 3K9V, copy A) was performed using AutoDock 4.2 [140, 141] with a crystal structure–calibrated docking protocol as described [60]. The topology and parameters for all analogs were generated using the PRODRG server [142] and used as input files for AutoDock 4.2.

4.3 Results

4.3.1 Metabolism studies of 1, 2, and 4 with an *in vitro* CYP24A1 reconstituted system

In this chapter, we only studied the metabolism of **2** and **4** in relation to **1**, but did not include **6** since it was previously shown that **6** was not metabolized by CYP24A1 [27]. The HPLC profiles of lipid soluble metabolites of **1**, **2**, and **4** produced by CYP24A1 are shown in Fig. 4.2. Within 5 min, extensive metabolism of **1** led to several polar metabolites which were identified as 1α,24(R),25(OH)$_3$D$_3$ (d*), 1α,25(OH)$_2$-24-oxo-D$_3$ (a*), 1α,23(S),25(OH)$_3$-24-oxo-D$_3$ (c*), 1α,23(OH)$_2$-24,25,26,27-tetranor-D$_3$ (b*), and calcitriol lactone (e*) based on co-migration with known standards (Fig. 4.2A). **2** was metabolized into a single metabolite (f*) while **4** was metabolized into two metabolites (g* and h*), all of which were more polar than their respective parent compounds (Fig. 4.2B and 4.2C). The metabolites of **2** and **4** were produced in a quantity sufficient for their structural identification by GC/MS analysis and periodate

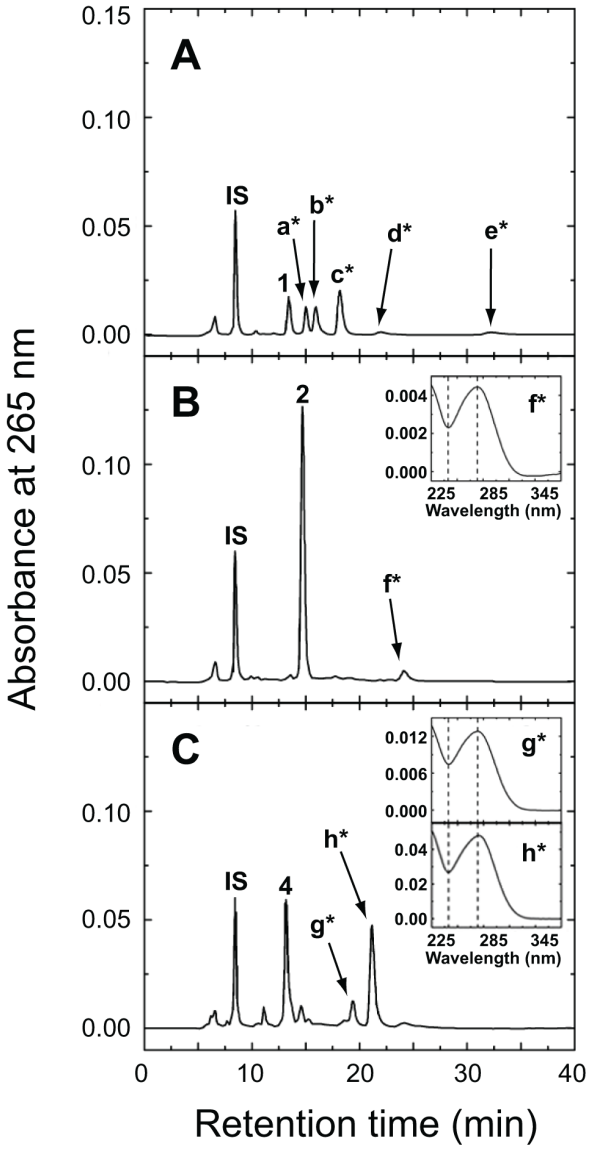

Figure 4.2: HPLC profiles of lipid soluble metabolites of **1**, **2**, and **4** produced by CYP24A1. Details of experimental conditions are given in the Methods section. HPLC analysis of lipid extracts of samples was performed using a Zorbax-SIL column (250 mm × 4.6 mm) eluted with 10% isopropanol in hexane at a flow rate of 2 mL/min. 1 μg of 25(OH)D_3 (IS) was added to each sample before lipid extraction as an internal standard to quantify the efficiency of the extraction step. As expected, **1** was metabolized into 1α,24(R),25((OH)$_3$$D_3$ (d*), 1α,25(OH)$_2$-24-oxo-D_3 (a*), 1α,23(S),25(OH)$_3$-24-oxo-D_3 (c*), 1α,23(OH)$_2$-24,25,26,27-tetranor-D_3 (b*), and calcitriol lactone (e*) (panel A). **2** was metabolized into a polar metabolite f* (panel B) while **4** was metabolized into two polar metabolites, g* and h* (panel C). All the three polar metabolites possessed the typical vitamin D chromophore showing λ_{max} at 265 nm and λ_{min} at 228 nm (inset).

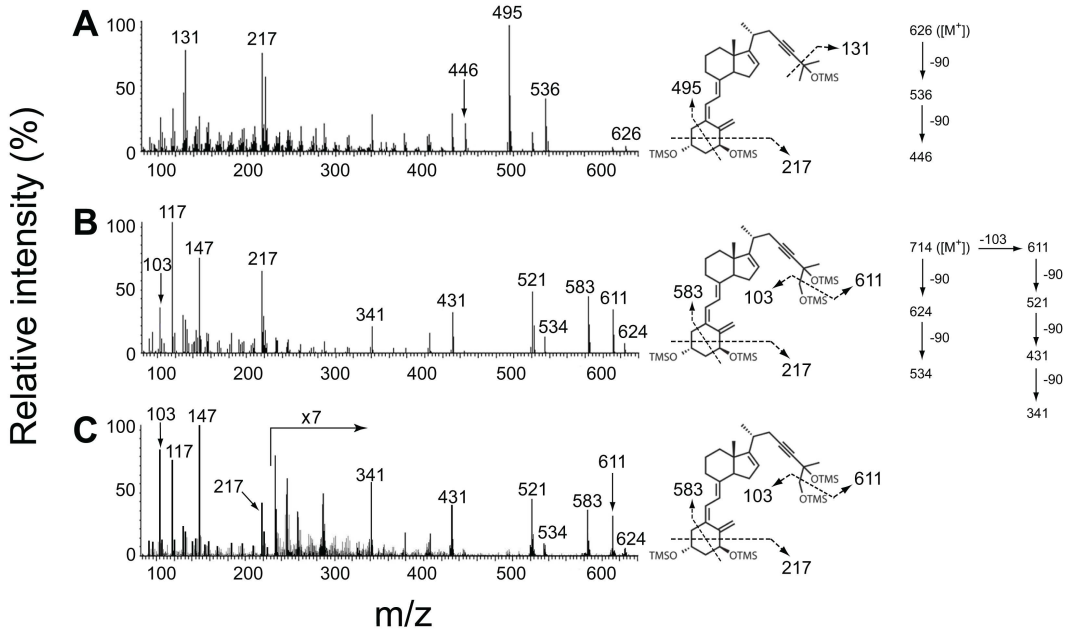

Figure 4.3: GC mass spectra of trimethylsilyl derivatives of **2** (A), f* (B), and synthetic standard of f* (C). All analyses were performed as described in the Methods section.

oxidation. Prior to GC/MS analysis, the final purity of each compound was tested by its characteristic vitamin D chromophore showing λ_{max} at 265 nm and λ_{min} at 228 nm.

4.3.2 Structural identification of metabolite of 2 using GC/MS

The metabolite of **2** was first isolated in our earlier study investigating the metabolism of **2** in an IPK and was identified putatively as C26-hydroxy-**2**. The results of this study were reported only in an abstract [123]. These preliminary results prompted us to chemically synthesize C26-hydroxy-**2**. Taking advantage of these earlier observations, we proceeded to identify the structure of the metabolite of **2** produced by CYP24A1.

We first obtained the mass spectrum of trimethylsilylated **2** for comparison with that of its metabolite f*. Its spectrum exhibited the molecular ion ($[M^+]$) at m/z 626 followed by the sequential losses of trimethylsilanol moieties (90 Da) to produce

thefragments at m/z 536 and m/z 446. Among other key signature ions are those involving fragmentations associated with A–ring. Significant are the characteristic fragment ions at m/z 217 (comprised of C1, C2, and C3) and m/z 495 ($[M–131]^+$), involving the loss of C2, C3, and C4, and which serve to establish the integrity of the A–ring (Fig. 4.3A). Finally, a fragment at m/z 131 is of major structural significance, arising from side chain cleavage across C24-C25 bond. This information provides a template in the interpretation of the spectrum of the metabolite f*.

The mass spectrum of trimethylsilylated f* (f^*_{TMS}) exhibited a fragment ion at m/z 624 as its highest detectable mass (Fig. 4.3B) but did not exhibit the molecular ion peak at m/z 714 since the latter is beyond the mass range of the instrument. However, the molecular mass can be inferred indirectly from consideration of the masses of key fragment ions. Specifically, the presence of a fragment ion at m/z 583 ($[M–131]^+$) can be related to a parent ion of m/z 714. Based on this finding, we concluded that metabolite f* differed from its parent compound by an additional hydroxyl group. Moreover, fragment ions at m/z 624 ($[M–90]^+$) and m/z 534 ($[M–(90\times2)]^+$) reflecting the sequential losses of TMSOH moieties further support the conclusion that they originate from a molecular species of m/z 714. The presence of a fragment ion at m/z 217 was an indication that the integrity of the A–ring is maintained and this ruled out the possibility of A–ring being the site of hydroxylation. The absence of a fragment ion at m/z 131 is indicative of a modification to the end of the side chain. The presence of a fragment ion at m/z 611 ($[M–103]^+$) representing a loss of [$\cdot CH_2OTMS$] group from the side chain of f^*_{TMS} suggested C26 as the possible site of hydroxylation. A fragment ion at m/z 147 [$(Me_3\text{-Si-O-Si-}Me_2)^+$] indicating the presence of two trimethylsilyloxy groups in close proximity [143] at C25 and C26, further confirmed C26 as the site of hydroxylation (Fig. 4.3B). Finally, it should be noted that mass spectral analysis of the trimethylsilylated synthetic standard of 1α,25,26$(OH)_3$-16-ene-23-yne-D_3 gave a fragmentation pattern virtually identical to that of f^*_{TMS} (Fig. 4.3C).

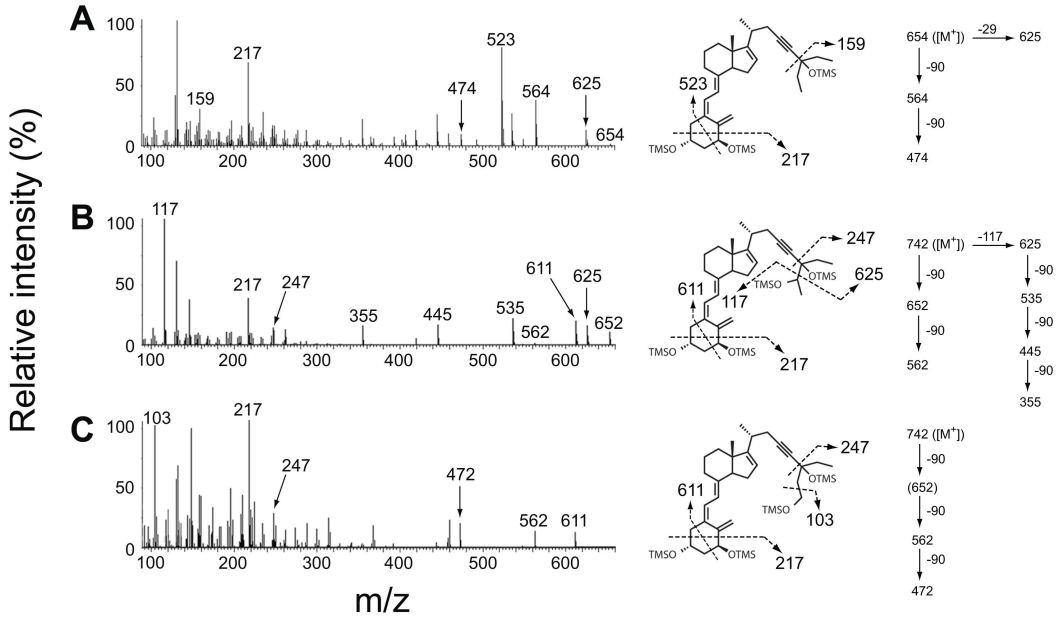

Figure 4.4: GC mass spectra of trimethylsilyl derivatives of **4** (A), g* (B), and h* (C). Experimental conditions are as described in the Methods section.

4.3.3 Structural identification of metabolites of 4 using GC/MS

As in the previous case, we first obtained the mass spectrum of trimethylsilylated **4** for comparison with the spectra of its metabolites g* and h*. The mass spectrum of trimethylsilylated **4** exhibited a molecular ion ($[M]^+$) at m/z 654, the typical fragments associated with sequential eliminations of TMSOH moieties (m/z 564 and m/z 474), the characteristic fragment ions at m/z 523 ($[M–131]^+$) and m/z 217, arising from A–ring cleavage, and a fragment ion at m/z 159, arising from side chain cleavage across C24–C25 bond (Fig. 4.4A).

The mass spectra of trimethylsilylated g* (g^*_{TMS}) and h* (h^*_{TMS}) exhibited fragment ions at m/z 652 and m/z 611 respectively as their highest detectable masses (Fig. 4.4B and 4.4C) but did not exhibit their molecular ions which are beyond the mass range of the instrument. However, the molecular ion peaks of g^*_{TMS} and h^*_{TMS} at m/z 742 could be inferred indirectly from the presence of the key fragment ion at m/z 611 ($[M–131]^+$) observed in the spectra of both compounds. This conclusion is further corroborated by electrospray ionization/mass spectrum (ESI/MS) results of

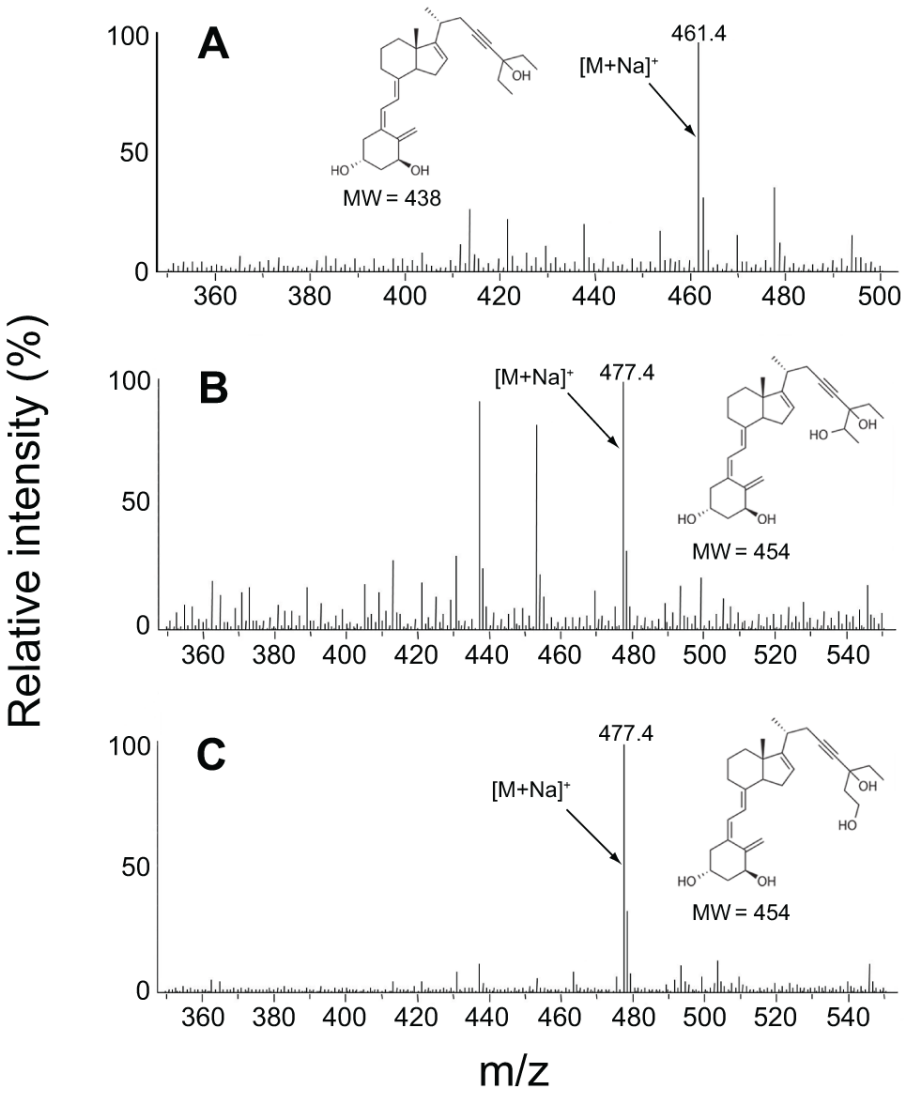

Figure 4.5: ESI mass spectra of **4** (A), g* (B), and h* (C), whose molecular ion masses ($[M]^+$) are m/z 438, 454, and 454, respectively. Prior to analysis, purified **4**, g*, and h* were reconstituted with 0.1% (v/v) formic acid in acetonitrile at final concentrations of 2 μg/mL, 1 μg/mL, and 2 μg/mL, respectively. The sodium adduct ion peak ($[M+Na]^+$) at m/z 477.4 was shown in mass spectra of both g* and h* indicating the addition of a hydroxyl group (16 Da) to the parent compound **4**.

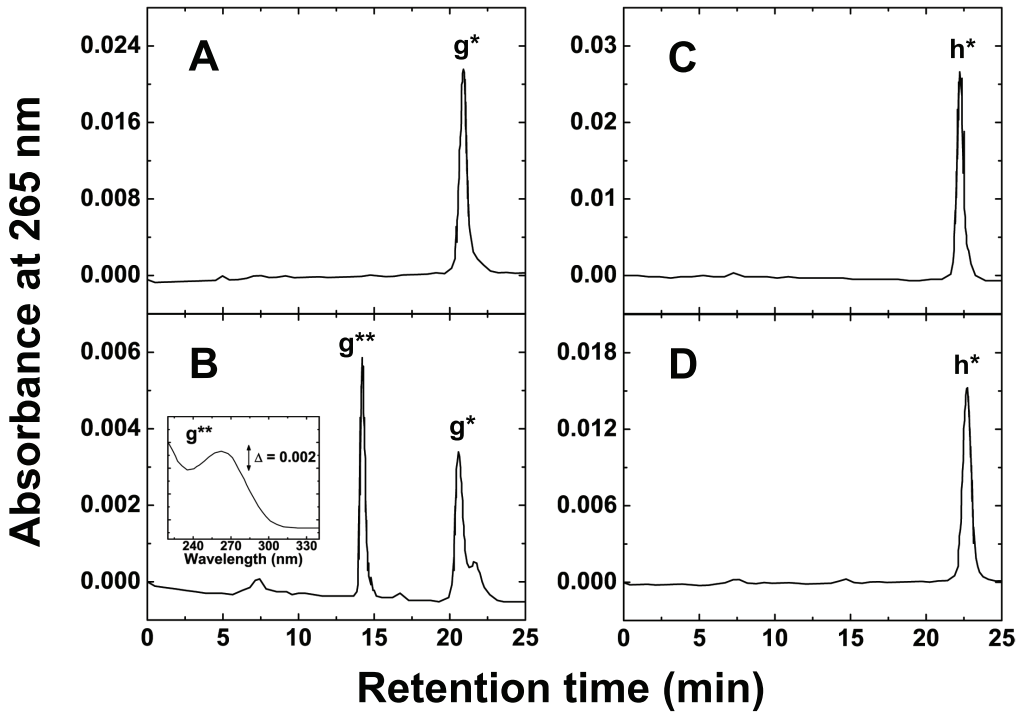

Figure 4.6: HPLC profiles of metabolites g* and h* before (A and C) and after (B and D) periodate oxidation. Periodate–oxdized metabolite g* was further decomposed into a less polar metabolite (g**) indicating that the C–C bond in a vicinal diol (i.e., C25 and C26) is cleaved with the formation of an aldehyde group (B) while metabolite h* remained unaffected (D).

underivatized **4**, g*, and h* which confirm the molecular weight of the metabolites is 16 Da greater than that of the parent compound, **4** (Fig. 4.5). Based on this finding, we concluded that metabolites g* and h* differed from their parent compound by an additional hydroxyl group.

The GC/MS spectra of the metabolites exhibited the characteristic fragment ion at m/z 217, which is an indication that the integrity of their A–ring is maintained and thus ruling out the A–ring as the site of hydroxylation. The mass shift of the characteristic fragment ion at m/z 159 in the spectrum of the parent compound to m/z 247 in the spectra of both metabolites suggests that the site of hydroxylation is either C26 or C26a. Fragment ions at m/z 117 and m/z 624 in the spectrum of g^*_{TMS} suggested C26 as the site of hydroxylation (Fig. 4.4B) while a fragment ion at m/z 103 in the spectrum of h^*_{TMS} suggested C26a as the site of hydroxylation (Fig. 4.4C). To further confirm the hydroxylation sites in g* and h*, both metabolites were subjected to oxidation by sodium periodate. The conversion of g* into a less polar metabolite suggested that g* contained a vicinal diol. On the contrary, h* was found to resist oxidation by sodium periodate (Fig. 4.6). Thus, we identified the metabolites of g* and h* unequivocally as C26-hydroxy-**4** and C26a-hydroxy-**4**, respectively.

4.3.4 Metabolic stability of 2 over 4

To examine the metabolic stability of **2** and **4** in relation to **1**, we incubated each compound in 1 mL of CYP24A1 reconstituted system at 5 μM of concentration. The amounts of the unmetabolized substrate and its metabolites were calculated based on HPLC analysis. The results indicated that 4.2 μM (84%) of **2** and 2.53 μM (50.6%) of **4** remained unmetabolized when compared to only 1.64 μM (32.8%) as in case of **1** (Fig. 4.7). Thus, both compounds **2** and **4** are more stable when compared to **1**. Following this experiment, we examined the kinetics of disappearance of parent compounds **2** and **4** and generation of their respective metabolites during a period of 60 min. The data indicated a much higher metabolic stability for **2** when compared to **4** (Fig. 4.8). The higher rate of metabolism of **4** could be attributed to the

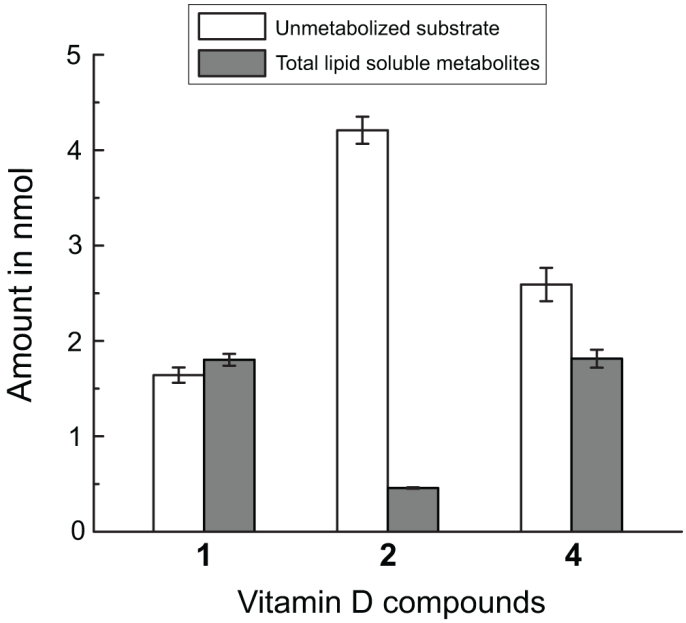

Figure 4.7: The relationship between unmetabolized parent compounds **1**, **2**, and **4** and their respective lipid soluble metabolites produced by CYP24A1. Experimental conditions including HPLC analysis are as described in Fig. 4.2. Metabolites were quantified by integrating the area of the ultraviolet peaks at an absorbance of 265 nm. Error bars represent the mean ± S.D. (n=4).

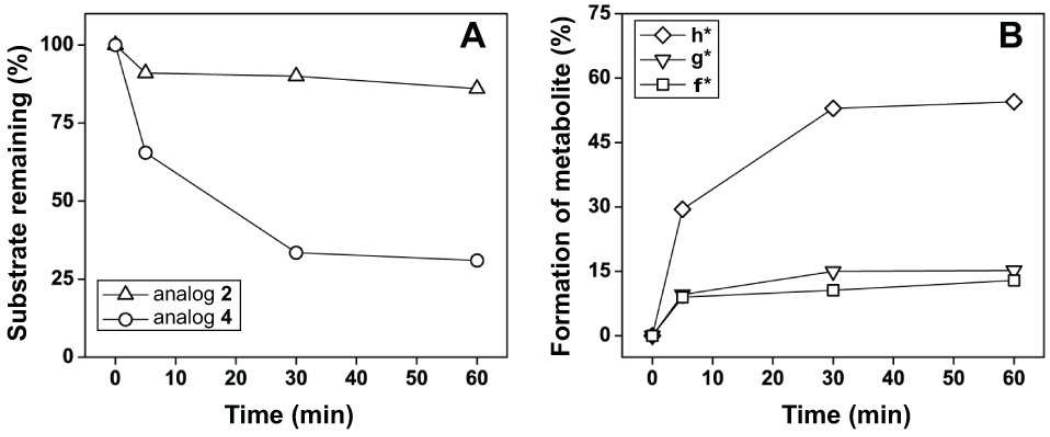

Figure 4.8: Time course of the metabolism of **2** and **4** incubated in a CYP24A1 reconstituted system. Experimental conditions are as described in the Methods section.

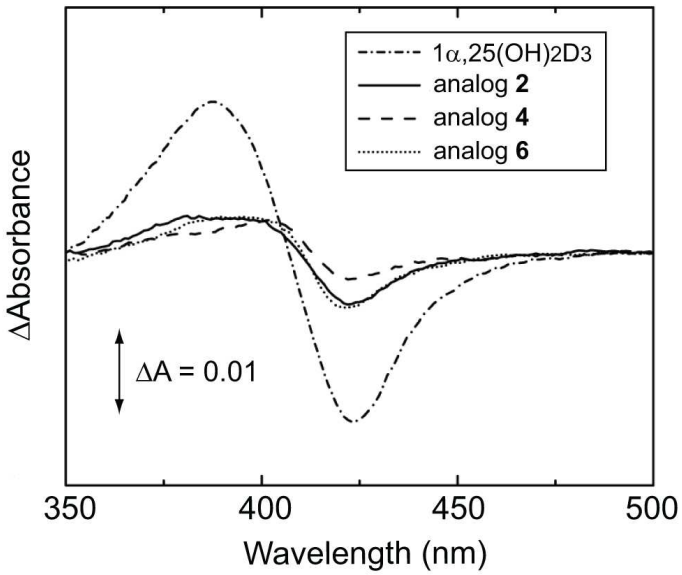

Figure 4.9: Substrate-induced difference spectra of rat CYP24A1 with **1**, **2**, **4**, and **6**. The difference spectra of CYP24A1 were measured in 100 mM potassium phosphate buffer (pH 7.4). The concentrations of enzyme and vitamin D compounds used were 0.5 μM and 1 μM, respectively.

hydroxylation at C26a generating the metabolite h*, whereas the hydroxylation at C26 position of both analogs took place practically at identical rates generating the metabolite f* from **2** and g* from **4** (Fig. 4.8B).

4.3.5 Spectral analysis of CYP24A1 induced by substrate binding

As shown in Fig. 4.9, binding of all tested substrates (**1**, **2**, **4**, and **6**) to CYP24A1 induced the Type I spectra (a peak at 390 nm; a trough at 420 nm), indicating that the spin state of heme iron of CYP24A1 is changed from low spin to high spin. The magnitude of spectral perturbation ($\Delta A_{390-420}$) induced by **1** was larger than that of other substrates. However, it is important to note that the metabolic susceptibility of the compounds to CYP24A1 is not always correlated with the magnitude of the apparent $\Delta A_{390-420}$ as shown in a previous study [136].

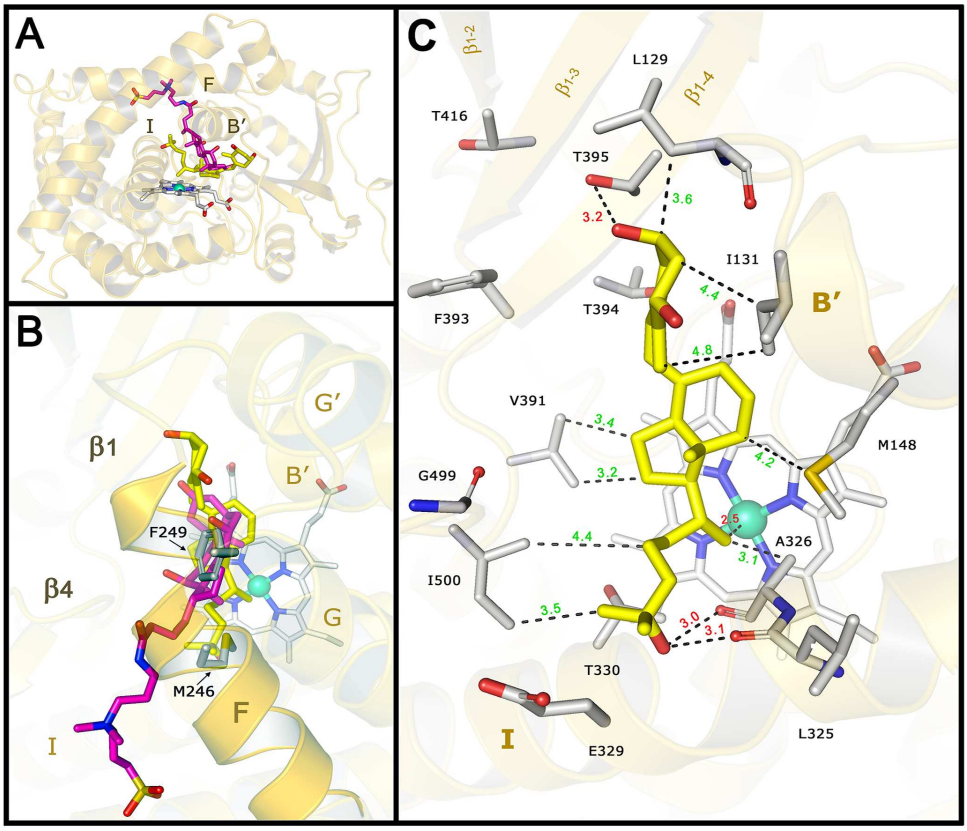

Figure 4.10: A computational model of secosteroid recognition in the open structure of CYP24A1. (A) An Autodock 4.2 docking model for the binding of **1** (in yellow) within the heme-centered active site of CYP24A1 is shown (gold ribbon, PDB ID: 3K9V, copy A). **1** reproducibly docked the enzymes active site formed among helices B, F, G, I, and β1-4 sheet, in a configuration that positions the 25-hydroxylated side chain over the heme via discrete contacts with the kinked, central helix I. **1** binds deeply in the hydrophobic binding pocket of CYP24A1, below the coordinates of a CHAPS detergent molecule (magenta, PDB ID: 3K9V, CPS600) found in the crystal structure. (B) The putative active site of CYP24A1 converges below the hydrophobic pocket formed among helices F, G, and G. In this conformation, important amino acid residues from helix F (M246 and F249) are well positioned to interact with potential substrates and close the active site cavity. (C) The optimized docking model for **1** is shown interacting with key amino acid residues (shown in gray) from the B-B loop (L129 and I131), B-C loop (M148), helix I (L325, A326, E329, and T330), helix K/β1-4 loop (V391), β1-4 sheet (F393, T394, and T395), β1-3 sheet (T416), and β4 turn (G499 and I500); notable hydrogen-bond (Å, red) and hydrophobic-bond distances (Å, green) are given with respect to computed atom positions. The docking of **1** is stabilized in the CYP24A1 active site by multiple hydrophobic contacts, and at least 3 hydrogen bonds (i.e., between the 3β–OH group and β1-4 sheet, and the 25–OH group and helix I).

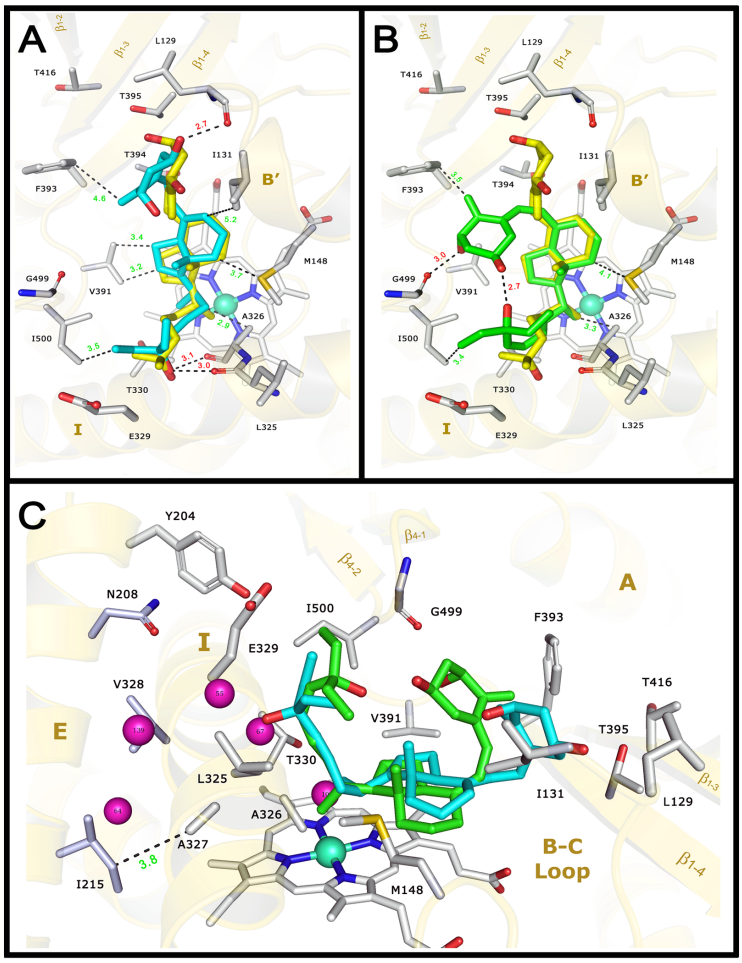

Figure 4.11: A comparison of docking results for **1**, **4**, and **6** in the crystal structure of CYP24A1. Low–energy docking solutions for (A) **4** (shown in aqua) and (B) **6** (shown in green) are superimposed with the docking solution for **1** (shown in yellow). Key amino acid residues flanking the substrate–binding pocket are shown and notable hydrogen (Å, red) and hydrophobic (Å, green) bond distances are given. Analog **6**, which is not metabolized by CYP24A1, docked CYP24A1 with over twice the computed affinity (K_I) of **1**, by forming alternative interactions with the β1-4 sheet (F393) and the β4 turn (G499 and I500), which prevent the side chain from forming typical interactions with helix I. In contrast, **4** docked CYP24A1 with 7 times less computed affinity than **6**, but appears to be a better mimic of **1**, based on its ability to form alternative contacts with helix I (A326) and the β4 turn (I500). (C) **4** and **6** are shown superimposed together in the cylindrical active site of CYP24A1, where **4**, but not **6**, can properly dock its bulky side chain over the heme in a putative recognition site centered on an open span of helix I (residues 325–330). This feature may function to recruit the polar functional groups of substrates, as it is stabilized by a string of water molecules in the crystal structure of CYP24A1 (shown as magenta spheres, from 3K9V, copy A). Multiple conserved residues from helix E (e.g., Y204, N208, and I215) interact with both sides of the kinked span of helix I, as well, helping to form the structural foundation of CYP24A1s extended active site cavity.

4.3.6 Docking analysis

In comparison to **1**, it was tested whether **2**, **4**, and **6** could achieve substrate-like recognition in the binding pocket of rat CYP24A1, using our recently published computational methods [60]. In Fig. 4.10A, an idealized model of **1** (shown in yellow) is depicted in the low-energy docking configuration among α-helices B, F, G, I, and the β1-4 sheet. **1** binds to the active site with its side chain positioned over the heme and engages itself in the catalytic center; situated below the structural coordinates of 3-[(3-Cholamidopropyl)dimethylammonio]-2-hydroxy-1-propanesulfonate (CHAPS), a zwitterionic detergent used to purify recombinant CYP24A1 that binds tightly to the open form of the enzyme (shown in magenta). In Fig. 4.10B, the binding site for **1** located below helix F is shown superimposed with the coordinates of CHAPS in order to illustrate the proximity of the important substrate-binding residues M246 and F249 [136] to the docking solution of the CHAPS binding site. A detailed schematic for the binding configuration of **1**, as seen from below helix F is shown in Fig. 4.10C.

Complimentary docking studies were performed with **2**, **4**, and **6**. We found that all the analogs were capable of docking the CYP24A1 active site in the same general configuration as **1**. Analog **2** docked CYP24A1 with six times less computed affinity than **1** (Table 4.1). However, analog **4** (shown in aqua), which has a bulkier side chain than **2**, docked CYP24A1 normally with only 3−fold lower affinity than **1** (Table 4.1), and it docked more reproducibly than **2** (Fig. 4.11A). The docking model for **6** (shown in green), which docked CYP24A1 with more than twice the computed binding affinity of **1** (Table 4.1), is shown superimposed with the coordinates of **1** in Fig. 4.11B.

Unlike **6**, analogs **2** and **4** consistently bind the CYP24A1 active site in a configuration similar to **1**, with the side chain positioned over the heme. As depicted in Fig. 4.11C, the side chain of **4** interacts with helix I, similar to **1**, within the charged, open cleft that is formed above the heme, among residues L325, A326, A327, V328, E329, and T330. This kinked span of helix I is well hydrated (shown as magenta spheres) in

the crystal structure of CYP24A1 [60] and it exposes the main chain atoms of L325 and A326 to solvent at the same point where the helix I bends into the heme plane near the catalytic residue T330. Conserved amino acid residues (e.g., Y204, N208, and I215) from helix E engage both sides of the disordered span of helix I, forming the underpinning of an elongated binding pocket that extends the CYP24A1 active site over the heme into a narrowing cavity formed among helices E, F, and I (Fig. 4.11C). Compound **6** was the only analog tested that could not dock its side chain into the proximal end of CYP24A1s elongated binding pocket.

Table 4.1: Flexible ligand docking results for **1**, **2**, **4**, and **6** in the crystal structure of rat CYP24A1.

Ligand[†]	Binding Energy[‡] [kcal/mol]	Dissociation Constant (K_I)[⊥] [nM]	Occupancy[§]
1	–12.13	1.29	0.16
2	–11.01	8.49	0.12
4	–11.46	3.98	0.20
6	–12.63	0.55	0.18

[†] Flexible ligand docking simulations for idealized compounds **1**, **2**, **4**, and **6** were performed using Autodock 4.2. Evaluations were based on experiments consisting of 200 Genetic Algorithm (GA) runs, with long evaluations (25,000,000 evals. per GA run), using a search grid targeting the full distal surface of rat CYP24A1 (PDB ID: 3K9V, copy A).

[‡] Binding energy is the computed value for the low-energy docking conformation in the high occupancy solution bin (root mean square=2.0 Å).

[⊥] Dissociation constant or inhibition constant (K_I) is the computed nanomolar affinity for the low-energy, active site binding solution with the highest occupancy.

[§] Occupancy refers to the fraction of total docking solutions represented by the low energy active site docking solution (root mean square=2.0 Å).

4.4 Discussion

The important role of CYP24A1 in catalyzing the initial hydroxylation at C24 in the metabolism of **1** followed by multiple oxidative reactions leading to the formation of calcitroic acid was established more than two decades ago [62, 64, 118, 119]. Recent studies [61, 65, 66, 117, 136] have shown that CYP24A1 is responsible for all C24, C23, and C26 oxidation pathways involved in the metabolism of **1** and is responsible for the production of all the metabolites of **1** shown in Fig. 1.8. Soon after the recognition of CYP24A1 as a multicatalytic enzyme, there were several studies directed towards understanding the critical role of CYP24A1 in the metabolism of a wide range of synthetic analogs [144, 145, 146]. In our present study, we established for the first time the role of CYP24A1 in the metabolism of two vitamin D analogs **2** and **4** with a common 16-ene-23-yne modification. We showed that **2** is metabolized by CYP24A1 into a single metabolite which is identified as C26-hydroxy-**2**. Thus, it became clear that the presence of a triple bond in the side chain of **2** protects it from undergoing hydroxylations at C23 and C24, but **2** is still subjected to hydroxylation at C26. We noted that **4** is metabolized by CYP24A1 into two metabolites that are unequivocally identified as C26-hydroxy-**4** and C26a-hydroxy-**4**. Out of these two metabolites, C26a-hydroxy-**4** is produced in a greater quantity (Fig. 4.2C and 4.8B), suggesting that the addition of methyl groups to distal carbons of the side chain of **2** renders the analog more susceptible to the action of CYP24A1 (Figs. 4.7 and 4.8).

The structural modification of extending the distal carbons of the sterol side chain with methyl groups seen in **4** was introduced for the first time in the synthesis of **5**, which is found to be more potent than **1** in stimulating calcium transport in rachitic rats [147]. This finding of increased biopotency of **5** was assumed to be due to its metabolic stability without direct experimental proof. Since then, this unique structural modification has been incorporated into the synthesis of several analogs. Some of these analogs shown in Fig. 4.1, especially **6** gained importance in drug development. Shankar *et al.* [132] examined the metabolism of **6** in a transformed human keratinocyte cell line (HPK1A-*ras*) and reported that the presence of con-

jugated double bonds at C22–23 and C24–24a in the side chain of **6** prevents both C23 and C24 hydroxylations, but the distal carbons of the sterol side chain of **6** were subjected to hydroxylations producing metabolites identified as C26-hydroxy-**6** and C26a-hydroxy-**6**. It was also noted that these hydroxylations took place in post-mitochondrial fractions isolated from rat, minipig, and human liver [148]. Furthermore, the incubation of **6** with COS-1 cells transfected with an expression vector containing the cDNA that encodes CYP24A1 produced neither C26 nor C26a hydroxylated metabolites [132]. This finding implied that CYP24A1 is not responsible for the C26 and C26a hydroxylation of **6**. However, our data from the CYP24A1 reconstitution assay indicated that the enzyme responsible for the C26 and C26a hydroxylations of **4** is CYP24A1. Thus, even though the metabolic fates of **4** and **6** are seemingly identical, it is most interesting to note that the enzymes responsible for their individual metabolism are different. This finding suggested that the structural features utilized by CYP24A1 to hydroxylate **4** but not **6** are probably related to the distance between the ring structure (i.e., CD–ring) and the distal carbons of the side chain as **6** unlike **4** has a longer side chain. However, Dilworth *et al.* [149] reported that the lengthening of the side chain of **1** has no effect on the activity of CYP24A1 as it is capable of both C23 and C24 hydroxylations of a series of homologated analogs of **1** with their side chains extended up to three additional carbon atoms. Thus, it is interesting to note that the homologation of the side chain as in the case of **6** is not tolerated by CYP24A1 because of the presence of additional modifications in the regions of C23 and C24.

To explore the structural basis by which CYP24A1 discriminates between **1** and analogs **2**, **4**, and **6**, we conducted an *in silico* docking simulation using the crystal structure of CYP24A1 [60]. We found that all analogs bound CYP24A1 with the secosteroid nucleus (i.e., CD–ring) in the same general configuration as **1**. But **6** unlike others was the only analog that could not reproducibly dock in a configuration to position its side chain over the heme even though **6** docked with the highest computed affinity (Table 4.1). Considering the degree of lipophilicity (logP) calculated by ALOGPS 2.1 program [150], such high binding affinity of **6** (logP = 6.59) may be

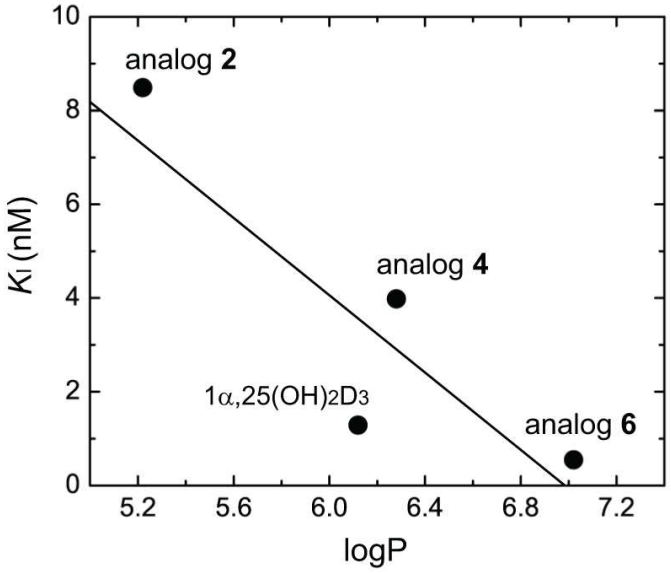

Figure 4.12: Linear dependence between computed dissociation constants (K_I) and theoretical lipophilicity (logP) of vitamin D compounds used in this chapter. LogP values for each compound were calculated by using the ACD/I-LAB software (www.acdlabs.com).

due to having ∼10−fold more lipophilicity than **1** (logP = 5.51) (Fig. 4.12).

Furthermore, we attribute the enhanced binding affinity of **6** to alternative interactions which the A–ring and side chain form with CYP24A1s β1-4 sheet (F393) and β4 turn (G499, I500). Out of the analogs **2** and **4** with the common 16-ene-23-yne modification, **4** docked CYP24A1 with ∼2−fold higher affinity than **2**, and was a better mimic for **1** with respect to the positioning of the C25 hydroxyl group. It appears that the bulkier side chain of **4** helps to compensate for modifications made to the CD–ring and side chain, by allowing the side chain to form alternative interactions with key binding residues from helix I (A326) and the β4 turn (I500). This result helps to explain why CYP24A1 metabolizes **4** more efficiently than **2**, and it also implies that side chain recognition is a key component of CYP24A1s catalytic mechanism. Based on our current understanding of substrate–induced, conformational selection in complex mammalian cytochrome P450s, we speculate that the altered recognition of **6** may impair CYP24A1s ability to acquire a closed form compatible with catalysis [151, 152]. This scenario would also apply to analog **2** to a lesser extent, and it provides an alternative explanation for CYP24A1s discrimination between analogs **4**

and **6**. New crystal structures of CYP24A1 bound to **1** and its related analogs are needed to clarify the structural basis for this discrete selectivity.

While our docking results do not prove why **6** is not metabolized by CYP24A1, they strongly imply that side chain recognition is a critical component of substrate selectivity in CYP24A1. In this regard, we have identified a putative recognition site for the 25–hydroxylated side chain of known substrates, near the amino acid residues A326 and A327 (helix I) in CYP24A1 (Fig. 4.10C). This observation is consistent with existing molecular modeling studies of CYP24A1 [153, 154, 155, 156], which imply that the non-conserved residue A326 partially mediates CYP24A1s species-based regioselectivity, via interactions with the side chain of **1** [153, 154]. The second alanine (A327), unlike a glycine in most mammalian CYPs (including related mitochondrial forms), is well–conserved in CYP24A1. We speculate that this unique alanine pair functions within a putative, side chain recognition site that exists at the base of an elongated cavity that extends the active site of CYP24A1 out over helix I. The size and positioning of this secondary cavity helps to explain the results of Dilworth *et al.* [149], who deduced that the CYP24A1 active site must resemble an open cylinder capable of accommodating analogs of **1** with extended side chains. A network of water molecules line the base of this extended cavity, and imply this section of helix I is highly adapted to recruit hydroxylated side chains of increasing length (Fig. 4.11C). Dehydration of this cavity and/or the heme environment may be required to prevent electron uncoupling during catalysis [26, 157], and our docking analysis hints that side chain recognition may facilitate this pre-catalytic process. These insights correlate well with previous observations that CYP24A1 requires a hydroxyl group at C25 to introduce the C24 vicinal hydroxyl group, a phenomenon best exemplified by its inability to catalyze the 24(R)–hydroxylation of 1α-hydroxyvitamin D_3 [136]. Furthermore, our group previously reported that CYP24A1 can catalyze the C25 hydroxylation of the non–25–hydroxylated synthetic analog, 1α,24(R)-dihydroxyvitamin D_3 [158]. This work implied that a hydroxyl group at C24 can function as a surrogate for the hydroxyl group at C25. Later, Masuda *et al.* [159] reported that CYP24A1 can metabolize another non–25–hydroxylated analog, 1α-hydroxyvitamin D_2. Thus the

methyl group at C24 in 1α-hydroxyvitamin D_2 can also function as a surrogate for the hydroxyl group at C25. Our analysis hints that CYP24A1 is selective for analogs of **1** that are properly functionalized at either the C24 or C25 position of the side chain. We speculate that functional groups at C24 or C25 may help to satisfy a mechanistic requirement for the side chain to provide steric hindrance in the CYP24A1 active site, as needed to dehydrate the heme environment for catalysis.

4.5 Conclusion

In this chapter, we studied the metabolism of two synthetic vitamin D analogs **2** and **4** with a common 16-ene-23-yne modification using rat CYP24A1 in a reconstitution assay. Our finding suggests that the addition of methyl groups at C26/C27 in the side chain of **2** practically made the compound more susceptible to CYP24A1. Similar information with respect to the metabolism of another analog **6** featuring dimethyl groups at its C26/C27 was also provided in a previous study. However, **6** unlike **4** was not metabolized by CYP24A1. These interesting findings provided us an opportunity for the first time to obtain a new insight into the role of CYP24A1 in the metabolism of analogs **4** and **6** by performing an *in silico* docking analysis using the crystal structure of rat CYP24A1. Our results imply that high–affinity binding to CYP24A1 is primarily mediated by hydrophobic contacts with the substrate, but proper recognition, as needed to close the enzyme and initiate the catalytic mechanism, may require discrete interactions between the side chain functionalized either at C24 or C25 and the enzymes highly evolved helix I.

4.6 Acknowledgements

This work was supported by funds from Epimer LLC. I acknowledge financial support from the NSF GK-12 Teaching Fellowship. I also thank Prof. P. Vouros and Ms. R. Gathungu (Northeastern University, Boston, MA) and Dr. A.J. Annalora (The Scripps Research Institute, La Jolla, CA) for their help on GC/MS and ESI/MS

analysis and docking analysis, respectively.

Chapter 5

Metabolism of 1α,25-dihydroxy-3-epi-vitamin D_3, A Natural Metabolite of 1α,25-dihydroxyvitamin D_3, by Rat Cytochrome P450 24A1

5.1 Introduction

The hormonally active form of vitamin D_3, 1α,25-dihydroxyvitamin D_3 (1α,25$(OH)_2D_3$) is the natural ligand for the vitamin D receptor (VDR), a member of the nuclear receptor superfamily [160]. In response to hormone binding, the VDR regulates the transcriptional expression of a wide array of genes, which encode osteocalcin, calbindin, and various other proteins involved in pathophysiological systems [42, 43, 44, 161]. More importantly, 1α,25$(OH)_2D_3$-bound VDR also induces expression of mitochrondrial cytochrome P450 24A1 (CYP24A1), a multicatalytic enzyme that successively oxidizes the side-chain of 1α,25$(OH)_2D_3$, leading to the loss of hormonal activity [61, 64]. The metabolic inactivation of 1α,25$(OH)_2D_3$ primar-

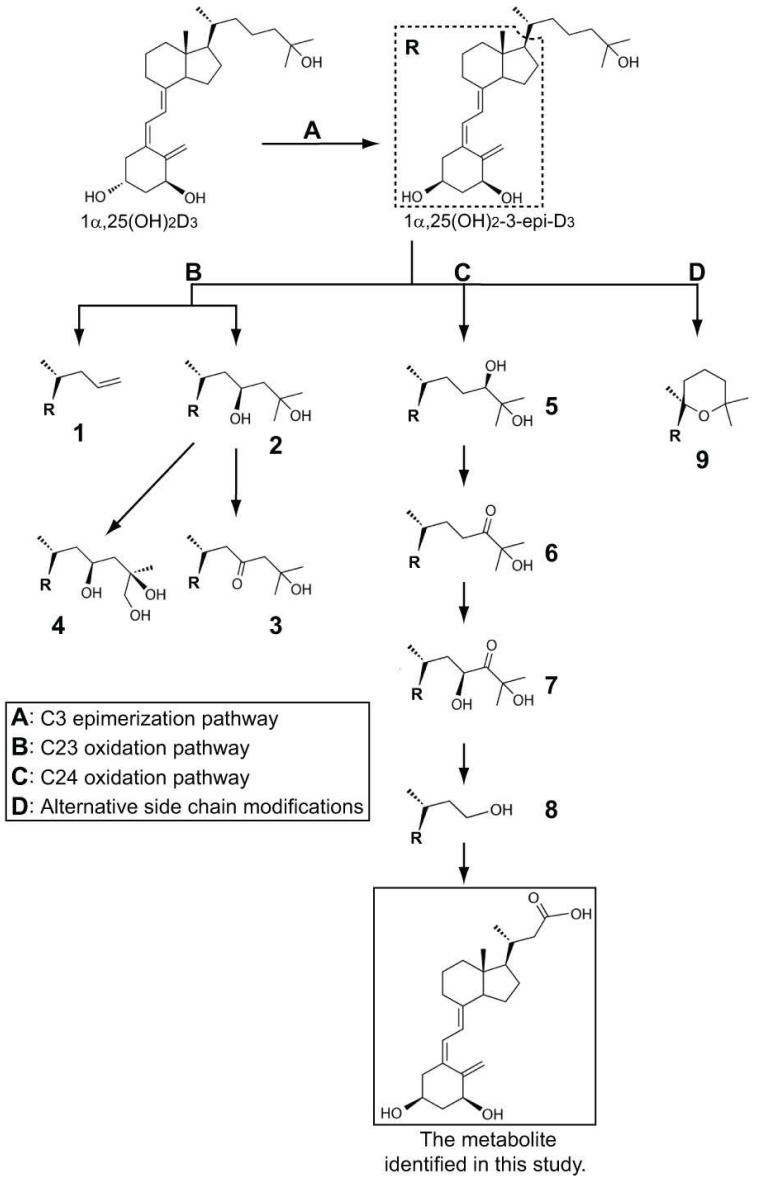

Figure 5.1: Metabolic pathways of $1\alpha,25(OH)_2D_3$ followed by C3 epimerization. Shown is the previously determined structures of $1\alpha,25(OH)_2$-3-epi-D_3 metabolites produced by human CYP24A1 [17], rat CYP24A1 [17], and neonatal human keratinocytes [16]. Metabolites are designated **1** to **9**: **1**, 25,26,27-trinor-23-ene-1α-hydroxyvitamin D_3; **2**, 1α,23,25-trihydroxy-3-epi-vitamin D_3; **3**, 1α,25-dihydroxy-23-oxo-3-epi-vitamin D_3; **4**, 1α,23,26-trihydroxy-3-epi-vitamin D_3; **5**, 1α,24,25-trihydroxy-3-epi-vitamin D_3 ($1\alpha,24,25(OH)_3$-3-epi-D_3); **6**, 1α,25-dihydroxy-24-oxo-3-epi-vitamin D_3 ($1\alpha,25(OH)_2$-24-oxo-3-epi-D_3); **7**, 1α,23,25-trihydroxy-24-oxo-vitamin D_3 ($1\alpha,23,25(OH)_3$-24-oxo-D_3); **8**, 1α,23-dihydroxy-24,25,26,27-tetranor-3-epi-vitamin D_3 ($1\alpha,23(OH)_2$-24,25,26,27-tetranor-3-epi-D_3); **9**, 1α-hydroxy-3-epi-vitamin D_3-20,25-cyclic ether.

ily proceeds through C24 oxidation pathway [62, 119], resulting in the conversion of 1α,25(OH)$_2$D$_3$ into a side-chain cleaved water–soluble metabolite, calcitroic acid [118].

Aside from the aforementioned side-chain oxidation pathway, 1α,25(OH)$_2$D$_3$ is also metabolized through a C3 epimerization pathway [162, 163, 164, 165, 166], leading to the formation of 1α,25-dihydroxy-3-epi-vitamin D$_3$ (1α,25(OH)$_2$-3-epi-D$_3$) in which the orientation of C3 hydroxyl moiety is changed from β to α. 1α,25(OH)$_2$-3-epi-D$_3$, like 1α,25(OH)$_2$D$_3$, is also subjected to further metabolism through putative metabolic pathways [146, 167] as illustrated in Figure 5.1.

The C3 epimerization pathway is tissue-specific as 1α,25(OH)$_2$-3-epi-D$_3$ is produced only in specific tissues [164, 168] as shown in Table 5.1. More interestingly, 1α,25(OH)$_2$-3-epi-D$_3$ exerts significant biological activities in the tissues in which it is produced. As such, 1α,25(OH)$_2$-3-epi-D$_3$ was found to be almost equipotent to 1α,25(OH)$_2$D$_3$ in inhibiting cellular proliferation in human keratinocytes [169, 170], suppressing parathyroid hormone secretion in bovine parathyroid cells [171], and stimulating surfactant synthesis in human alveolar type II cells [172]. In light of prospective clinical applications, the biological activities of 1α,25(OH)$_2$-3-epi-D$_3$ observed in both *in vitro* and *in vivo* studies in conjunction with its low calcemic activity [173, 174] make it a promising therapeutic drug.

To date, the underlying mechanisms for the apparent biological activities of 1α,25(OH)$_2$-3-epi-D$_3$ in relation to the VDR–mediated responses, however, remain obscure because of its poor binding affinity for VDR [169, 171, 176]. Although the metabolic stability of 1α,25(OH)$_2$-3-epi-D$_3$ has been speculated as one of the possible mechanisms [166, 171], the published literature does not yet provide concrete evidence. In this chapter, we have performed a metabolism study comparing of 1α,25(OH)$_2$-3-epi-D$_3$ and its parent compound 1α,25(OH)$_2$D$_3$ using purified rat CYP24A1 in a reconstituted system. The final water–soluble metabolite of 1α,25(OH)$_2$-3-epi-D$_3$ produced by rat CYP24A1 was isolated and unequivocally identified as 3-epi-calcitroic acid. The amount of 3-epi-calcitroic acid produced from 1α,25(OH)$_2$-3-epi-D$_3$ was found to be $\sim$2.6–fold lower than that of calcitroic acid pro-

duced from 1α,25(OH)$_2$D$_3$ under identical conditions. This finding provides the first clear experimental proof that 1α,25(OH)$_2$-3-epi-D$_3$ shows higher metabolic stability over 1α,25(OH)$_2$D$_3$.

Table 5.1: Tissue specific metabolism of 1α,25(OH)$_2$-3-epi-D$_3$ (Adapted and modified from Ref. [175])

Tissues and Cell lines	Species	C3 epimerization pathway
Keratinocytes (primary)	Human	Yes
HaCaT (immortalized keratinocytes)	Human	Yes
Intestinal Cells (Caco-2)-Confluent	Human	Yes
Intestinal Cells (Caco-2)-subconfluent	Human	No
Breast Cancer Cells (SKBR 3)	Human	No
Osteosarcoma Cells (U2-OS)	Human	Yes
Osteosarcoma Cells (Sa-OS)	Human	Yes
Osteosarcoma Cells (UMR-106)	Rat	Yes
Osteosarcoma Cells (ROS 17/2.8)	Rat	Yes
Myeloid Leukemic Cells (HL-60)	Human	No
Myeloid Leukemic Cells (RWLeU-4)	Human	No
Monocytic Leukemic Cells (U 937)	Human	No
Placenta (explants)	Human	No
Vascular Smooth Muscle Cells (primary)	Rat	Yes
Aortic Rings	Rat	Yes
Perfused Kidney	Rat	No
Parathyroid Cells (primary)	Bovine	Yes

5.2 Materials and Methods

5.2.1 Vitamin D Compounds and Chemicals

Crystalline 25-hydroxyvitamin-D_3 ($25(OH)D_3$) and $1\alpha,25(OH)_2D_3$ were purchased from Enzo Life Sciences (Plymouth Meeting, PA). $1\alpha,25(OH)_2$-3-epi-D_3 was synthesized according to a published method [177]. Cholacalcioic acid was synthesized as previously described [178] (For detailed information on synthesis, see Appendix B). All other chemicals were purchased from Sigma-Aldrich (St. Louis, MO) and used without further purification.

5.2.2 Expression and purification of CYP24A1 and its redox cofactors

Recombinant rat CYP24A1 (WT, $\Delta 2-32$) was expressed in *E. coli* (DH5α-FIQ) and purified as described [136]. Purified CYP24A1 samples with A_{417}/A_{280} ratio exceeding 1.0 were considered pure for biochemical assay. Bovine adrenodoxin (ADX) and adrenodoxin reductase (ADR) were expressed and purified as described with minor modifications [137, 138]. Spectral purity indexes of ADX (A_{414}/A_{276}) and ADR (A_{452}/A_{278}) used in the present study were 0.9 and 0.1, respectively [136, 137]. All enzymes were stored at –80 °C prior to use.

5.2.3 CYP24A1 reconstitution assay

The reconstituted CYP24A1 reaction mixture (1 mL) contained 50 mM phosphate buffer (pH 7.4), CYP24A1 (0.5 μM), ADX (0.5 μM), ADR (0.5 μM), and vitamin D substrate (1–5 μM). The reaction was initiated by the addition of NADPH at a final concentration of 1 mM and the mixture incubated at 37 °C for 5–60 min.

5.2.4 Extraction of lipid–soluble and water–soluble metabolites

The reaction was quenched with 2 mL of methanol followed by 4 mL of dichloromethane for lipid extraction using a method as described [62]. The organic layer, containing lipid–soluble metabolites, was evaporated under a stream of nitrogen and the residue redissolved in hexane/isopropanol (85:15, v/v) for HPLC analysis. The aqueous layer from lipid extraction, containing water-soluble metabolites, was acidified with a drop of conc. HCl and re-extracted with dichloromethane. The dichloromethane fraction was dried under a stream of nitrogen and the residue redissolved in hexane/isopropanol/methanol (80:10:10, v/v/v) for HPLC analysis.

5.2.5 High-performance liquid chromatography (HPLC)

HPLC analysis of the lipid extracts from either kidney perfusates or reactants from enzymatic reactions was performed with a Waters System Controller (Waters, Milford, MA). A photodiode array detector (Waters model 996) was used to monitor lipids with the typical vitamin D chromophore (λ_{max} at 265 nm; λ_{min} at 228 nm). Resolution of vitamin D metabolites was achieved using a Zorbax-SIL column (250 mm $\times$ 4.6 mm) (Dupont, Wilmington, DE) eluted with two different solvent mixtures at a flow rate of 2 mL/min: (1) 15% isopropanol in hexane for separation of lipid-soluble metabolites (2) 10% isopropanol and 10% methanol in hexane for water–soluble metabolites.

5.2.6 Gas chromatography-Mass spectrometry (GC-MS)

GC-MS analysis was performed using an Agilent GC system 6890 equipped with a mass-selective detector (MSD5973). Purified metabolites were subjected to trimethylsilyl (TMS) derivatization using Power SIL-Prep (Alltech Associates, Deerfield, IL) in anhydrous acetonitrile (50:50, v/v) at 70 °C for 15 min. The derivatized metabolites (final concentration, 2 μg/mL) were subjected to GC/MS analysis using a HP-5MS GC capillary column (30 m $\times$ 0.25 mm $\times$ 25 m, 5% phenyl siloxane) with helium as a carrier gas at a flow rate of 0.8 mL/min. The oven temperature was set at 150 °C and

ramped at a rate of 10 °C/min to reach the final temperature of 300 °C. Full-scan electron impact spectra across the mass range of m/z 50–700 were acquired in each run and the final spectra were obtained after background correction.

5.2.7 Spectral binding titrations

Binding assays of rat CYP24A1 with 1α,25(OH)$_2$D$_3$ and 1α,25(OH)$_2$-3-epi-D$_3$ were performed using a Cary Model 500 double-beam spectrophotometer as described [136]. Vitamin D substrates were prepared in 4.5% (2-Hydroxypropyl)-β-cyclodextrin and added to a solution of purified CYP24A1 (0.3 μM) in 1.0 mL of 100 mM phosphate buffer (pH 7.4). The stability and concentration of purified enzyme were determined by CO–difference spectra [6] prior to each titration. Substrate–induced spectral shifts from 417 to 392 nm, corresponding to changes from the low– to high–spin state of the heme, were monitored in the presence of increased substrate concentrations. All spectral spin–state titrations were taken to saturation with 10–fold substrate excess. The apparent dissociation constant (K_d) was determined from the Scatchard plot.

5.3 Results

5.3.1 Metabolism studies of 1α,25(OH)$_2$D$_3$ and 1α,25(OH)$_2$-3-epi-D$_3$ using rat CYP24A1 reconstitution system

We examined the catalytic activity of CYP24A1 toward both 1α,25(OH)$_2$D$_3$ and 1α,25(OH)$_2$-3-epi-D$_3$ in a reconstituted system. CYP24A1 was incubated with both substrates at a final concentration of 5 μM for 25 min with optimized concentrations of ADR and ADX. HPLC chromatogram of 1α,25(OH)$_2$D$_3$ incubation showed only two minor lipid–soluble metabolites, identified as 1α,23(OH)$_2$-24,25,26,27-tetranor-D$_3$ (3) and 1α,23,25(OH)$_3$-24-oxo-D$_3$ (4) (Fig. 5.2A). Under the same experimental conditions, it is noted that the amounts of 1α,23(OH)$_2$-24,25,26,27-tetranor-3-epi-D$_3$ (2*) and 1α,24,25(OH)$_3$-3-epi-D$_3$ (4*), the lipid–soluble metabolites of

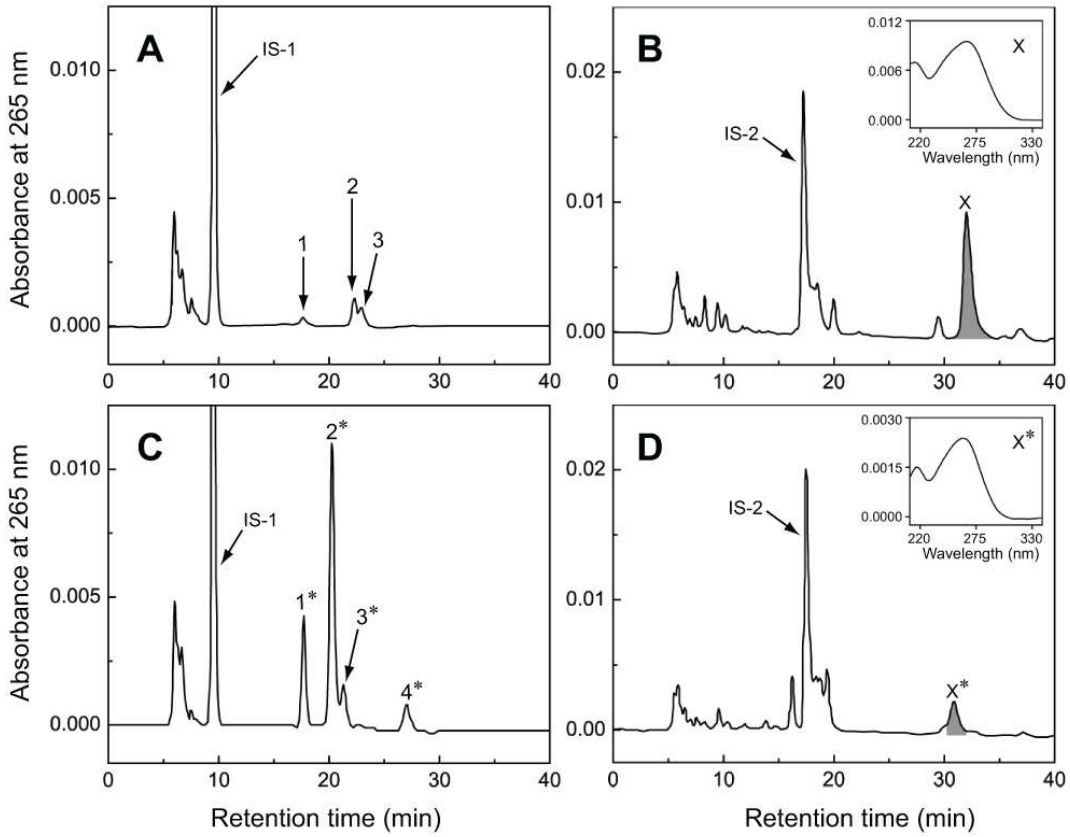

Figure 5.2: HPLC chromatograms of lipid (A and C) and water–soluble (B and D) metabolites of 1α,25(OH)$_2$D$_3$ and 1α,25(OH)$_2$-3-epi-D$_3$, respectively, produced by rat CYP24A1 in a reconstituted system. Experimental conditions are as described under Materials and Methods. Both lipid–soluble and water–soluble metabolites were extracted using the conditions described in Materials and Methods. Prior to extraction, 25(OH)D$_3$ (IS-1) or cholacalcioic acid (IS-2) was added to each sample as internal standard to quantify the efficiency of the extraction step. For lipid–soluble metabolites, peaks were numbered according to the order of appearance: (A) 1, 1α,25(OH)$_2$D$_3$; 2, 1α,23(OH)$_2$-24,25,26,27-tetranor-D$_3$; 3, 1α,23,25(OH)$_3$-24-oxo-D$_3$; (C) 1*, 1α,25(OH)$_2$-3-epi-D$_3$; 2*, 1α,23(OH)$_2$-24,25,26,27-tetranor-3-epi-D$_3$; 3*, 1α,23,25(OH)$_3$-24-oxo-3-epi-D$_3$; 4*, 1α,24,25(OH)$_3$-3-epi-D$_3$. For water-soluble metabolites, peaks X and X* (shaded in gray) were collected and subjected to GC-MS analysis. The UV spectra of peaks X and X* showed the characteristic vitamin D$_3$ chromophore (λ_{max} at 265 nm; λ_{min} at 228 nm) found in insets of (B) and (D), respectively.

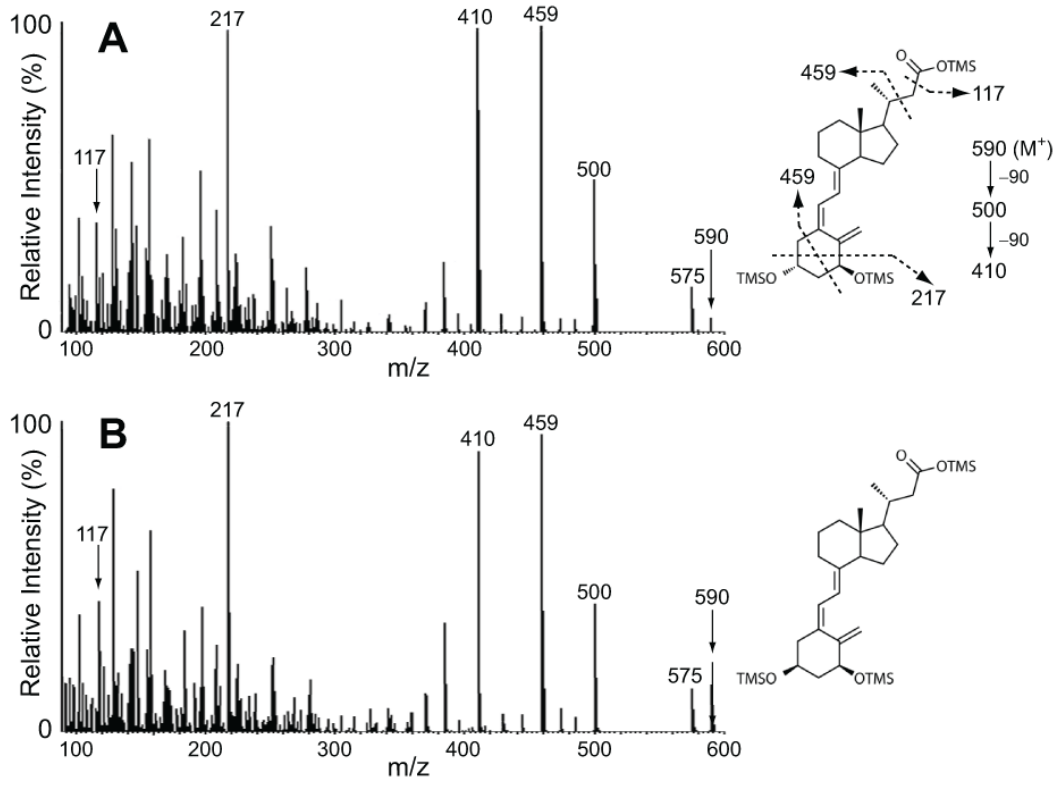

Figure 5.3: Mass spectra of trimethylsilyl derivatives of major water–soluble metabolite of (A) 1α,25(OH)$_2$D$_3$ and (B) 1α,25(OH)$_2$-3-epi-D$_3$ produced by rat CYP24A1 in a reconstituted system. Chromatographic retention times of metabolites X and X* are 22.05 and 22.97 min, respectively.

1α,25(OH)$_2$-3-epi-D$_3$ were significantly higher than the corresponding metabolites of 1α,25(OH)$_2$D$_3$ (Fig. 5.2C). Water–soluble metabolites of 1α,25(OH)$_2$D$_3$ (X) and 1α,25(OH)$_2$-3-epi-D$_3$ (X*) were also purified by HPLC and the corresponding elution profiles are shown in Fig. 5.2B and 5.2D, respectively. The purity of each water–soluble metabolite was determined by the characteristic UV chromophore of vitamin D showing λ_{max} at 265 nm and λ_{min} at 228 nm (insets of Fig. 5.2B and 5.2D). The purified metabolites X and X* were subjected to GC-MS analysis.

5.3.2 Structural identification of water–soluble metabolites X and X* using GC-MS

The trimethylsilylated metabolite X (X_{TMS}) exhibited a molecular ion ([M^+]) at m/z 590 followed by the sequential losses of trimethylsilanol moieties (90 Da) to produce

the fragments at m/z 500 and m/z 410 (Fig. 5.3A). The characteristic fragment ions at m/z 217 and m/z 459 ($[M–131]^+$) were derived from A–ring cleavage. Loss of the TMS–derivatized COOH group accounts for the fragment ion at m/z 117, indicating the presence of a TMS ester function in the side-chain of X. The mass spectral analysis of trimethylsilylated metabolite X* gave a fragmentation pattern virtually identical to that of X_{TMS} (Fig. 5.3B).

5.3.3 Metabolic stability of 1α,25$(OH)_2$-3-epi-D_3 over 1α,25$(OH)_2D_3$

For direct comparison of metabolite levels measured by HPLC, 1α,25$(OH)_2D_3$ and 1α,25$(OH)_2$-3-epi-D_3 were incubated at the same concentration in a rat CYP24A1 reconstituted system as described under Materials and Methods. Relative amounts of unmetabolized substrates and their respective metabolites are shown in Fig. 5.4. The amounts of unmetabolized substrates of 1α,25$(OH)_2D_3$ and 1α,25$(OH)_2$-3-epi-D_3 were not significantly different from each other. However, the total amount of major lipid–soluble metabolites of 1α,25$(OH)_2$-3-epi-D_3 were ∼3–fold higher than that of 1α,25$(OH)_2D_3$. Conversely, the amount of 3-epi-calcitroic acid was ∼2.6–fold lower than that of calcitroic acid. This finding provides definitive evidence that 1α,25$(OH)_2$-3-epi-D_3, a natural metabolite of 1α,25$(OH)_2D_3$, shows higher metabolic stability over its parent substrate although both are readily metabolized through the C24 oxidation pathway.

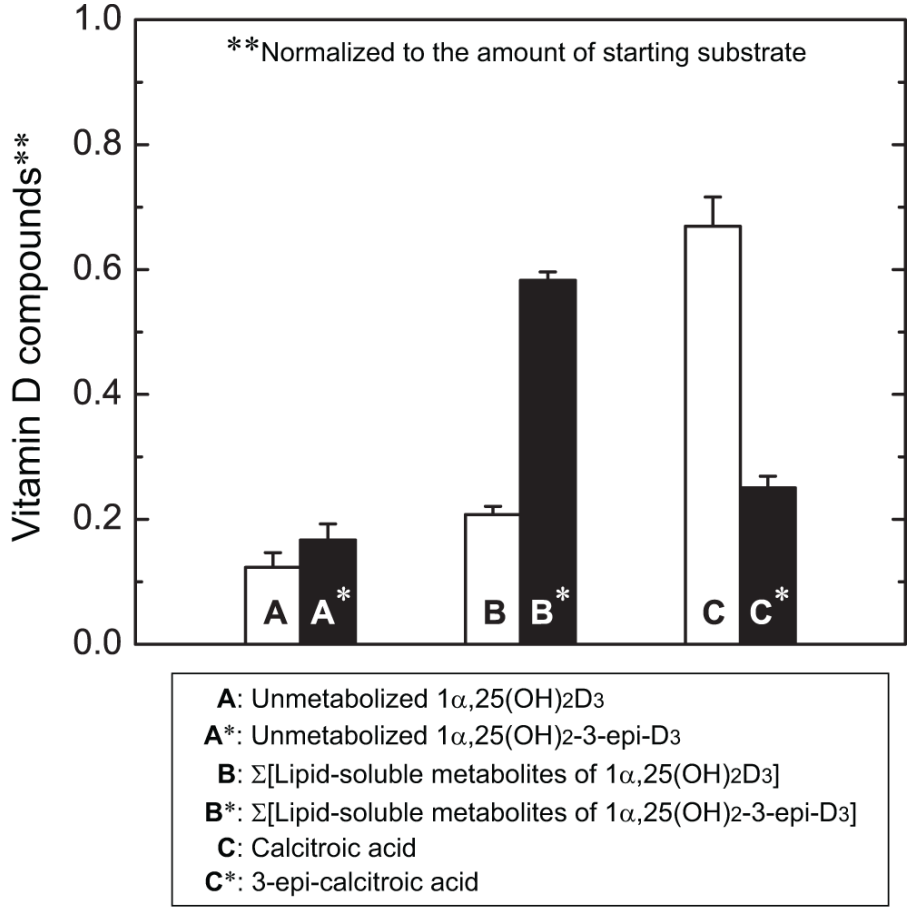

Figure 5.4: Relative amounts of unmetabolized parent substrates and their respective metabolites – both lipid–soluble and water–soluble metabolites – produced in enzyme reconstitution systems containing 5 μM substrate, 0.5 μM ADR, 0.5 μM ADX, 0.5 μM CYP24A1, and 1 mM NADPH. The reaction mixture was incubated at 37 °C for 25 min. Lipid extracts from enzymatic reactions were subjected to HPLC analysis. Metabolites were quantified by integrating the area of the UV peaks at an absorbance of 265 nm. Error bars represent the mean ± S.D. (n=5).

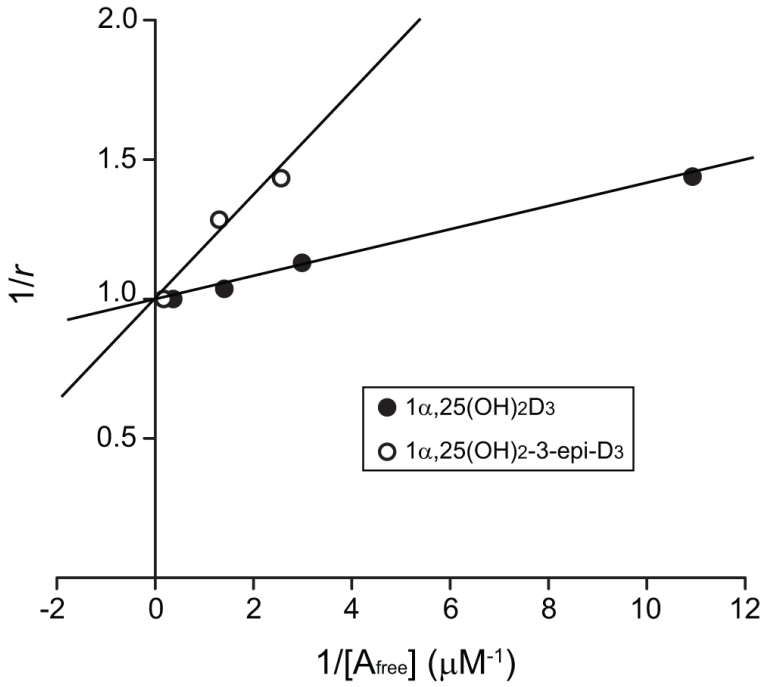

Figure 5.5: Double reciprocal plot of $1/r$ vs. $1/\mathrm{A_{free}}$, where r represents the molar ratio of the total substrate bound to the total amount of enzyme. The free substrate concentration, $[\mathrm{A_{free}}]$ was calculated using the equation $[\mathrm{A_{free}}]=[\mathrm{A_{total}}]-([r][\mathrm{CYP24A1}])$, where $[\mathrm{A_{total}}]$ represents the total substrate concentration at each data point of a given titration curve and [CYP24A1] refers to the total enzyme concentration. The apparent dissociation constant (K_d) was determined from the slope of the line shown in the double reciprocal plot (Table 5.2). Each data point represents the mean of quadruplicate measurements.

Table 5.2: Substrate-binding properties of CYP24A1 for 1α,25(OH)$_2$D$_3$ and 1α,-25(OH)$_2$-3-epi-D$_3$. Data are represented as mean ± S.D. (n=4).

Substrate	Spectral perturbation†	Dissociation Constant (K_d) [μM]
1α,25(OH)$_2$D$_3$	0.032 ± 0.002	0.036 ± 0.004
1α,25(OH)$_2$-3-epi-D$_3$	0.007 ± 0.001	0.144 ± 0.032

† ΔAbs_{max}–ΔAbs_{free}, where ΔAbs_{max} is the maximal change in absorbance between 417 and 392 nm during each titration, and ΔAbs_{free} is the initial difference in absorbance between 417 and 392 nm for the free enzyme prior to each titration. Spectral perturbation reflects the substrate-binding efficiency within the active site of CYP24A1; greater perturbation is correlated to more efficient binding.

5.3.4 Substrate–binding properties of CYP24A1

Binding of 1α,25(OH)$_2$D$_3$ or 1α,25(OH)$_2$-3-epi-D$_3$ to CYP24A1 induced a Type I spectral change (a peak at ∼390 nm; a trough at ∼420 nm), indicating the spin state of heme iron of CYP24A1 is changed from low to high spin. The apparent K_d of 1α,25(OH)$_2$D$_3$ or 1α,25(OH)$_2$-3-epi-D$_3$ was estimated from the slope of titration curves of $1/r$ versus $1/A_{free}$, where r and A_{free} represent the molar ratio of the total substrate bound to the total amount of enzyme and the free substrate concentration, respectively (Fig. 5.5). The preference of CYP24A1 for 1α,25(OH)$_2$D$_3$ over 1α,25(OH)$_2$-3-epi-D$_3$ was evident from the apparent K_d value of 0.036 μM, which is ∼4–fold lower than that of 1α,25(OH)$_2$-3-epi-D$_3$ (Table 5.2).

5.4 Discussion

In endocrine systems, C3 epimerization is known to play a pivotal role in hormone inactivation as seen in conversion of a potent steroid hormone such as 5α-dihydrotestosterone into its inactive steroid 3α-androstanediol [179]. C3 epimeriza-

tion has also been observed in vitamin D endocrine system [162], where the hormonal form 1α,25$(OH)_2D_3$ is converted into its C3 epimer, 1α,25$(OH)_2$-3-epi-D_3. Unlike the role of C3 epimerization as an inactivation process noted in the case of steroid 3α-androstanediol, 1α,25$(OH)_2$-3-epi-D_3 was found to be as potent as 1α,25$(OH)_2D_3$ in various biological activities [169, 170, 171, 172, 180, 181]. This intriguing finding gained further attention in that 1α,25$(OH)_2$-3-epi-D_3 exhibits much lower calcemic activity compared to 1α,25$(OH)_2D_3$ [173, 174]. The lowering of calcemic activity of vitamin D compounds due to C3 epimerization was best demonstrated by 1α-hydroxyvitamin D_3, a potent vitamin D analog whose threshold dose for the development of hypercalcemia was nearly 80–fold higher than its C3 epimer, 1α-hydroxy-3-epi-vitamin D_3 [182].

The change in configuration of C3 hydroxyl group of 1α,25$(OH)_2D_3$ from β to α also results in low binding affinity for VDR [169]. However, some of biological activities of 1α,25$(OH)_2$-3-epi-D_3 appear to be little affected by low binding affinity for VDR [171, 176]. Following these observations, the crystal structure of human VDR complexed with 1α,25$(OH)_2$-3-epi-D_3 [177] revealed that 1α,25$(OH)_2$-3-epi-D_3 lacks interaction with Ser278, which is one of key residues involved in ligand recognition by VDR [183]. However, it is interesting to note that 1α,25$(OH)_2$-3-epi-D_3 maintains the number of hydrogen bonds by an alternative water-mediated interaction to compensate the abolished interaction with Ser278 [177]. Despite these findings, the underlying mechanisms by which the biological activities of 1α,25$(OH)_2$-3-epi-D_3 are exerted still remain elusive. A comparative metabolism study between 1α,25$(OH)_2$-3-epi-D_3 and 1α,25$(OH)_2D_3$ using respective radiolabeled substrates (i.e., 1α,25$(OH)_2$-3-epi-[26,27-^{3}H]D_3 and 1α,25$(OH)_2$[26,27-^{3}H]D_3, respectively) in human keratinocytes [166] offered a possible mechanism that explains some of the unique biological activities produced by 1α,25$(OH)_2$-3-epi-D_3 despite its low binding affinity for VDR. When incubated with physiological concentrations of 1α,25$(OH)_2$-3-epi-[26,27-^{3}H]D_3 and 1α,25$(OH)_2$[26,27-^{3}H]D_3, the radioactivity of 1α,25$(OH)_2$-3-epi-[26,27-^{3}H]D_3 and its lipid–soluble [^{3}H]-metabolites remained detectable for longer period of time than that of 1α,25$(OH)_2$[26,27-^{3}H]D_3 and its lipid–soluble metabolites. This finding suggested

that 1α,25(OH)$_2$-3-epi-D$_3$ is metabolized at a slower rate compared to 1α,25(OH)$_2$D$_3$, thereby being able to exert its biological activities for longer duration. However, the structural identification of metabolites of 1α,25(OH)$_2$-3-epi-D$_3$ produced in keratinocytes was not determined although it was speculated that the metabolites of 1α,25(OH)$_2$-3-epi-D$_3$ were similar to those of 1α,25(OH)$_2$D$_3$.

To address the aforementioned issues, we investigated the comparative metabolism of 1α,25(OH)$_2$-3-epi-D$_3$ and 1α,25(OH)$_2$D$_3$ using rat CYP24A1 in a reconstituted system. The intermediary metabolites of 1α,25(OH)$_2$-3-epi-D$_3$ produced by CYP24A1 were identified as 1α,23(OH)$_2$-24,25,26,27-tetranor-3-epi-D$_3$ (2*), 1α,23,25(OH)$_3$-24-oxo-3-epi-D$_3$ (3*), 1α,24,25(OH)$_3$-3-epi-D$_3$ (4*) based on co-migration with known standards. Furthermore, we also isolated and identified for the first time the final water–soluble metabolite of 1α,25(OH)$_2$-3-epi-D$_3$, namely 3-epi-calcitroic acid (Figs. 5.1 and 5.3). When incubated with pharmacological concentrations of 1α,25(OH)$_2$D$_3$ and 1α,25(OH)$_2$-3-epi-D$_3$, the amount of 3-epi-calcitroic acid produced by CYP24A1 was $\sim$2.6–fold lower than that of calcitroic acid under identical conditions (Fig. 5.4). This finding provided definitive proof to indicate that 1α,25(OH)$_2$-3-epi-D$_3$ shows higher metabolic stability over 1α,25(OH)$_2$D$_3$. In addition, the apparent K_{d} value for 1α,25(OH)$_2$-3-epi-D$_3$ was $\sim$4–fold higher than that for 1α,25(OH)$_2$D$_3$ (Table 5.2), rendering the formation of enzyme–substrate complexes for 1α,25(OH)$_2$-3-epi-D$_3$ less favorable. This finding is in good agreement with results from a previous study in which kinetic analysis of the initial C24-hydroxylation generated by rat CYP24A1 toward both 1α,25(OH)$_2$-3-epi-D$_3$ and 1α,25(OH)$_2$D$_3$, with apparent K_{m} values of 0.15 and 0.06 μM, respectively [146].

5.5 Conclusion

In this chapter, we compared rat CYP24A1-mediated metabolism of 1α,25(OH)$_2$-3-epi-D$_3$ with that of 1α,25(OH)$_2$D$_3$ in a reconstituted system and showed that both substrates are metabolized through the same C24 oxidation pathway (Fig. 5.6). For the first time, we identified 3-epi-calcitroic acid as the final

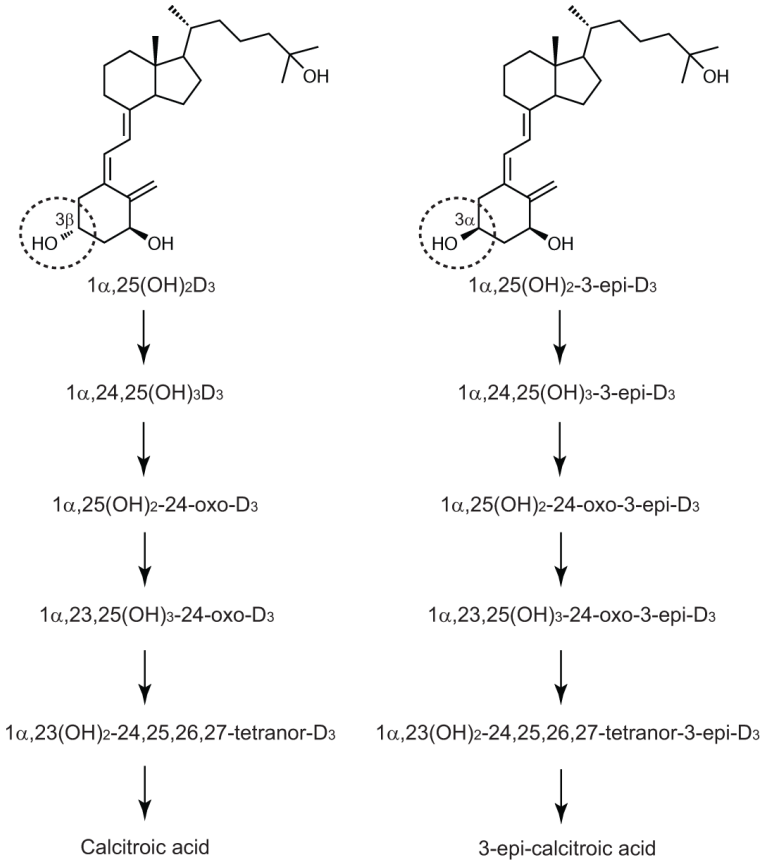

Figure 5.6: The complete C24 oxidation pathway for metabolism of 1α,$25(OH)_2D_3$ and 1α,$25(OH)_2$-3-epi-$D_3$by rat CYP24A1.

metabolite of 1α,25(OH)$_2$-3-epi-D$_3$. Furthermore, we showed that the amount of calcitroic acid produced from 1α,25(OH)$_2$D$_3$ was greater than that of 3-epi-calcitroic acid produced from 1α,25(OH)$_2$-3-epi-D$_3$ under the same experimental conditions. Thus, we proved that the slower inactivation of 1α,25(OH)$_2$-3-epi-D$_3$ by CYP24A1 could be responsible, at least in part, for the prolonged and potent biological effects of 1α,25(OH)$_2$-3-epi-D$_3$ observed in certain types of cells (e.g., parathyroid cells and keratinocytes) in spite of its lower affinity to VDR.

5.6 Acknowledgements

I thank Prof. P. Vouros and Ms. R. Gathungu (Northeastern University, Boston, MA) for their help on GC/MS analysis.

Chapter 6

Concluding Remarks and Future Work

Cytochrome P450s (CYPs) are heme-thiolate mooxygenases that play important roles in the synthesis of endogenous compounds such as steroids as well as the metabolism of xenobiotics. In this thesis, two mitochondrial CYPs, namely CYP27B1 and CYP24A1, were employed to exploit their native catalytic activities for potential applications in vitamin D biosensing and metabolism of vitamin D drugs. Ultimately, the main goal of work in Chapters 2 and 3 was to achieve the substrate hydroxylation by CYP27B1 via electrode–driven catalysis.

In Chapter 2, electrochemical methods were used to provide CYP27B1 with reducing equivalents for electrode-driven catalysis. Surfactant films on an edge-plane pyrolytic graphite electrode were employed to achieve electronic coupling between CYP27B1 and the electrode. Cyclic voltammetry in a deoxygenated solution revealed excellent electrochemical reversibility with an average midpoint potential of –180 ± 5 mV vs. Ag/AgCl and the rate constant for heterogeneous electron transfer 3.5 ± 0.6 s^{-1}. Despite the excellent electron transfer between CYP27B1 and the electrode, the lack of electrode–driven catalysis to support substrate hydroxylation was observed. Given that, biochemical and spectroscopic analysis of CYP27B1 in surfactant films were further performed in Chapter 3. It was found that the structural integrity of CYP27B1 in surfactant films can be significantly perturbed, thereby impairing the

catalytic activity of the enzyme. In addition, the potentials required to achieve efficient electron transfer from the electrode to the enzymes active sites lies within the range of dioxygen reduction. As a result, the electrode–driven reduction of CYPs for substrate oxidation can be a futile process that leads to the reduction of dioxygen which generates reactive oxygen species (e.g., hydrogen peroxide) and, further impairs the enzymes stability. Thus, one possible solution would be to design practical electrode materials exhibiting very high overpotential (i.e., more negative potential) for dioxygen reduction. Future work will further pursue the use of engineered electrode materials to overcome the aforementioned issue associated with reduction of dioxygen.

Owing to the lack of enzyme stability, direct immobilization will not be an ideal strategy to achieve the electrode–driven catalysis. Therefore, if CYPs are not immobilized but in solution, the use of a redox mediator that is thermodynamically favorable enough to provide CYPs with reducing equivalents, but not sensitive enough to react with dioxygen would be another possible alternative.

It is also generally believed that bacterial CYPs, which possess higher turnover and stability (e.g., performing catalytic functions under extreme conditions of temperature, pH, or solvent) than their mammalian counterparts, are the most suitable enzymes for practical purposes. Indeed, bacterial CYP105A1 and its mutants, which have been tailored for stereoselective synthesis of 1α,25$(OH)_2D_3$, were recently discovered by Hayashi *et al.* [Structure-based Design of a Highly Active Vitamin D Hydroxylase from *Streptomyces griseolus* CYP105A1, *Biochemistry* 47 (2008) 11964]. Thus, one future experiment would be based on exploiting the catalytic activity of CYP105A1 or its mutants for vitamin D biosensing applications.

In Chapter 4, the comprehensive metabolism of two synthetic analogs of 1α,25$(OH)_2D_3$, namely 1α,25-dihydroxy-16-ene-23-yne-vitamin D_3 (**2**) and 1α,25-dihydroxy-16-ene-23-yne-26,27-dimethyl-vitamin D_3 (**4**) was examined using rat CYP24A1 in a reconstituted system. We noted that **2** is metabolized into a minor metabolite identified as C26-hydroxy-**2**, confirming that the 16ene-23-yne modification is well-suited for resisting the activity of CYP24A1. However, **4** is rapidly

metabolized into two metabolites, identified as C26-hydroxy-**4** and C26a-hydroxy-**4**. This finding clearly indicates that the addition of methyl groups to distal carbons of the side chain of **2** renders the analog more susceptible to the action of CYP24A1. To gain a better insight into the structural determinants for substrate recognition of different analogs, we performed for the first time an *in silico* docking analysis using the crystal structure of rat CYP24A1 that had been solved for the substrate–free open form. Another well-known synthetic analog **6**, which is known to be inactive to the activity of CYP24A1, was accompanied by **2** and **4** for docking analysis. The results hint that CYP24A1 metabolizes selectively different analogs of 1α,25$(OH)_2D_3$, based on their ability to generate discrete recognition cues (e.g., side chain recognition) required to close the enzyme and trigger the catalytic mechanism. New crystal structures of CYP24A1 complexed with 1α,25$(OH)_2D_3$ and its related analogs are expected to clarify the structural basis for the discrete selectivity discussed in this thesis.

In Chapter 5, the metabolism of 1α,25$(OH)_2$-3-epi-D_3, a natural metabolite of 1α,25$(OH)_2D_3$, was examined using rat CYP24A1 in a reconstituted system. The stereochemistry of the 3-OH group of 1α,25$(OH)_2D_3$ contributed substantially to binding affinity to CYP24A1, showing that the value of K_d for 1α,25$(OH)_2$-3-epi-D_3 was ∼4–fold higher than that of 1α,25$(OH)_2D_3$. In addition, the amount of metabolic end product of 1α,25$(OH)_2$-3-epi-D_3, a newly discovered metabolite identified as 3-epi-calcitroic acid, was found to be ∼2.6–fold lower than that of 1α,25$(OH)_2D_3$ (i.e., calcitroic acid), providing definitive evidence for the higher metabolic stability of 1α,25$(OH)_2$-3-epi-D_3 when compared to 1α,25$(OH)_2D_3$. This finding, together with the intrinsic minimal calcemic activity of 1α,25$(OH)_2$-3-epi-D_3 (or its related analogs), provides a forecast for making the use of it as a promising anti-cancer drug. Moreover, the prevalence of 1α,25$(OH)_2$-3-epi-D_3 and its precursor 3-epi-hydroxyvitamin D_3 in serum of infants and adults have been recently ascertained from clinical studies [Full-scan Mass Spectral Evidence for 3-epi-25-hydroxyvitamin D_3 in Serum of Infants and Adults, *Clinical Chemistry and Laboratory Medicine* 49 (2011) 253]. Taken together, the work presented in this thesis provides invaluable insight for both the scientific

and medical communities.

Appendix A

Protocol: Expression and Purification of Mouse CYP27B1

A.1 General Procedure

1. Transform pKCHis-m1α(encoding mouse CYP27B1 with tetra His-tag at the C-terminus) and pGro12 (encoding molecular chaperonin GroEL/ES) to competent *E. coli* (DH5α) cells.

2. Pick a single colony from a freshly streaked selective agar plate and inoculate a starter culter of 5 mL TB with 50 μg/mL Ampicillin and 25 μg/mL Kanamycin.

3. Incubate for 10$\sim$12 h at 37°C with shaking (250 rpm).

4. Diulte the cells (1 mL) into 100 mL TB (pH 7.0) containing 50 μg/mL Ampicillin and 25 μg/mL Kanamycin) in 1 L flask.

5. Grow the cells until OD_{660}=0.5$\sim$0.8, which takes normally 4 h with 225 rpm at 37°C.

6. Add δ-Aminolevulinic acid (ALA)*, isopropyl β-D-1-thiogalactopyranoside (IPTG), and arabinose (Ara) at a final concentration of 1 mM, 1 mM, and 4 mg/mL, respectively. *ALA is an endogenous precursor of porphyrin; IPTG is

an inducer of CYP27B1 expression; Ara is an inducer of chaperonin GroEL/ES expression (see Fig. A.1).

7. The cells are grown in the incubator for 20∼24 h with 200 rpm at 26°C.

8. Pellet the cells with 4000 rpm for 10 min and decant the supernatant.

9. Resuspend the cells with Buffer A** (30 mL) including 0.2 mM phenylmethylsulfonyl fluoride (PMSF)***, a serine protease inhibitor. Buffer A**: 100 mM KPi, 0.5 M NaCl, 20% glycerol, 1% CHAPS, pH 7.4. ***PMSF is dissolved in isopropanol.

10. The tube containing the resuspended cells is placed in the shaker for 30 min to homogenize the cells at 4°C.

11. During step 7, rinse the NTA-resin (4 mL of well-mixed resin solution), which is soaked in EtOH, with deionized water by centrifuging 5 times with 3400 rpm at 4°C for 2 min. Decant the supernatant and resuspend with deionized water each time. Equilibrate the resin with 2 mL of buffer A****. Buffer A****: 100 mM KPi, 0.5 M NaCl, 20% glycerol, 0.1% CHAPS, pH 7.4.

12. Sonicate the homogenized cells for 15 min at 4°C.

13. The lysed cells are subjected to ultracentrifuge the cell at 4°C with 100000g for 1 h.

14. Mix the resultant supernatant with the resin from step 8 for 1 h.

15. During step 11, equilibrate a PD-10 column with 25 mL of Buffer A****.

16. Pack the column with the resultant mixture obtained from step 11.

17. Wash the column with 10 CV (20 mL) Buffer A**** + 50 mM imidazole.

18. Wash the column with 10 CV Buffer A**** + 60 mM imidazole.

19. Wash the column with 10 CV Buffer A**** + 70 mM imidazole.

20. Wash the column with 10 CV Buffer A**** + 80 mM imidazole.

21. Wash the column with 10 CV Buffer A**** + 90 mM imidazole.

22. Wash the column with 10 CV Buffer A**** + 100 mM imidazole.

23. Collect the fraction of the purified protein with 5 CV Buffer A**** + 200 mM imidazole. Note that the flow rate is reduced to 0.5 mL/min for elution. SDS-PAGE analysis of purified CYP27B1 is shown in Fig. A.3.

24. Concentrate the protein fraction with Amicon tube (15 mL) until obtaining the final volume of 2.5 mL. Centrifuge with 5000 g at 4°C for 30 min and check the volume remained in the filter side.

25. Add the concentrated protein (2.5 mL) to the PD–10 column and elute with 3.5 mL Buffer A****.

26. Take 50 μL of purified protein and mix it with 750 μL of buffer A**** to measure the absolute spectrum.

27. Prepare 1M of sodium dithionite in Buffer A**** and add 10 μL into 800 μL of purified protein solution. Apply CO bubble for 1 min and measure CO–difference spectra of reduced CYP27B1 using difference extinction coefficient at 446 and 490 nm of 90 $mM_{-1}cm_{-1}$.

28. Transfer the purified protein into 15 mL Amicon tube to further increase its concentration if necessary.

A.2 Supplementary Figures

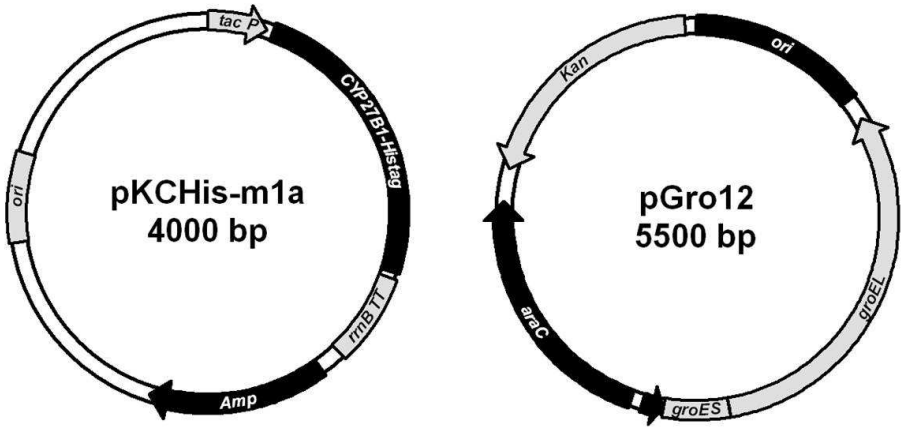

Figure A.1: Expression constructs for Mouse CYP27B1 (pKCHis-m1α) and molecular chaperonin GroEl/ES (pGro12).

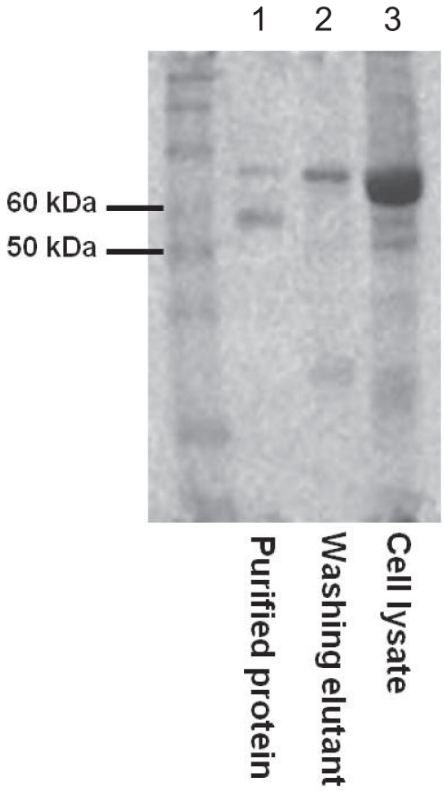

Figure A.2: SDS-PAGE analysis of cell lysate (lane 3), washing elutant obtained at step 14 (lane 2), and column effluent washed with 200 mM imidazole (lane 1). Step imidazole (step 15-19) elutions are used to improve the purity of CYP27B1 (see Fig. A.3).

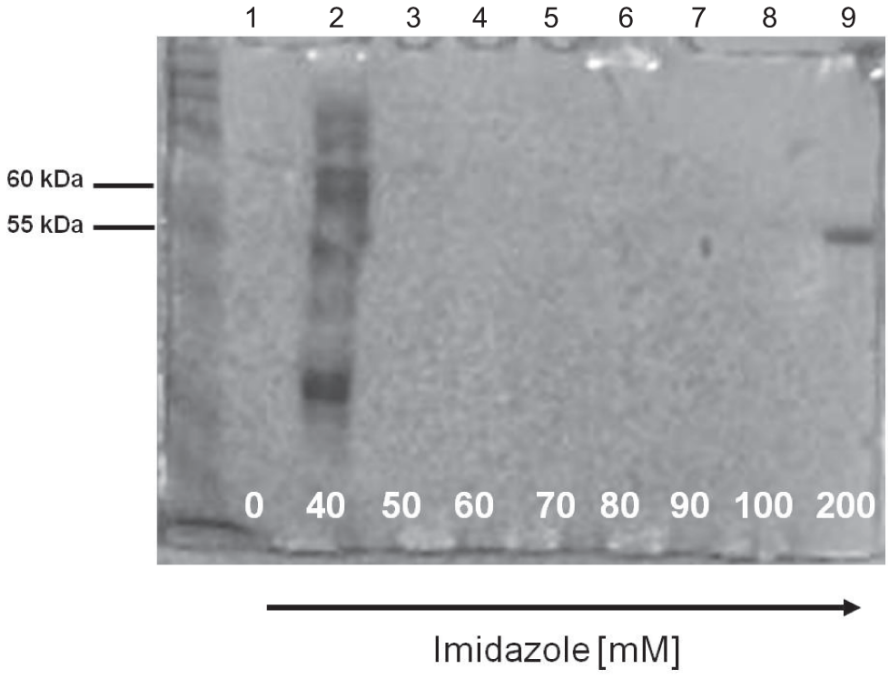

Figure A.3: SDS-PAGE analysis of column effluent obtained from step imidazole (40 to 200 mM) elutions. Lane 9 shows a single band at 51 kDa, the molecular weight of the purified CYP27B1.

Appendix B

Synthesis of Cholacalcioic Acid

B.1 Background

To quantify extraction efficiency, an internal standard is added in a constant amount to samples prior to extraction. The following describes the general steps in the synthesis of cholacalcioic acid (Fig. B.1), which was used in Chapter 5 as an internal standard when extracting the water–soluble metabolites.

B.2 General procedure

First, a total of 100 μg of 24(R),25-dihydroxyvitamin D_3 dissolved in 50 μL of methanol and was subjected to periodate oxidation by reacting it with 50 μL of 5%

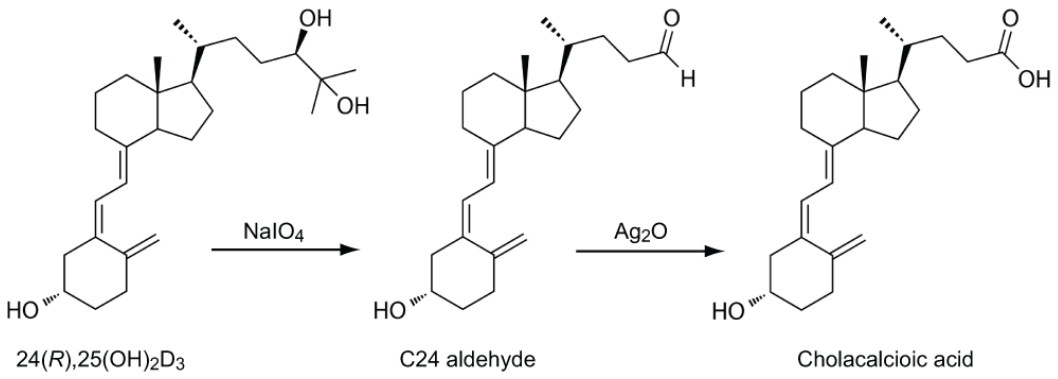

Figure B.1: Chemical synthesis of cholacalcioic acid.

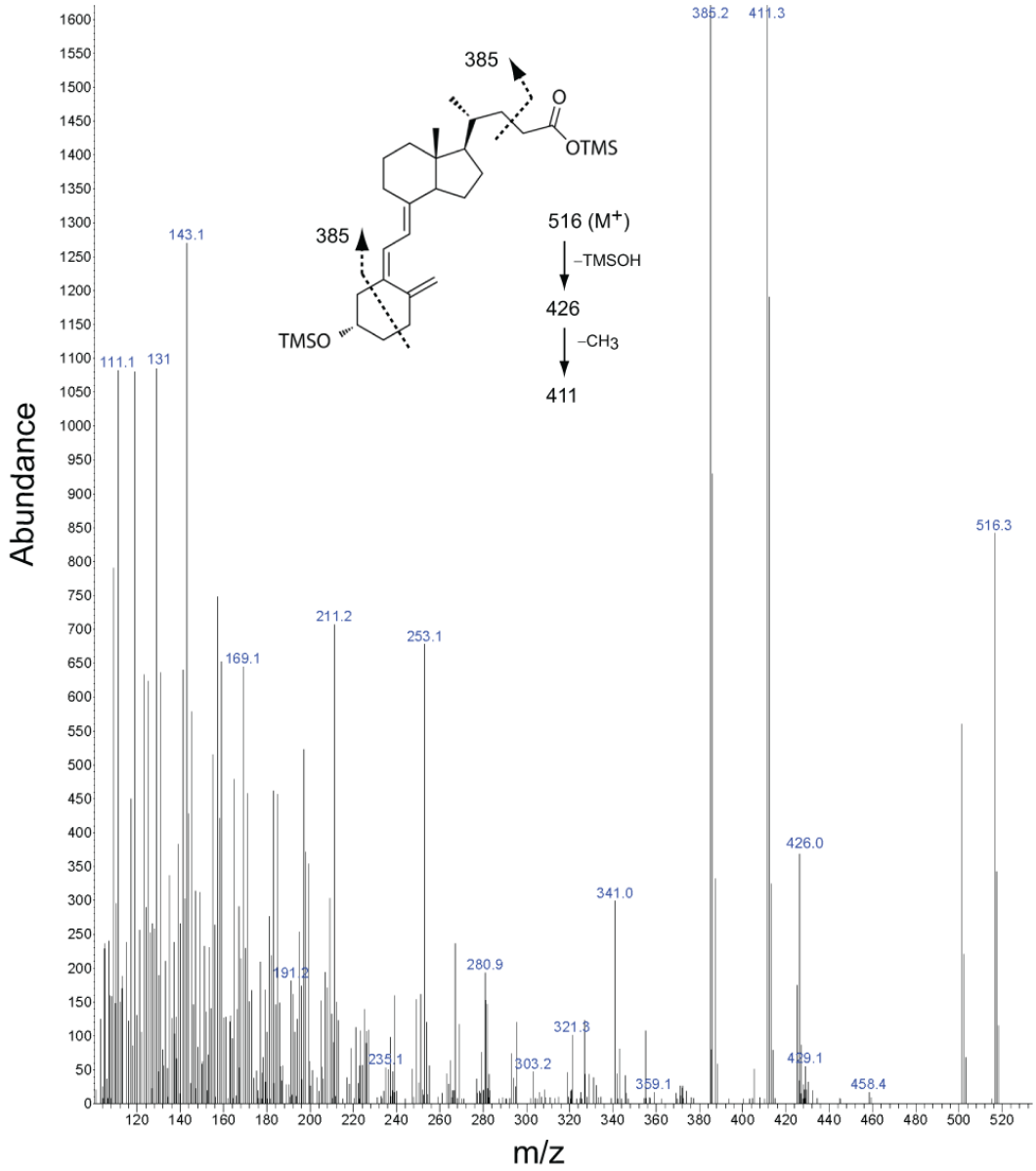

Figure B.2: Mass spectra of trimethylsilyl derivative of cholacalcioic acid synthesized by the method described above.

(w/v) aqueous sodium metaperiodate ($NaIO_4$). After 30 min at 25°C, the reaction product (i.e., C24 aldehyde) was dried under nitrogen gas, and subjected to HPLC using a Zobax-SIL column eluted with 15% isopropanol in hexane at a flow rate of 2 mL/min. Silver oxide was prepared *in situ* from 0.1 M silver nitrate ($AgNO_3$) and 0.1 M NaOH. A total of 20 μg of purified C24 aldehyde was dissolved in 200 μL of methanol and was subjected to further oxidation with 200 μL of silver oxide for 15 min at 25°C. Subsequently, 2 mL of methanol and water (1:1, v/v) was added to the reaction mixture and centrifuged. The supernatant was added to 1 mL of methanol and dried it under nitrogen gas. The resultant sample was subjected to HPLC analysis as described above except for using hexane/isopropanol/methanol (8:1:1, v/v/v) solvent system. The mass spectrum of trimethylsilyl (TMS) derivative of purified cholacalcioic acid exhibited a molecular ion ($[M^+]$) at m/z 516 followed by the sequential loss of a trimethylsilanol moiety (90 Da) and a methyl (15 Da) group to produce the fragments at m/z 426 and m/z 411, respectively (Fig. B.2). The characteristic fragment ions at m/z 131 and m/z 385 ($[M–131]^+$) were derived from A–ring cleavage.

Bibliography

[1] O. Hayashi, M. Katagiri, and S. Rothberg. Mechanism of the pyrocatechase reaction. *J. Am. Chem. Soc.*, 77:5450, 1955.

[2] H. S. Mason, W. L. Fowlks, and E. Peterson. Oxygen transfer and electron transport by the phenolase complex. *J. Am. Chem. Soc.*, 77:2914, 1955.

[3] D. Garfinkel. Studies on pig liver microsomes. I. Enzymic and pigment composition of different microsomal fractions. *Arch. Biochem. Biophys.*, 77:493, 1958.

[4] M. Klingenberg. Pigments of rat liver microsomes. *Arch. Biochem. Biophys.*, 75:376, 1958.

[5] T. Omura and R. Sato. The carbon monoxide-binding pigment of liver microsomes: I. Evidence for its hemoprotein nature. *J. Biol. Chem.*, 239:2370, 1964.

[6] T. Omura and R. Sato. The carbon monoxide-binding pigment of liver microsomes: II. Solubilization, purification, and properties. *J. Biol. Chem.*, 239:2379, 1964.

[7] P. R. Ortiz de Montellano. *Cytochrome P450: Structure, Mechanism, and Biochemistry.* Plenum Press, 1986.

[8] M. Sono, M. P. Roach, E. D. Coulter, and J. H. Dawson. Heme-containing oxygenases. *Chem. Rev.*, 96:2842, 1996.

[9] I. G. Denisov, T. M. Makris, S. G. Sligar, and I. Schlichting. Structure and chemistry of cytochrome P450. *Chem. Rev.*, 105:2253, 2005.

[10] S. M. Contakes, Y. H. L. Nguyen, H. B. Gray, E. C. Glazer, A. M. Hays, and D. B. Goodin. *Conjugates of heme–thiolate enzymes with photoactive metal–diimine wires.* Springer, 2007.

[11] J. R. Winkler, P. Wittung-Stafshede, J. Leckner, B. G. Malmstrom, and H. B. Gray. Effects of folding on metalloprotein active sites. *Proc. Natl. Acad. Sci. USA*, 94:4246, 1997.

[12] J. L. R. Anderson and S. K. Chapman. Ligand probes for heme proteins. *Dalton Trans.*, 1:13, 2005.

[13] R. Feyereisen. Insect P450 enzymes. *Annu. Rev. Entomol.*, 44:507, 1999.

[14] D. W. Nebert, M. Adesnik, M. J. Coon, R. W. Estabrook, F. J. Gonzales, P. F. Guengerich, I. C. Gunsalus, E. F. Johnson, B. Kemper, W. Levin, I. R. Phillips, R. Sato, and M. R. Waterman. The P450 gene superfamily - Recommended nomenclature. *DNA*, 6:1, 1987.

[15] G. A. Roberts, G. Grogan, A. Greter, S. L. Flitsch, and N. J. Turner. Identification of a new class of cytochrome p450 from a *Rhodococcus* sp. *J. Bacteriol.*, 184:3898, 2002.

[16] J. Hedegaard and I. C. Gunsalus. Mixed function oxidation. IV. An induced methylene hydroxylase in camphor oxidation. *J. Biol. Chem.*, 240:4038, 1965.

[17] C. A. Tyson, J. D. Lipscomb, and I. C. Gunsalus. Roles of puridaredoxin and $P450_{cam}$ in methylene hydroxylation. *J. Biol. Chem.*, 247:5777, 1972.

[18] T. L. Poulos, M. Perez, and G. C. Wagner. Preliminary crystallographic data on cytochrome $P450_{cam}$. *J. Biol. Chem.*, 257:10427, 1982.

[19] I. Schlichting, J. Berendzen, K. Chu, A. M. Stock, S. A. Maves, D. E. Benson, R. M. Sweet, D. Ringe, G. A. Petsko, and S. G. Sligar. The catalytic pathway of cytochrome P450$_{cam}$ at atomic resolution. *Science*, 287:1615, 2000.

[20] N. Urushino, K. Yamamoto, N. Kagawa, S. Ikushiro, M. Kamakura, S. Yamada, S. Kato, K. Inouye, and T. Sakaki. Interaction between mitochondrial CYP27B1 and adrenodoxin: Role of arginine 458 of mouse CYP27B1. *Biochemistry*, 45:4405, 2006.

[21] I. C. Gunsalus, J. R. Meeks, and J. D. Lipscomb. Cytochrome P450$_{cam}$ substrate and effector interactions. *Ann. NY Acad. Sci.*, 212:107, 1973.

[22] S. A. Martinis, S. R. Blanke, L. P. Hager, S. G. Sligar, and G. H. B. Hoa. Probing the heme iron coordination structure of pressure-induced cytochrome P450$_{cam}$. *Biochemistry*, 35:14530, 1996.

[23] G. S. Wilson, J. C. M. Tsibris, and I. C. Gunsalus. Electrochemical studies of puridaredoxin and its selenium analog. *J. Biol. Chem.*, 248:6059, 1973.

[24] L. D. Gorsky, D. R. Kopp, and M. J. Coon. On the stoichiometry of the oxidase and mooxygenase reactions catalyzed by liver microsomal cyrochrome P450 - Products of oxygen reduction. *J. Biol. Chem.*, 259:6812, 1984.

[25] W. M. Atkins and S. G. Sligar. Metabolic switching in cytochrome P450$_{cam}$ - Deuterium isotope effects on regiospecificity and the monooxygenase oxidase ratio. *J. Am. Chem. Soc.*, 109:3754, 1987.

[26] P. J. Loida and S. G. Sligar. Molecular recognition in cytochrome P450 - Mechanism for the control of uncoupling reactions. *Biochemistry*, 32:11530, 1993.

[27] F. P. Guengerich. Reactions and significance of cytochrome P450 enzymes. *J. Biol. Chem.*, 266:10019, 1991.

[28] F. P. Guengerich. Roles of cytochrome P450 enzymes in chemical carcinogenesis and cancer chemotherapy. *Cancer Res.*, 48:2946, 1988.

[29] K. Ruckpaul and H. Rein. *Biochemistry and Physiology of Plant Cytochrome P-450, in Microbial and Plant Cytochrome P-450: Biochemical Characteristics, Genetic Engineering and Practical Implications.* Taylor & Francis, 1991.

[30] R. Sheldon. Enzyme - Picking a winner. *Nature*, 399:636, 1999.

[31] O. Kappeli, M. Sauer, and A. Fiechter. Convenient procedure for the isolation of highly enriched, cyrochrome P450 containing microsomal fraction from Candida tropicalis. *Anal. Biochem.*, 126:179, 1982.

[32] D. R. Nelson, T. Kamataki, D. J. Waxman, F. P. Guengerich, R. W. Estabrook, R. Feyereisen, F. J. Gonzalez, M. J. Coon, I. C. Gunsalus, O. Gotoh, K. Okuda, and D. W. Nebert. The P450 superfamily - Update on new sequences, gene-mapping, accession numbers, early trivial names of enzymes, and nomenclature. *DNA Cell Biol.*, 12:1, 1993.

[33] Y. Higashi, T. Hiromasa, A. Tanae, T. Miki, J. Nakura, T. Kondo, T. Ohura, E. Ogawa, K. Nakayama, and Y. Fujii-Kuriyama. Effects of individual mutations in the P450C21 pseudogene on the P450C21 activity and their distribution in the patient genomes of congenital steroid 21-hydroxylase deficiency. *J. Biochem.*, 109:638, 1991.

[34] B. W. Hollis. 25-Hydroxyvitamin D_3-1α-hydroxylase in porcine hepatic tissue - Subcellular localization to both mitochondria and microsomes. *Proc. Natl. Acad. Sci. USA*, 87:6009, 1990.

[35] M. A. Shampo and R. A. Kyle. Edward C Kendall - Nobel laureate. *Mayo Clin. Proc.*, 76:119, 2001.

[36] M. F. Holick. Vitamin D and Health: Evolution, biological functions, and recommended dietary intakes for vitamin D. *Clinic Rev. Bone Miner. Metab.*, 7:2, 2009.

[37] P. Mattila, A.-M. Lampi, R. Ronkainen, J. Toivo, and V. Piironen. Sterol and vitamin D_2 contents in some wild and cultivated mushrooms. *Food Chem.*, 76:293, 2002.

[38] R. Nicolaysen. Studies upon the mode of action of vitamin D. *Biochem. J.*, 31:122, 1937.

[39] A. W. Norman, J. F. Myrtle, R. J. Midgett, H. G. Nowicki, V. Williams, and G. Popjak. 1,25-dihydroxycholecalciferol - Identification of proposed active form of vitamin D_3 in intestine. *Science*, 173:51, 1971.

[40] D. E. M. Lawson, D. R. Fraser, E. Kodicek, H. R. Morris, and D. H. Williams. Identification of 1,25-dihydroxycholecalciferol, a new kidney hormone controlling calcium metabolism. *Nature*, 230:228, 1971.

[41] M. F. Holick, H. K. Schnoes, and H. F. DeLuca. Identification of 1,25-dihydroxycholecalciferol, a form of vitamin D_3 metabolically active in intestine. *Proc. Natl. Acad. Sci. USA*, 68:803, 1971.

[42] R. Bouillon, W. H. Okamura, and A. W. Norman. Structure-function relationships in the vitamin D endocrine system. *Endocr. Rev.*, 16:200, 1995.

[43] L. A. Plum and H. F. DeLuca. Vitamin D, disease and therapeutic opportunities. *Nat. Rev. Drug Discov.*, 9:941, 2010.

[44] I. Schuster. Cytochromes P450 are essential players in the vitamin D signaling system. *Biochim. Biophys. Acta*, 1814:186, 2011.

[45] E. Usui, M. Noshiro, Y. Ohyama, and K. Okuda. Unique property of liver mitochondrial P450 to catalyze the two physiologically important reactions involved in both cholesterol catabolism and vitamin D activation. *FEBS Lett.*, 274:175, 1990.

[46] R. Shinkyo, T. Sakaki, M. Kamakura, M. Ohta, and K. Inouye. Metabolism of vitamin D by human microsomal CYP2R1. *Biochem. Biophys. Res. Comm.*, 324:451, 2004.

[47] I. Aiba, T. Yamasaki, T. Shinki, S. Izumia, K. Yamamoto, S. Yamada, H. Terato, H. Ide, and Y. Ohyama. Characterization of rat and human CYP2J enzymes as vitamin D 25-hydroxylases. *Steroids*, 71:849, 2006.

[48] R. P. Gupta, B. W. Hollis, S. B. Patel, K. S. Patrick, and N. H. Bell. CYP3A4 is a human microsomal vitamin D 25-hydroxylase. *J. Bone Miner. Res.*, 19:680, 2004.

[49] N. Strushkevich, S. A. Usanov, A. N. Plotnikov, G. Jones, and H.-W. Park. Structural analysis of CYP2R1 in complex with vitamin D_3. *J. Mol. Biol.*, 380:95, 2008.

[50] J. B. Cheng, D. L. Motola, D. J. Mangelsdorf, and D. W. Russell. Deorphanization of cytochrome P450 2R1 - A microsomal vitamin D 25-hydroxylase. *J. Biol. Chem.*, 278:38084, 2003.

[51] J. B. Cheng, M. A. Levine, N. H. Bell, D. J. Mangelsdorf, and D. W. Russell. Genetic evidence that the human CYP2R1 enzyme is a key vitamin D 25-hydroxylase. *Proc. Natl. Acad. Sci. USA*, 101:7711, 2004.

[52] M. G. Brunette, M. Chan, C. Ferriere, and K. K. Roberts. Site of 1,25$(OH)_2$ vitamin D_3 synthesis in kidney. *Nature*, 276:287, 1978.

[53] K. Takeyama, S. Kitanaka, T. Sato, M. Kobori, J. Yanagisawa, and S. Kato. 25-hydroxyvitamin D_3 1α-hydroxylase and vitamin D synthesis. *Science*, 277:1827, 1997.

[54] J. G. Ghazarian, C. R. Jefcoate, J. C. Knutson, W. H. Orme-Johnson, and H. F. DeLuca. Mitochondrial cytochrome P450 - Component of chick kidney 25-hydroxycholecalciferol-1α-hydroxylase. *J. Biol. Chem.*, 249:3026, 1974.

[55] T. Sakaki, N. Sawada, K. Takeyama, S. Kato, and K. Inouye. Enzymatic properties of mouse 25-hydroxyvitamin D_3 1α-hydroxylase expressed in *Escherichia coli*. *Eur. J. Biochem.*, 259:731, 1999.

[56] T. Sakaki, N. Kagawa, K. Yamamoto, and K. Inouye. Metabolism of vitamin D_3 by cytochrome P450. *Front. Biosci.*, 10:119, 2005.

[57] S. Masuda, V. Byford, A. Arabian, Y. Sakai, M. B. Demay, R. St-Arnaud, and G. Jones. Altered pharmacokinetics of 1α,25-dihydroxyvitamin D_3 and 25-hydroxyvitamin D_3 in the blood and tissues of the 25-hydroxyvitamin D-24-hydroxylase (CYP24a1) null mouse. *Endocrinol.*, 146:825, 2005.

[58] R. St-Arnaud, A. Arabian, R. Travers, F. Barletta, P. M. Raval, K. Chapin, J. Depovere, C. Mathieu, S. Christakos, M. B. Demay, and F. H. Glorieux. Deficient mineralization of intramembranous bone in vitamin D-24-hydroxylase-ablated mice is due to elevated 1,25-dihydroxyvitamin D and not to the absence of 24,25-dihydroxyvitamin D. *Endocrinol.*, 141:2658, 2000.

[59] H. C. Horvath, P. Lakatos, J. P. Kosa, K. bacsi, K. Borka, G. Bises, T. Nittke, P. A. Hershberger, G. Speer, and E. Kallay. The candidate oncogene CYP24A1: A potential biomarker for colorectal tumorigenesis. *J. Histochem. Cytochem.*, 58:277, 2010.

[60] A. J. Annalora, D. B. Goodin, W.-X. Hong, Q. Zhang, E. F. Johnson, and C. D. Stout. Crystal structure of CYP24A1, a mitochondrial cytochrome P450 involved in vitamin D metabolism. *J. Mol. Biol.*, 396:441, 2010.

[61] M. Akiyoshi-Shibata, T. Sakaki, Y. Ohyama, M. Noshiro, K. Okuda, and Y. Yabusaki. Further oxidation of hydroxycalcidiol by calcidiol 24-hydroxylase - A study with the mature enzyme expressed in *Escherichia coli*. *Eur. J. Biochem.*, 224:335, 1994.

[62] G. S. Reddy and K.-Y. Tserng. Calcitroic acid, end product of renal metabolism of 1,25-dihydroxyvitamin D_3 through C-24 oxidation pathway. *Biochemistry*, 28:1763, 1989.

[63] G. W. Engstrom, T. A. Reinhardt, and R. L. Horst. 25-hydroxyvitamin D_3-23-hydroxylase, a renal enzyme in several animal species. *Arch. Biochem. Biophys.*, 250:86, 1986.

[64] T. Sakaki, N. Sawada, Y. Nonaka, Y. Ohyama, and K. Inouye. Metabolic studies using recombinant *Escherichia coli* cells producing rat mitochondrial CYP24: CYP24 can convert 1 α,25-dihydroxyvitamin D_3 to calcitroic acid. *Eur. J. Biochem.*, 262:43, 1999.

[65] M. J. Beckman, P. Tadikonda, E. Werner, J. Prahl, S. Yamada, and H. F. DeLuca. Human 25-hydroxyvitamin D_3-24-hydroxylase, a multicatalytic enzyme. *Biochemistry*, 35:8465, 1996.

[66] T. Sakaki, N. Sawada, K. Komai, S. Shiozawa, S. Yamada, K. Yamamoto, Y. Ohyama, and K. Inouye. Dual metabolic pathway of 25-hydroxyvitamin D_3 catalyzed by human CYP24. *Eur. J. Biochem.*, 267:6158, 2000.

[67] J. Kazlauskaite, A. C. G. Westlake, L.-L. Wong, and H. A. O. Hill. Direct electrochemistry of cytochrome $P450_{cam}$. *Chem. Commun.*, 18:2189, 1996.

[68] B. D. Fleming, Y. Tian, S. G. Bell, L.-L. Wong, V. Urlacher, and H. A. O. Hill. Redox properties of cytochrome $P450_{BM3}$ measured by direct methods. *Eur. J. Biochem.*, 270:4082, 2003.

[69] K. F. Aguey-Zinsou, P. V. Bernhardt, J. J. De Voss, and K. E. Slessor. Electrochemistry of $P450_{cin}$: new insights into P450 electron transfer. *Chem. Commun.*, 3:418, 2003.

[70] A. Fantuzzi, M. Fairhead, and G. Gilardi. Direct electrochemistry of immobilized human cytochrome P450 2E1. *J. Am. Chem. Soc.*, 126:5040, 2004.

[71] E. I. Iwuoha, S. Joseph, Z. Zhang, M. R. Smyth, U. Fuhr, and P. R. Ortiz de Montellano. Drug metabolism biosensor: electrochemical reactivities of cytochrome $P450_{cam}$ immobilised in synthetic vesicular systems. *J. Pharm. Biomed. Anal.*, 17:1101, 1998.

[72] Z. Zhang, A. E. F. Nassar, Z. Q. Lu, J. B. Schenkman, and J. F. Rusling. Direct electron injection from electrodes to cytochrome $P450_{cam}$ in biomembrane-like films. *J. Chem. Soc. Faraday Trans.*, 93:1769, 1997.

[73] V. V. Shumyantseva, Y. D. Ivanov, N. Bistolas, F. W. Scheller, A. I. Archakov, and U. Wollenberger. Direct electron transfer of cytochrome P450 2B4 at electrodes modified with nonionic detergent and colloidal clay nanoparticles. *Anal. Chem.*, 76:6046, 2004.

[74] D. L. Johnson, A. J. Conley, and L. L. Martin. Direct electrochemistry of human, bovine, and porcine cytochrome P450c17. *J. Mol. Endocrinol.*, 36:5188, 2006.

[75] M. Gelo-Pujic, H. H. Kim, N. G. Butlin, and G. T. R. Palmore. Electrochemical studies of a truncated laccase produced in *Pichia pastoris*. *Appl. Environ. Microbiol.*, 65:5515, 1999.

[76] J. F. Fei, H. K. Song, and G. T. R. Palmore. A biopolymer composite that catalyzes the reduction of oxygen to water. *Chem. Mater.*, 19:1565, 2007.

[77] I. Hamachi, S. Noda, and T. Kunitake. Functional conversion of myoglobin bound to synthetic bilayer-membranes - From dioxygen storage protein to redox enzyme. *J. Am. Chem. Soc.*, 113:9625, 1991.

[78] J. F. Rusling and A. E. F. Nassar. Enhanced eletron-transfer for myoglobin in surfactant films on electrodes. *J. Am. Chem. Soc.*, 115:11891, 1993.

[79] D. R. Fraser and E. Kodicek. Unique biosynthesis by kidney of a biologically active vitamin D metabolite. *Nature*, 228:764, 1970.

[80] E. Uchida, N. Kagawa, T. Sakaki, N. Urushino, N. Sawada, M. Kamakura, M. Ohta, S. Kato, and K. Inouye. Purification and characterization of mouse CYP27B1 overproduced by an *Escherichia coli* system coexpressing molecular chaperonins GroEL/ES. *Biochem. Biophys. Res. Commun.*, 323:505, 2004.

[81] J. F. Rusling and H. Zhang. Multilayer films of cationic surfactants on electrodes - Control of charge transport by phase. *Langmuir*, 7:1791, 1991.

[82] S. Joseph, J. F. Rusling, Y. M. Lvov, T. Friedberg, and U. Fuhr. An amperometric biosensor with human CYP3A4 as a novel drug screening tool. *Biochem. Pharmacol.*, 65:1817, 2003.

[83] E. Laviron. General expression of the linear potential sweep voltammogram in the case of diffusionless electrochemical systems. *J. Electroanal. Chem.*, 101:19, 1979.

[84] A. K. Udit, M. G. Hill, and H. B. Gray. Electrochemistry of cytochrome P450 BM3 in sodium dodecyl sulfate films. *Langmuir*, 22:10854, 2006.

[85] M. T. Fisher and S. G. Sligar. Control of heme protein redox potential and reduction rate: Linear free energy relation between potential and ferric spin state equilibrium. *J. Am. Chem. Soc.*, 107:5018, 1985.

[86] S. N. Daff, S. K. Chapman, K. L. Turner, R. A. Holt, S. Govindaraj, T. L. poulos, and A. W. Munro. Redox control of the catalytic cycle of flavocytochrome $P450_{BM3}$. *Biochemistry*, 36:13816, 1997.

[87] M. Born. Volumen und Hydratationswärme der Ionen. *Z. Phys.*, 1:45, 1920.

[88] R. J. Kassner. Effects of nonpolar environments on redox potentials of heme complexes. *Proc. Natl. Acad. Sci. USA*, 69:2263, 1972.

[89] Z. Salamon and G. Tollin. Interaction of horse heart cytochrome c with lipid bilayer membranes: Effects on redox potentials. *J. Bioenerg. Biomembr.*, 29:211, 1997.

[90] C. E. Immoos, J. Chou, M. Bayachou, E. Blair, J. Greaves, and P. J. Farmer. Electrocatalytic reductions of nitrite, nitric oxide, and nitrous oxide by thermophilic cytochrome P450CYP119 in film-modified electrodes and an analytical comparison of its catalytic activities with myoglobin. *J. Am. Chem. Soc.*, 126:4934, 2004.

[91] Y. Oku, A. Ohtaki, S. Kamitori, N. Nakamura, M. Yohda, H. Ohno, and Y. Kawarabayasi. Structure and direct electrochemistry of cytochrome P450 from the thermoacidophilic crenarchaeon, Sulfolobus tokodaii strain 7. *J. Inorg. Biochem.*, 98:1194, 2004.

[92] S. Y. Rhieu, D. R. Ludwig, V. S. Siu, and G. T. R. Palmore. Direct electrochemistry of cytochrome P450 27B1 in surfactant films. *Electrochem. Commun.*, 11:1857, 2009.

[93] C. Lei, U. Wollenberger, C. Jung, and F. W. Scheller. Clay-bridged electron transfer between cytochrome $P450_{cam}$ and electrode. *Biochem. Biophys. Res. Comm.*, 268:740, 2000.

[94] A. K. Udit, N. Hindoyan, M. G. Hill, F. H. Arnold, and H. B. Gray. Protein-surfactant film voltammetry of wild-type and mutant cytochrome P450 BM3. *Inorg. Chem.*, 44:4109, 2005.

[95] A. K. Udit and H. B. Gray. Electrochemistry of heme-thiolate proteins. *Biochem. Biophys. Res. Comm.*, 338:470, 2005.

[96] B. D. Fleming, S. G. Bell, L.-L. Wong, and A. M. Bond. The electrochemistry of a heme-containing enzyme, CYP199A2, adsorbed directly onto a pyrolytic graphite electrode. *J. Electroanal. Chem.*, 611:149, 2007.

[97] H. Matsumura, N. Nakamura, M. Yohda, and H. Ohno. The electrochemical properties of thermophilic cytochrome P450 CYP119A2 at extremely high temperatures in poly(ethylene oxide). *Electrochem. Commun.*, 9:361, 2007.

[98] L. Peng, X. Yang, Q. Zhang, and S. Liu. electrochemistry of cytochrome P450 2B6 on electrodes modified with zirconium dioxide nanoparticles and platin components. *Electroanal.*, 20:803, 2008.

[99] S. J. Sadeghi, A. Fantuzzi, and G. Gilardi. Breakthrough in P450 bioelectrochemistry and future perspectives. *Biochim. Biophys. Acta*, 1814:237, 2011.

[100] D. L. Johnson, B. C. Lewis, D. J. Elliot, J. O. Miners, and L. L. Martin. Electrochemical characterization of the human cytochrome P450 2C9. *Biochem. Pharmacol.*, 69:1533, 2005.

[101] M. Yang, J. L. Kabulski, L. Wollenberg, X. Chen, M. Subramanian, T. S. Tracy, D. Lederman, P. M. Gannett, and N. Wu. Electrocatalytic drug metabolism by CYP2C9 bonded to a self-assembled monolayer-modified electrode. *Drug Metab. Disp.*, 37:892, 2009.

[102] A. Shukla, E. M. Gillam, D. J. Mitchell, and P. V. Bernhardt. Direct electrochemistry of enzymes from the cytochrome P450 2C family. *electrochem. Commun.*, 7:437, 2005.

[103] L. H. Mak, S. J. Sadeghi, A. Fantuzzi, and G. Gilardi. Control of human cytochrome P450 2E1 electrocatalytic response as a result of unique orientation on gold electrodes. *Anal. Chem.*, 82:5357, 2010.

[104] S. Liu, L. Peng, X. Yang, Y. Wu, and L. He. Electrochemistry of cytochrome P450 enzyme on nanoparticle-containing membrane-coated electrode and its applications for drug sensing. *Anal. Biochem.*, 375:209, 2008.

[105] A. K. Udit, K. D. Hagen, P. J. Goldman, A. Star, J. M. Gillan, H. B. Gray, and M. G. Hill. Spectroscopy and electrochemistry of cytochrome P450 BM3-surfactant film assemblies. *J. Am. Chem. Soc.*, 128:10320, 2006.

[106] P. Panicco, Y. Astuti, A. Fantuzzi, J. R. Durrant, and G. Gilardi. P450 versus P420: correlation between cyclic voltammetry and visible absorption spectroscopy of the immobilized heme domain of cytochrome P450 BM3. *J. Phys. Chem. B*, 112:14063, 2008.

[107] F. P. Guengerich, D. P. Ballou, and M. J. Coon. Purified liver microsomal cytochrome P450 - Electron-accepting properties and oxidation-reduction potential. *J. Biol. Chem.*, 250:7405, 1975.

[108] A. K. Udit, M. G. Hill, V. G. Bittner, F. H. Arnold, and H. B. Gray. Reduction of dioxygen catalyzed by pyrene-wired heme domain of cytochrome P450 BM3 electrodes. *J. Am. Chem. Soc.*, 126:10218, 2004.

[109] A. J. Bard and L. R. Faulkner. *Electrochemical methods: Fundamentals and Applications*. Wiley, 2001.

[110] S. Todorovic, C. Jung, P. Hildebrandt, and D. H. Murgida. Conformational transitions and redox potential shifts of cytochrome P450 induced by immobilization. *J. Biol. Inorg. Chem.*, 11:119, 2006.

[111] E. Abe, C. Miyaura, H. Sakagami, M. Takeda, K. Konno, T. Yamazaki, S. Yoshiki, and T. Suda. Differentiation of mouse myeloid leukemia cells induced by 1α,25-dihydroxyvitamin D_3. *Proc. Natl. Acad. Sci. USA*, 78:4990, 1981.

[112] E. L. Smith, N. C. Walworth, and M. F. Holick. Effect of 1α,25-dihydroxyvitamin D_3 on the morphological and biochemical differentiation of cultured human epidermal keratinocytes grown in serum-free conditions. *J. Invest. Dermatol.*, 86:709, 1986.

[113] A. S. Dusso, A. J. Brown, and E. Slatopolsky. Vitamin D. *Am. J. Physiol. Renal Physiol.*, 289:F8, 2005.

[114] A. J. Brown and E. Slatopolsky. Vitamin D analogs: Therapeutic applications and mechanism for selectivity. *Mol. Asp. Med.*, 29:433, 2008.

[115] G. Jones. Vitamin D analogs. *Endocrinol. Metab. Clin. North Am.*, 39:447, 2010.

[116] Y. Ohyama and K. Okuda. Isolation and characterization of a cytochrome P450 from rat kidney mitochondria that catalyzes the 24-hydroxylation of 25-hydroxyvitamin D_3. *J. Biol. Chem.*, 266:8690, 1991.

[117] Y. Miyamoto, T. Shinki, K. Yamamoto, Y. Ohyama, H. Iwasaki, R. Hosotani, T. Kasama, H. Takayama, S. Yamada, and T. Suda. 1α,25-dihydroxyvitamin D_3-24-hydroxylase (CYP24) hydroxylates the carbon at the end of the side chain (C-26) of the C-24-fluorinated analog of 1α,25-dihydroxyvitamin D_3. *J. Biol. Chem.*, 272:14115, 1997.

[118] R. P. Esvelt, H. K. Schnoes, and H. F. DeLuca. Isolation and characterization of 1α-hydroxy-23-carboxytetranorvitamin D - Major metabolite of 1,25-dihydroxyvitamin D_3. *Biochemistry*, 18:3977, 1979.

[119] G. Makin, D. Lohnes, V. Byford, R. Ray, and G. Jones. Target-cell metabolism of 1,25-dihydroxyvitamin D_3 to calcitroic acid - Evidence for a pathway in kidney and bone involving 24-oxidation. *Biochem. J.*, 262:173, 1989.

[120] J. L. Napoli and R. L. Horst. 23,25,26-trihydroxycholecalciferol - A 25-hydroxycholecalciferol-26,23-lactone precursor. *Biochem. J.*, 206:173, 1982.

[121] J. Y. Zhou, A. W. Norman, M. Lubbert, E. D. Collins, M. R. Uskoković, and H. P. Koeffler. Novel vitamin D analogs that modulate leukemic cell growth and differentiation with little effect on either intestinal calcium absorption or bone calcium mobilization. *Blood*, 74:82, 1989.

[122] J. Y. Zhou, A. W. Norman, D. L. Chen, G. W. Sun, M. R. Uskoković, and H. P. Koeffler. 1,25-dihydroxy-16-ene-23-yne-vitamin D_3 prolongs survival time of leukemic mice. *Proc. Natl. Acad. Sci. USA*, 87:3929, 1990.

[123] P. K. Dantuluri, C. Haning, M. R. Uskoković, K. Y. Tserng, and G. S. Reddy. *Vitamin D - A pluripotent steroid hormone: Structural studies, molecular endocrinology and clinical applications.* Walter de Gruyter, 1994.

[124] M. R. Uskoković, A. W. Norman, P. S. Manchand, G. P. Studzinski, M. J. Campbell, H. P. Koeffler, A. Takeuchi, M. L. Siu-Caldera, D. S. Rao, and G. S. Reddy. Highly active analogs of 1α,25-dihydroxyvitamin D_3 that resist

metabolism through C-24 oxidation and C-3 epimerization pathways. *Steroids*, 66:463, 2001.

[125] G. S. Reddy, G. Jones, S. W. Kooh, D. Fraser, and H. F. DeLuca. Stimulation of 24*R*,25-dihydroxyvitamin D_3 synthesis by metabolites of vitamin D_3. *Am. J. Physiol.*, 245:E359, 1983.

[126] G. S. Reddy, K. Y. Tserng, B. R. Thomas, R. Dayal, and A. W. Norman. Isolation and identification of 1,23-dihydroxy-24,25,26,27-tetranorvitamin D_3, a new metabolite of 1,25-dihydroxyvitamin D_3 produced in rat kidney. *Biochemistry*, 26:324, 1987.

[127] K. VanWeelden, L. Flanagan, L. Binderup, M. Tenniswood, and J. Welsh. Apoptotic regression of MCF-7 xenografts in nude mice treated with the vitamin D_3 analog, EB1089. *Endocrinology*, 139:2102, 1998.

[128] C. Crescioli, P. Ferruzzi, A. Caporali, M. Scaltriti, S. Bettuzzi, R. Mancina, S. Gelmini, M. Serio, D. Villari, G. B. Vannelli, E. Colli, L. Adorini, and M. Maggi. Inhibition of prostate cell growth by BXL-628, a calcitriol analogue selected for a phase II clinical trial in patients with benign prostate hyperplasia. *Eur. J. Endocrinol.*, 150:591, 2004.

[129] S. Peleg, F. Khan, N. M. Navone, D. D. Cody, E. A. Johnson, C. S. Van Pelt, and G. H. Posner. Inihibition of prostate cancer-mediated osteoblastic bone leisions by the low-calcemic analog 1α-hydroxymethyl-16-ene-26,27-bishomo-25-hydroxyvitamin D_3. *J. Steroid Biochem. Mol. Biol.*, 97:203, 2005.

[130] L. Adorini, G. Penna, S. Amuchastegui, C. Cossetti, F. Aquilano, R. Mariani, B. Fibbi, A. Morelli, M. R. Uskoković, E. Colli, and M. Maggi. Inhibition of prostate growth and inflammation by the vitamin D receptor agonist BXL-628 (elocalcitol). *J. Stereoid Biochem. Mol. Biol.*, 103:689, 2007.

[131] K. W. Colston, A. G. Mackay, S. Y. James, L. Binderup, S. Chander, and R. C. Coombes. EB1089 - a new vitamin D analog that inhibits the growth of breast cancer cells *in vivo* and *in vitro*. *Biochem. Pharmacol.*, 44:2273, 1992.

[132] V. N. Shankar, F. J. Dilworth, H. L. J. Makin, N. J. Schroeder, D. J. H. Trafford, A. M. Kissmeyer, M. J. Calverley, E. Binderup, and G. Jones. Metabolism of the vitamin D analog EB1089 by cultured human cells: Redirection of hydroxylation site to distal carbons of the side-chain. *Biochem. Pharmacol.*, 53:783, 1997.

[133] C. M. Hansen and P. H. Mäenpää. EB1089, a novel vitamin D analog with strong antiproliferative and differentiation-inducing effects on target cells. *Biochem. Pharmacol.*, 54:1173, 1997.

[134] B. L. Lokeshwar, G. G. Schwartz, M. G. Selzer, K. L. Burnstein, S. H. Zhuang, N. L. Block, and L. Binderup. Inhibition of prostate cancer metastasis *in vivo*: A comparison of 1,25-dihydroxyvitamin D (calcitriol) and EB1089. *Cancer Epidemiol. Biomarkers Prev.*, 8:241, 1999.

[135] T. R. J. Evans, K. W. Colston, F. J. Lofts, D. Cunningham, D. A. Anthoney, H. Gogas, J. S. de Bono, K. J. Hamberg, T. Skoy, and J. L. Mansi. A phase II trial of the vitamin D analogue Seocalcitol (EB1089) in patients with inoperable pancreatic cancer. *Br. J. Cancer*, 86:680, 2002.

[136] A. J. Annalora, E. Bobrovnikova-Marjon, R. Serda, L. Lansing, M. L. Chiu, A. Pastuszyn, S. Iyer, C. B. Marcus, and J. L. Omdahl. Rat cytochrome P450C24 (CYP24A1) and the role of F249 in substrate binding and catalytic activity. *Arch. Biochem. Biophys.*, 425:133, 2004.

[137] Y. Sagara, A. Wada, Y. Takata, M. R. Waterman, K. Sekimizu, and T. Horiuchi. Direct expression of adrenodoxin reductase in *Escherichia coli* and the functional characterization. *Biol. Pharmacol. Bull.*, 16:627, 1993.

[138] W. Gnanaiah and J. L. Omdahl. Isolation and characterization of pig kidney mitochondrial ferredoxin-$NADP^+$ oxidoreductase. *J. Biol. Chem.*, 261:12649, 1986.

[139] T. Kimura, J. H. Parcells, and H. P. Wang. Purification of adrenodoxin reductase, adrenodoxin, and cytochrome P450 from adrenal cortex. *Methods Enzymol.*, 52:132, 1978.

[140] D. S. Goodsell and A. J. Olson. Automated docking of substrates to proteins by simulated annealing. *Proteins: Struct. Funct. Bioinform.*, 8:195, 1990.

[141] D. S. Goodsell, G. M. Morris, and A. J. Olson. Automated docking of flexible ligands: Applications of AutoDock. *J. Mol. Recognit.*, 9:1, 1996.

[142] A. W. Schuttelkopf and D. M. F. van Aalten. PRODRG: a tool for high-throughput crystallography of protein-ligand complexes. *Acta Crystallogr. Sect. D-Biol.Crystallogr.*, 60:1355, 2004.

[143] S. Sloan, D. J. Harvey, and P. Vouros. Interaction and rearrangement of trimethylsiloxy functional groups. Structural significance of the m/z 147 ion in the mass spectra of trimethylsilyl steroidal ethers. *Org. Mass Spectrom.*, 5:789, 1971.

[144] T. Kusudo, T. Sakaki, D. Abe, T. Fujishima, A. Kittaka, H. Takayama, M. Ohta, and K. Inouye. Metabolism of 20-epimer of 1α,25-dihydroxyvitamin D_3 by CYP24: species-based difference between humans and rats. *Biochem. Biophys. Res. Commun.*, 309:885, 2003.

[145] T. Sakaki, N. Sawada, D. Abe, K. Komai, S. Shiozawa, Y. Nanaka, N. Nakagawa, T. Okano, M. Ohta, and K. Inouye. Metabolism of 26,26,26,27,27,27-F_6-1α,25-dihydroxyvitamin D_3 by CYP24: species-based difference between humans and rats. *Biochem. Pharmacol.*, 65:1957, 2003.

[146] T. Kusudo, T. Sakaki, D. Abe, T. Fujishima, A. Kittaka, H. Takayama, S. Hatakeyama, M. Ohta, and K. Inouye. Metabolism of A–ring diastereomers

of 1α,25-dihydroxyvitamin D_3 by CYP24A1. *Biochem. Biophys. Res. Commun.*, 321:774, 2004.

[147] H. Sai, S. Takatsuto, N. Hara, and N. Ikekawa. Synthesis of 1α,25-dihydroxy-26,27-dimethylvitamin D_3, a highly active analog of 1α,25-dihydroxyvitamin D_3. *Chem. Pharm. Bull.*, 33:878, 1985.

[148] A. M. Kissmeyer, E. Binderup, L. Binderup, C. M. Hansen, N. R. Andersen, H. L. J. Makin, N. J. Schroeder, V. N. Shankar, and G. Jones. Metabolism of the vitamin D analog EB 1089: Identification of *in vivo* and *in vitro* liver metabolites and their biological activities. *Biochem. Pharmacol.*, 53:1087, 1997.

[149] F. J. Dilworth, I. Scott, A. Green, S. Strugnell, Y. D. Guo, E. A. Roberts, R. Kremer, M. J. Calverley, H. L. J. Makin, and G. Jones. Different mechanisms of hydroxylation site selection by liver and kidney cytochrome P450 species (CYP27 and CYP24) involved in vitamin D metabolism. *J. Biol. Chem.*, 270:16766, 1995.

[150] I. V. Tetko and V. Y. Tanchuk. Application of associative neural networks for prediction of lipophilicity in ALOGPS 2.1 program. *J. Chem. Inf. Comput. Sci.*, 42:1136, 2002.

[151] N. Mast, M. A. Whitet, I. Bjorkhem, E. F. Johnson, C. D. Stout, and I. A. Pikuleva. Crystal structures of substrate–bound and substrate–free cytochrome P450 46A1, the principal cholesterol hydroxylase in the brain. *Proc. Natl. Acad. Sci. USA*, 105:9546, 2008.

[152] Y. T. Lee, E. C. Glazer, R. F. Wilson, C. D. Stout, and D. B. Goodin. Three clusters of conformational states in $P450_{cam}$ reveal a multistep pathway for closing of the substrate access channel. *Biochemistry*, 50:693, 2011.

[153] H. Hamamoto, T. Kusudo, N. Urushino, H. Masuno, K. Yamamoto, S. Yamada, M. Kamakura, M. Ohta, K. Inouye, and T. Sakaki. Structure-function

analysis of vitamin D 24-hydroxylase (CYP24A1) by site-directed mutagenesis: Amino acid residues responsible for species-based difference of CYP24A1 between human and rats. *Mol. Pharmacol.*, 70:120, 2006.

[154] A. J. Annalora, E. Bobrovnikov-Marion, R. Serda, A. Pastuszyn, S. E. Graham adn C. B. Marcus, and J. L. Omdahl. Hybrid homology modeling and mutational analysis of cytochrome P450C24A1 (CYP24A1) of the vitamin D pathway: Insights into substrate specificity and membrane bound structure-function. *Arch. Biochem. Biophys.*, 460:262, 2007.

[155] D. E. Prosser, M. Kaufmann, B. O'Leary, V. Byford, and G. Jones. Single A326G mutation converts human CYP24A1 from 25OHD$_3$-24-hydroxylase into 23-hydroxylase, generating 1α,25(OH)$_2$D$_3$-26,23-lactone. *Proc. Natl. Acad. Sci. USA*, 104:12673, 2007.

[156] S. Masuda, D. E. Prosser, Y. D. Guo, M. Kaufmann, and G. Jones. Generation of a homology model for the human cytochrome P450, CYP24A1, and the testing of putative substrate binding residues by site-directed mutagenesis and enzyme activity studies. *Arch. Biochem. Biophys.*, 460:177, 2007.

[157] P. Hlavica. Models and mechanisms of O–O bond activation by cytochrome P450 - A critical assessment of the potential role of multiple active intermediates in oxidative catalysis. *Eur. J. Biochem.*, 271:4335, 2004.

[158] N. Astecker, E. A. Bobrovnikova, J. L. Omdahl, L. Gennaro, P. Vouros, I. Schuster, M. R. Uskoković, S. Ishizuka, G. Wang, and G. S. Reddy. C-25 hydroxylation of 1α,24R-dihydroxyvitamin D$_3$ is catalyzed by 25-hydroxyvitamin D$_3$-24-hydroxylase (CYP24A1): metabolism studies with human keratinocytes and rat recombinant CYP24A1. *Arch. Biochem. Biophys.*, 431:261, 2004.

[159] S. Masuda, S. A. Strugnell, J. C. Knutson, R. St-Arnaud, and G. Jones. Evidence for the activation of 1α-hydroxyvitamin D$_2$ by 25-hydroxyvitamin D-24-hydroxylase: Delineation of pathways involving 1α,24-dihydroxyvitamin D$_2$ and 1α,25-dihydroxyvitamin D$_2$. *Biochim. Biophys. Acta*, 1761:221, 2006.

[160] B. F. Brumbaugh and M. R. Haussler. Nuclear and cytoplasmic binding components for vitamin D metabolites. *Life Sci.*, 16:353, 1975.

[161] A. Verstuyf, G. Carmeliet, R. Bouillon, and C. Mathieu. Vitamin D: a pleiotropic hormone. *Kindey Int.*, 78:140, 2010.

[162] G. S. Reddy, K. R. Muralidharan, W. H. Okamura, K. Y. Tserng, and J. A. McLane. *Vitamin D - A pluripotent steroid hormone: Structural studies, molecular endocrinology and clinical applications.* Walter de Gruyter, 1994.

[163] M. G. Bischof, M. L. Siu-Caldera, A. Weiskopf, P. Vouros, H. S. Cross, M. Peterlik, and G. S. Reddy. Differentiation-related pathways of 1α,25-dihydroxycholecalciferol metabolism in human colon adenocarcinoma-derived Caco-2 cells: Production of 1α,25-dihydroxy-3epi-cholecalciferol. *Exp. Cell Res.*, 241:194, 1998.

[164] M. L. Siu-Caldera, H. Sekimoto, A. Weiskopf, P. Vouros, K. R. Muralidharan, W. H. Okamura, J. Bishop, A. W. Norman, M. R. Uskoković, I. Schuster, and G. S. Reddy. Production of 1α,25-dihydroxy-3-epi-vitamin D_3 in two rat osteosarcoma cell lines (UMR 106 and ROS 17/2.8): Existence of the C-3 epimerization pathway in ROS 17/2.8 cells in which the C-24 oxidation pathway is not expressed. *Bone*, 24:457, 1999.

[165] H. Sekimoto, M. L. Siu-Caldera, A. Weiskopf, P. Vouros, K. R. Muralidharan, W. H. Okamura, M. R. Uskoković, and G. S. Reddy. 1α,25-dihydroxy-3-epi-vitamin D_3: *In vivo* metabolite of 1α,25-dihydroxyvitamin D_3 in rats. *FEBS Lett.*, 448:278, 1999.

[166] N. Astecker, G. S. Reddy, G. Herzig, G. Vorisek, and I. Schuster. 1α,25-dihydroxy-3-epi-vitamin D_3 a physiological metabolite of 1α,25-dihydroxyvitamin D_3: Its production and metabolism in primary human keratinocytes. *Mol. Cell. Endocrinol.*, 170:91, 2000.

[167] G. S. Reddy, K. R. Muralidharan, W. H. Okamura, K. Y. Tserng, and J. A. McLane. Metabolism of 1α,25-dihydroxyvitamin D_3 and its C-3 epimer 1α,25-dihydroxy-3-epi-vitamin D_3 in neonatal human keratinocytes. *Steroids*, 66:441, 2001.

[168] G. S. Reddy, M. L. Siu-Caldera, I. Schuster, N. Astecker, K. Y. Tserng, K. R. Muralidharan, W. H. Okamura, J. A. McLane, and M. R. Uskoković. *Vitamin D - Chemistry, biology and clinical applications of the steroid hormone*. Walter de Gruyter, 1997.

[169] A. W. Norman, R. Bouillon, M. C. Farach-Carson, J. E. Bishop, L. X. Zhou, I. Nemere, J. Zhao, K. R. Muralidharan, and W. H. Okamura. Demonstration that 1β,25-dihydroxyvitamin D_3 is an antagonist of the nongenomic but not genomic biological responses and biological profile of the three A–ring diastereomers of 1α,25-dihydroxyvitamin D_3. *J. Biol. Chem.*, 268:20022, 1993.

[170] I. Schuster, N. Astecker, H. Egger, G. Herzig, G. S. Reddy, J. Schmid, and G. Vorisek. *Vitamin D - Chemistry, biology and clinical applications of the steroid hormone*. Walter de Gruyter, 1997.

[171] A. J. Brown, C. Ritter, E. Slatopolsky, K. R. Muralidharan, W. H. Okamura, and G. S. Reddy. 1α,25-dihydroxy-3-epi-vitamin D_3, a natural metabolite of 1α,25-dihydroxyvitamin D_3, is a potent suppresor of parathyroid hormone secretion. *J. Cell. Biochem.*, 73:106, 1999.

[172] V. K. Rehan, J. S. Torday, S. Peleg, L. Gennaro, P. Vouros, J. Padbury, D. S. Rao, and G. S. Reddy. 1α,25-dihydroxy-3-epi-vitamin D_3, a natural metabolite of 1α,25-dihydroxyvitamin D_3: production and biological activity studies in pulmonary alveolar type II cells. *Mol. Genet. Metab.*, 76:46, 2002.

[173] N. A. Morrison and J. A. Eisman. Nonhypercalcemic 1,25-$(OH)_2D_3$ analogs potently induce the human osteocalcin gene promoter stably transfected into rat osteosarcoma (ROSCO-2). *J. Bone Miner. Res.*, 6:893, 1991.

[174] J. C. Fleet, J. Bradley, G. S. Reddy, R. Ray, and R. J. Wood. 1α,25-$(OH)_2$-vitamin D_3 analogs with minimal in vivo calcemic activity can stimulate significant transepithelial calcium transport and mRNA expression *in vitro*. *Arch. Biochem. Biophys.*, 329:228, 1996.

[175] G. S. Reddy, D. S. Rao, and M. L. Siu-Caldera. *Vitamin D Endocrine System - Structural, biological, genetic and clinical aspects*. Printing and Reprographics, University of California, Riverside, 2000.

[176] H. Harant, D. Spinner, G. S. Reddy, and I. J. D. Lindley. Natural metabolites of 1α,25-dihydroxyvitamin D_3 retain biologic activity mediated through the vitamin D receptor. *J. Cell. Biochem.*, 78:112, 2000.

[177] F. Molnár, R. Sigüeiro, Y. Sato, C. Araujo, I schuster, P. Antony, J. Peluso, C. Muller, A. Mouriño, D. Moras, and N. Rochel. 1α,25$(OH)_2$-3-epi-vitamin D_3, a natural physiological metabolite of vitamin D_3: its synthesis, biological activity and crystal structure with its receptor. *PLoS ONE*, 6:e18124, 2011.

[178] G. S. Reddy, J. L. Omdahl, M. Robinson, G. C. Wang, G. T. R. Palmore, D. Vicchio, A. L. Yergey, K. Y. Tserng, and M. R. Uskoković. 23-carboxy-24,25,26,27-tetranorvitamin D_3 (calcioic acid) and 24-carboxy-25,26,27-trinorvitamin D_3 (cholacalcioic acid): End products of 25-hydroxyvitamin D_3 metabolism in rat kidney through C-24 oxidation pathway. *Arch. Biochem. Biophys.*, 455:18, 2006.

[179] T. M. Penning, M. J. Bennett, S. SmithHoog, B. P. Schlegel, J. M. Jez, and M. Lewis. Structure and function of 3α-hydroxysteroid dehydrogenase. *Steroids*, 62:101, 1997.

[180] K. Nakagawa, Y. Sowa, M. Kurobe, K. Ozono, M. L. Siu-Caldera, G. S. Reddy, M. R. Uskoković, and T. Okano. Differential activities of 1α,25-dihydroxy-16-ene-vitamin D_3 analogs and their 3-epimers on human promyelocytic leukemia (HL-60) cell differentiation and apoptosis. *Steroids*, 66:327, 2001.

[181] P. Furigay and N. Swamy. Anti-endothelial properties of 1,25-dihydroxy-3-epi-vitamin D_3, a natural metabolite of calcitriol. *J. Steroid Biochem. Mol. Biol.*, 89-90:427, 2004.

[182] A. J. Brown, C. S. Ritter, A. S. Weiskopf, P. Vouros, G. J. Sasso, M. R. Uskoković, G. C. Wang, and G. S. Reddy. Isolation and identification of 1α-hydroxy-3-epi-vitamin D_3, a potent suppressor of parathyroid hormone secretion. *J. Cell. Biochem.*, 96:569, 2005.

[183] M. W. Choi, K. Yamamoto, H. Masuno, K. Nakashima, T. Taga, and S. Yamada. Ligand recognition by the vitamin D receptor. *Bioorg. Med. Chem.*, 9:1721, 2001.